HIGH STRAIN RATE INDUCED FAILURE IN STEELS AT HIGH SHEAR STRAINS

by

Nebojša Panić

A thesis submitted to the Faculty of Graduate Studies
in partial fulfillment of
the requirements for the degree of

Master of Science

in Mechanical Engineering

Department of Mechanical Engineering
University of Manitoba
Winnipeg, Manitoba, Canada

0-612-45106-2

THE UNIVERSITY OF MANITOBA

FACULTY OF GRADUATE STUDIES

*****

COPYRIGHT PERMISSION PAGE

High Strain Rate Induced Failure in Steels at High Shear Strains

BY

Nebojša Panić

A Thesis/Practicum submitted to the Faculty of Graduate Studies of The University of Manitoba in partial fulfillment of the requirements of the degree

of

Master of Science

ACKNOWLEDGMENTS

I am taking this opportunity to thank all the people who helped me throughout this project and beyond. My first and most sincere gratitude belongs to my advisor, and I would also like to call him a friend, Dr. M. Nabil Bassim. It is his exceptional balance of teaching, advisory and personal skills that made my experience as a student an unforgettable one.

Besides my advisor, I would like to thank every professor that took part in teaching me throughout my 5 years as a student at the University of Manitoba because it was a combined knowledge of many disciplines that enabled me to complete this work.

I would like to thank the technicians at the Mechanical Engineering Department: Mr. Don Mardis, Mr. John Van Dorp and Mr. Irwin Penner for the most needed help I received from them. Their patience was exemplary and I appreciate it more than I can say.

At last, I would like to share this great moment with all the other people that were in the same boat as I was. These are my gradmates (the word means like classmates, but since we were not in the same class but we were in the same department of graduate studies, I had to make the name).

Now that this is over, I will remember it as an enjoyable experience despite the hard work that was involved.

TABLE OF CONTENTS

LIST OF FIGURES

FIGURE PAGE

FIGURE PAGE

FIGURE PAGE

LIST OF TABLES

LIST OF SYMBOLS

γ	Shear strain
$\dot{\gamma} = \partial\gamma/\partial t$	Shear strain rate (s^{-1})
τ	Shear stress (Pa)
V	Dislocation velocity (cm/s)
N	Number of mobile dislocations
b	Magnitude of Burger's vector
ρ_m	Density of mobile dislocations ($1/m^2$)
t	Time (s)
ΔF^*	Helmholtz free energy change
ΔG^*	Gibbs free energy change
ν	Dislocation vibration frequency
k	Boltzmann's constant = $1.38\text{x}10^{-23}$ (J/K) or thermal conductivity (W/mK)
a	Thermal diffusivity (m^2/s)
T	Temperature (K)
$\gamma^p, \dot{\gamma}^p$	Plastic strain and plastic strain rate (s^{-1})
$\tau^*(0)$	Stress required for dislocation to overcome obstacle at 0K (Pa)
T_c	Thermal activation temperature for dislocation (K)
θ	Temperature (K)
ρ	Density (kg/m^3)
c	Specific heat capacity (J/kgK)
$\partial\tau/\tau\partial\gamma$	Strain hardening
$(-\partial\tau/\partial\theta)/\rho c$	Thermal softening
n	Strain hardening exponent
m	Strain rate sensitivity
γ_i	Instability strain

$\dot{H}$	Void growth rate
$\Delta \ln \dot{\gamma} / \Delta \ln \gamma$	Inhomogeneity in the deforming body
$k(\gamma)$	Inhomogeneity amplification factor
δ	Adiabatic shear band halfwidth (μm)
θ_m	Temperature at the centre of the band (K)
θ_δ	Temperature at the band boundary (K)
ϕ	Angle of twist
L_s	Specimen gauge length (mm)
D_s	Mean specimen diameter (mm)
D	Diameter of the Hopkinson bar (mm)
T_s	Average torque in specimen

ABSTRACT

Materials deformed at high strain rates exhibit sometimes the behaviour that is very different from that at static or quasi-static loading. Material and physical properties that are of no concern in low strain rates become crucial in the material response at high strain rates. Material properties such as thermal diffusivity and thermal softening have to be considered in order to understand the mechanism of deformation at high strain rates. The most important aspect of high strain rate deformation is the occurrence of local thermal and mechanical instability that leads to failure of the material, usually characterised by the occurrence of adiabatic shear bands (ASB).

In this study, AISI 4140 steel was tested using a torsional split Hopkinson bar at three different strain rates and the impact of strain rate on the material behaviour was examined. It was concluded that material response changes with the strain rate, where the width of the shear band is wider for the lower strain rate and narrower for the higher strain rate. The influence of material hardness on failure mechanisms was also investigated by producing different tempers of 4140 steel with distinct microstructures and different hardness. It was concluded that the hardness plays an important role in deformation and failure characteristics of 4140 steel. All specimens tested exhibited the formation of ASB with differences in shear band type. Depending on strain rate and hardness, some specimens showed deformed shear band, and some showed transformed shear band. The fracture surface of specimens was examined under the scanning electron microscope (SEM), and it was found that all specimens fractured in the ductile manner. There was no evidence of brittle fracture which would be expected at higher strain rates. It was found that the strain rate and hardness did not have an impact on the fracture type, but they had the impact on characteristics of the fracture, resulting in the smaller dimples and narrower shear bands for harder samples.

CHAPTER 1 THEORETICAL BACKGROUND AND LITERATURE REVIEW

1.1 INTRODUCTION

The idea of testing materials at high rates of strain dates back to the 1830's when French militarists were exploding cannon balls in order to determine the right amount of explosive needed for the optimal explosion [1]. Later, in 1872, John Hopkinson published a paper on findings after testing an iron wire that had the upper end fixed and free weight at the lower end. By dropping the weight, he concluded that the stress of the wire is higher for the dynamic loading conditions than for the static loading conditions.

The tangible consequence of the high strain rate loading was first examined by Tresca [2] in 1878 when he discovered the "hot lines" while forging the platinum bar. Zener and Hollomon [3] were the first to consider the adiabatic conditions and the effects of thermal softening and strain hardening during the high strain rate deformation when they discovered the 32 μm wide shear band while punching the steel plate with a die. They originated the idea of the triumph of thermal softening over strain hardening due to the high rate effects. This study was followed by many important works including Costin *et al.* [4], Hartley *et al.* [5], Giovanola [6], Marchand and Duffy [7], Bai [8], Moss [9] and Lindholm and Johnson [10], among many others.

The appearance of adiabatic shear bands (ASB) is observed in many applications including cutting, forming, impact loading, penetration, and is an important factor in industries such as mining, military, nuclear industry, aircraft industry, rail, etc. Understanding the behaviour of materials at high strain rates is crucial for the proper material selection and adequate application in industry.

1.2 EFFECT OF STRAIN RATE AND TEMPERATURE ON MATERIAL BEHAVIOUR

Much of the work has been done in examining the influence of strain rate and temperature on material behaviour [1, 11, 12, 13, 14]. While strain rate and temperature play role in the material behaviour, strain rate history and temperature history also play a major role in the deformation mechanisms. Lindholm [15] performed tests on the influence of strain rate history on flow stress on aluminum, and showed that if the material is prestrained at a lower strain rate and then deformed at a higher strain rate, its flow stress will be lower than if it were deformed at the constant higher strain rate throughout the test. Hartley and Duffy [16] reached the same conclusions along with many other researchers [17, 18].

1.2.1 Dislocation Velocity and Flow Stress

Dislocation motion plays the most important role in the plastic deformation of materials. In fact, it is the source of the plastic deformation. Observed moving dislocations have certain velocity that depends on the applied stress and temperature, as well as on the material properties. The empirical equation describing the dislocation motion is given by [19]

$$V = \left(\frac{\tau}{\tau_0}\right)^n \tag{1.1}$$

where τ is applied shear stress resolved in the slip plane, τ_0 is shear stress for the velocity $V = 1$ cm/s, and n is the dislocation velocity exponent. The dislocation velocity exponent, n, is a material property and depends on the strain rate and temperature. Figure 1.1 presents data on dislocation velocity for lithium fluoride [20].

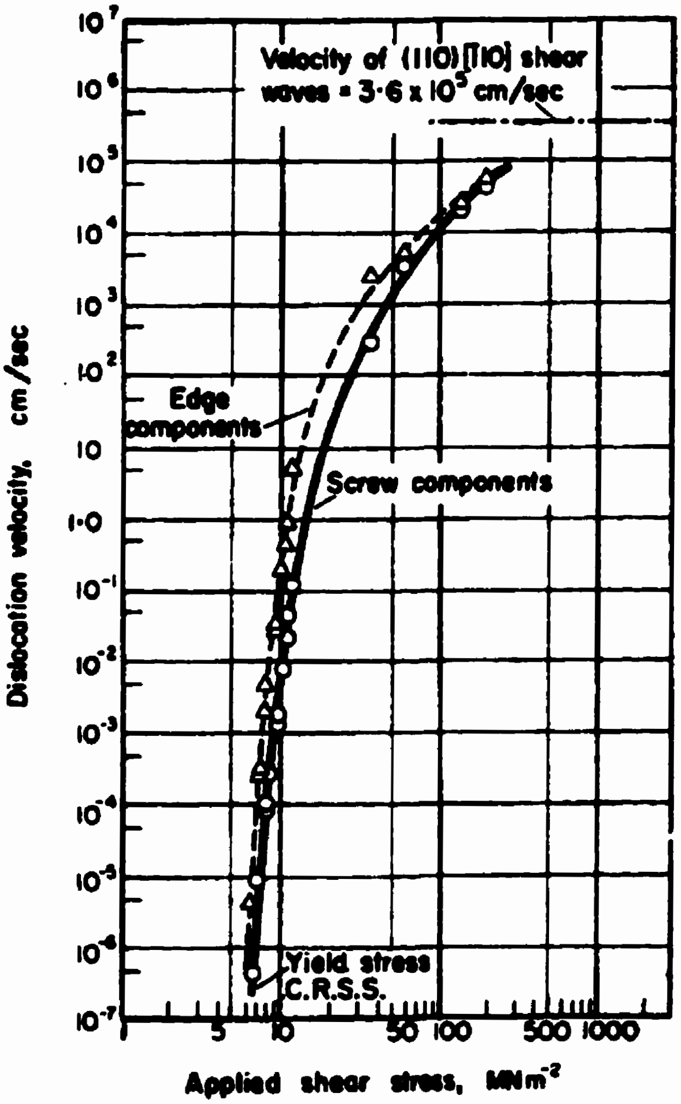

Figure 1.1: Change of Dislocation Velocity With Applied Stress [20]

Equation (1.1) roughly describes the strain rate sensitivity of the material. For example, Silicon and Germanium that have $n \sim 2$, will have considerable change in the flow stress for changes in dislocation velocities from say, 10^{-3} to 10^{3} cm/s. However, Copper that has large n, will not be strain rate sensitive since the change in the dislocation velocities from 10^{-3} to 10^{3} cm/s will not change its flow stress considerably.

1.2.2 Plastic Strain and Strain Rate Due to Dislocation Motion

For the regime of deformation described in this work, only plastic deformation is of interest for the description of material behaviour. The elastic part of the deformation (Hooke's law) is omitted here since it is not related to dislocation motion and it does not influence neither the mechanism of deformation nor the final failure morphology.

When an external stress is applied to a body, dislocations will start to move with velocity given by equation (1.1). The motion of dislocations presents a plastic work done by dislocations, or plastic deformation. Consider a crystal with volume

$$hld \tag{1.2}$$

where h is crystal height, l is length and d is a distance that a dislocation moves across (Figure 1.2). When the shear stress is applied to the crystal, each of N mobile dislocations will move certain distance x_i, and a total displacement of the crystal will be

$$D = \frac{b}{d} \sum_{i=1}^{N} x_i \tag{1.3}$$

where b is a magnitude of the Burger's vector of a dislocation [21]. The macroscopic shear strain will therefore be

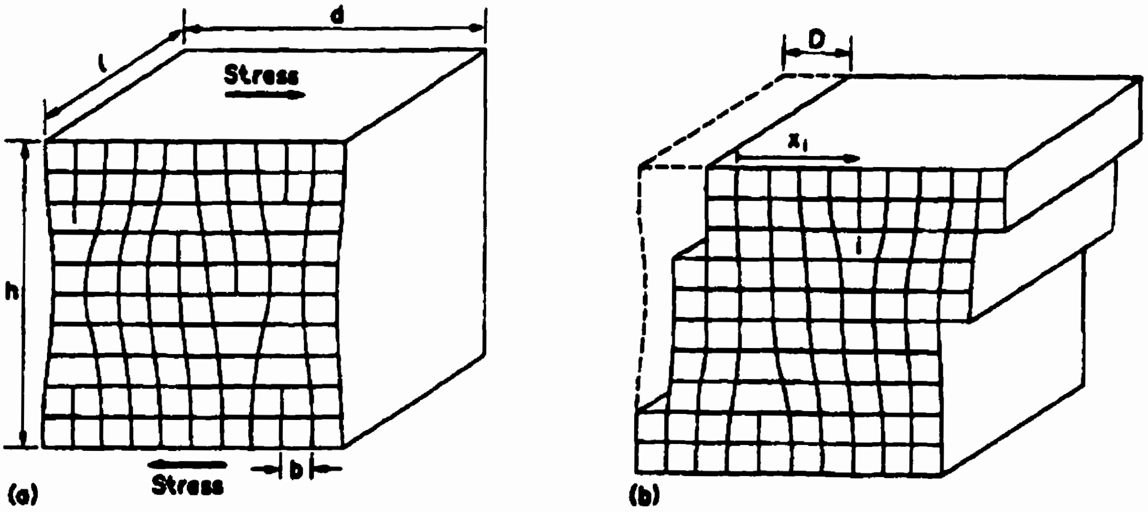

Figure 1.2: Shear Strain in a Crystal [21]

$$\gamma = \frac{D}{h} = \frac{b}{hd}\sum_{i=1}^{N} x_i \tag{1.4}$$

The average distance that a dislocation moves is given by

$$\bar{x} = \frac{1}{N}\sum_{i=1}^{N} x_i \tag{1.5}$$

Substituting equation (1.5) into equation (1.4) and noting that a density of the mobile dislocations is

$$\rho_m = \frac{Nl}{hld}$$

the relation for shear strain is obtained

$$\gamma = b\rho_m\bar{x} \tag{1.6}$$

When equation (1.6) is differentiated with respect to time t, the relation for shear strain rate can be obtained

$$\dot{\gamma} = \frac{d\gamma}{dt} = b\rho_m\bar{V} \tag{1.7}$$

Equation (1.7) is the Orowan equation and relates the plastic shear strain rate $\dot{\gamma}$ in a crystal to Burger's vector b, the average dislocation velocity $\bar{V}$, and the mobile dislocation density ρ_m [22].

1.2.3 Strain Rate Dependence of Flow Stress

As mentioned earlier, the flow stress of a material is dependent on the strain rate and temperature. While at low strain rates (i.e., static and quasi-static loading), the flow stress is constant over the wide range of strain rates, it becomes dependent on strain rate at certain limit [1, 23, 24, 25]. Figure 1.3 (a) presents data for several grades of steel, and figure 1.3 (b) presents data for pure copper [1]. The strain rate sensitivity of the material is usually taken to be the slope of the logarithmic plot of the flow stress and strain rate at the constant temperature and at constant value of strain [23]

$$N = \left(\frac{\partial \ln \dot{\gamma}}{\partial \ln \tau}\right)_{T,\gamma}$$

modified for the shear loading.

In order for dislocations to move, they have to be supplied with energy. This energy has both mechanical and thermal components. Strain rate and temperature dependence of the flow stress is a consequence of this energy. The equations describing the strain rate and temperature dependence of the flow stress usually have only thermal component present. The reason behind this is that the strain rate dependence of the flow stress is actually the consequence of the stress dependence on Gibbs free energy of activation [21]. Therefore, in the following equations, the Gibbs free energy change presents the factor taking into account the dependence of the flow stress on the strain rate.

The following model is also called a thermal activation model because it considers the thermal activation energy to be the main source of energy that allows moving dislocations to overcome the barriers. The mechanical part of the required energy is supplied by the external load.

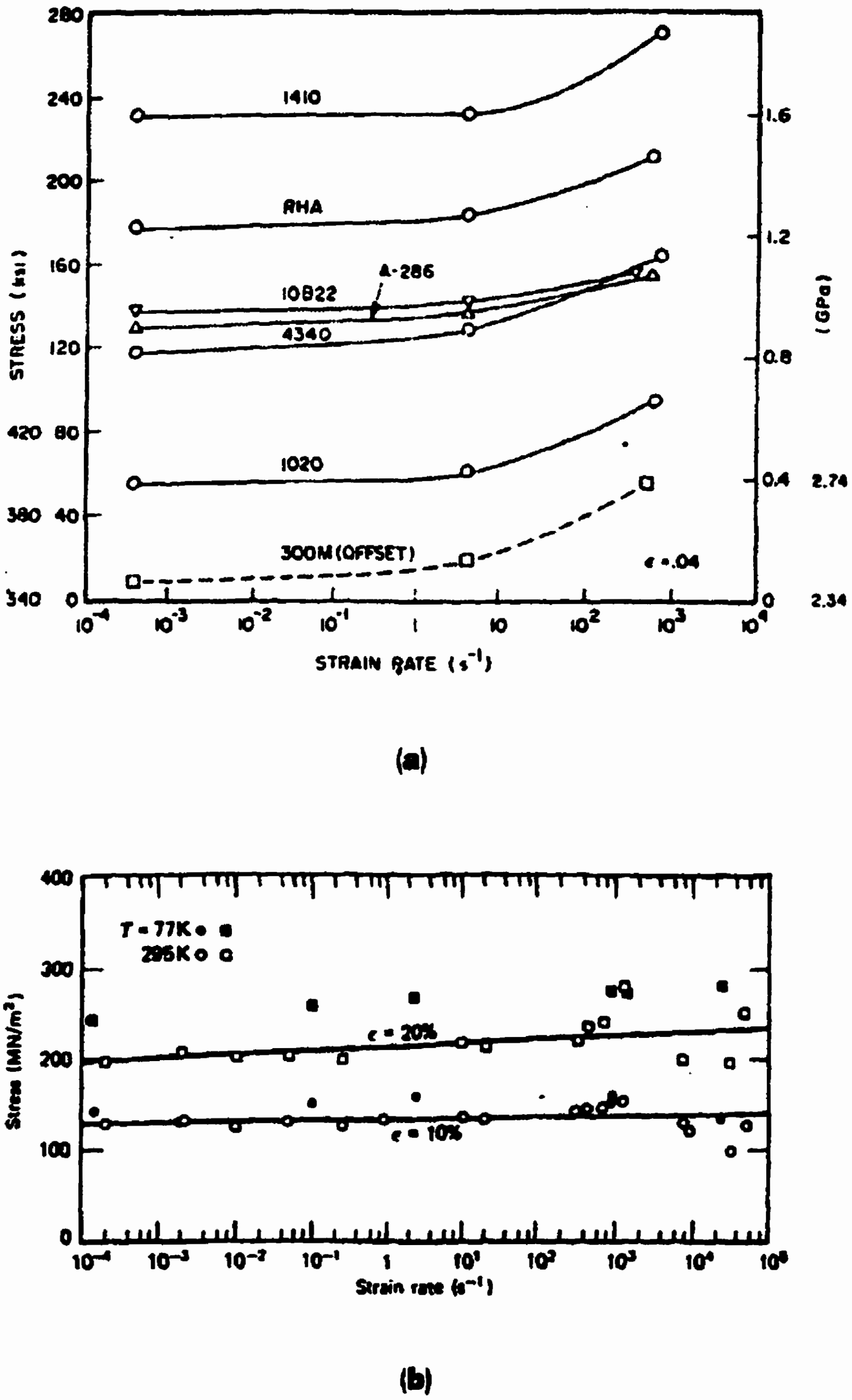

Figure 1.3: Strain Rate Dependence of Flow Stress For (a) Steel, and (b) Pure Copper [1]

In order for a dislocation to move a distance, it has to overcome the barrier with the energy

$$\Delta F^* = \int_{x_1}^{x_2} K dx \tag{1.8}$$

which is the Helmholtz free energy change, where dislocation moves a distance from x_1 to x_2 whereby it has to overcome the obstacle that produces a force K. The applied external shear stress exerts a force $\tau^* bl$ on a moving dislocation, where τ^* is the applied shear stress resolved in the slip plane, b is a Burger's vector, and l is the length of a dislocation. Therefore, the work done on moving dislocation by the applied shear stress is a product of a force on dislocation and the distance that the dislocation has to move

$$\tau^* b\, l(x_2 - x_1) = \tau^* V^* \tag{1.9}$$

where V^* is called the activation volume. This work is only a mechanical part of the whole energy required for the dislocation to move the distance from x_1 to x_2. Another part of the required energy is thermal energy (Gibbs free energy of activation)

$$\Delta G^* = \Delta F^* - \tau^* V^* \tag{1.10}$$

which is a difference between the total energy that dislocation has to overcome (equation (1.8)) and the mechanical part of the energy supplied to dislocation by the externally applied shear stress (equation (1.9)).

If it is assumed that a dislocation vibrates at certain frequency ν, then the dislocation will pass through the following number of obstacles per second

$$\nu \exp\left(\frac{\Delta G^*}{kT}\right) \tag{1.11}$$

The product of equation (1.11) and the distance that a dislocation moves between obstacles gives the average dislocation velocity

$$\overline{V} = d\nu \exp\left(\frac{\Delta G^*}{kT}\right) \tag{1.12}$$

where d is the distance moved by dislocation, k is Boltzmann's constant, and T is a temperature. When equation (1.7) is substituted into equation (1.12), the strain rate dependence of the flow stress is obtained

$$\dot{\gamma} = \rho_m b d \nu \exp\left(\frac{\Delta G^*}{kT}\right) \tag{1.13}$$

It was mentioned earlier that the flow stress is contained in the Gibbs free energy factor ΔG^*, and if equation (1.10) is substituted into equation (1.13), the flow stress dependence on the strain rate becomes clear

$$\dot{\gamma} = \rho_m b d \nu \exp\left(\frac{\Delta F^* - \tau^* V^*}{kT}\right) \tag{1.14}$$

Clifton *et al.* developed an equation for the plastic shear strain rate dependence of the flow stress for Aluminum for strain rates of up to 10^3 s^{-1} [26]

$$\dot{\gamma}^p = \varpi \exp\left(-\frac{[\tau^*(\gamma^p) - \tau]\, V^*}{kT}\right) \tag{1.15}$$

where τ^* is a stress barrier and V^* is activation volume. Like equation (1.14), equation (1.15) does not include the strain rate history effects pointed out in the introduction to this section. According to Malvern [22], the effects of strain rate history are complex, and the relation takes the form of

$$\underline{\dot{\varepsilon}}^p = f(\underline{\sigma}, T, S_1, S_2, \ldots)$$

where S_1, S_2,... are structure parameters that develop with time and deformation according to

$$\dot{S}_i = f_i(\underline{\sigma}, T, S_1, S_2, \ldots)$$

More information on strain rate history effects can be found in [16].

1.2.4 Temperature Dependence of Flow Stress

The flow stress depends also on temperature. As the temperature changes, the required externally applied load that constitutes the mechanical energy required by dislocations to move over obstacles, will also change. Figure 1.4 presents data for the stress dependence on temperature for different strain rates [27].

If the stress required for dislocation to overcome obstacle at 0 K is given by $\tau^*(0)$ and the stress required at any temperature is given by $\tau^*(T)$, than the Gibbs free energy change when dislocation moves certain distance is

$$\Delta G^* = \Delta F\left[1 - \frac{\tau^*(T)}{\tau^*(0)}\right] \tag{1.16}$$

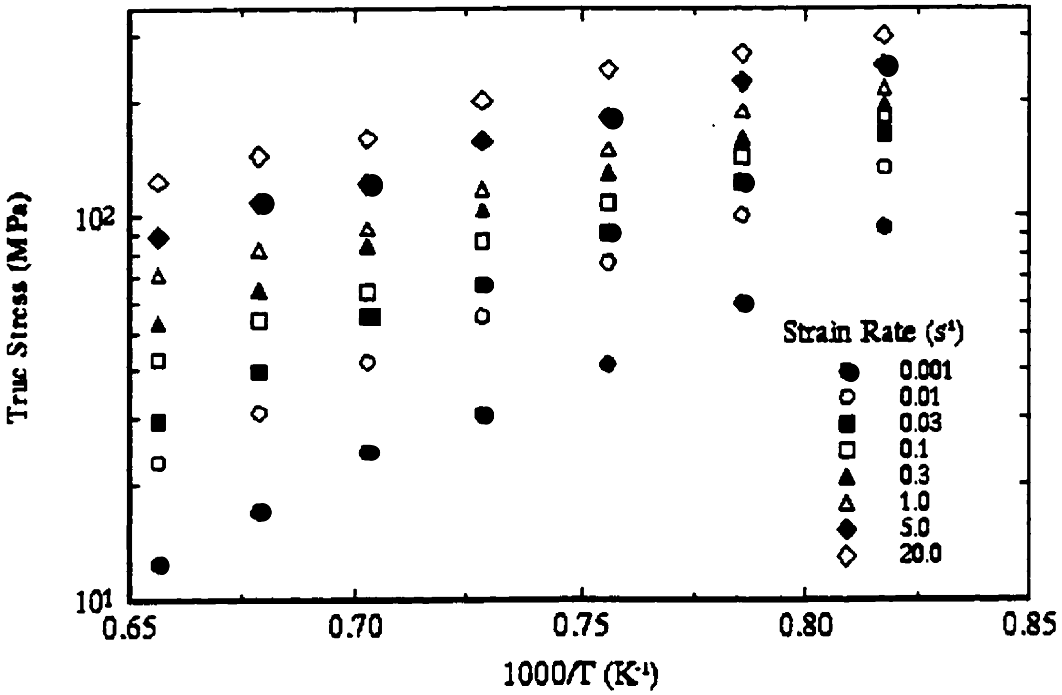

Figure 1.4: Temperature Dependence of Flow Stress [27]

Substituting equation (1.16) into equation (1.13) gives the flow stress dependence on temperature

$$\frac{\tau^*(T)}{\tau^*(0)} = \frac{kT}{\Delta F} \ln\left(\frac{\dot{\gamma}}{\rho_m b d v}\right) + 1 \tag{1.17}$$

There is a temperature above which the dislocations have enough thermal energy and are able to overcome obstacles with thermal activation alone. This temperature depends on the material and is labelled T_c. At this temperature, since the thermal energy is sufficient for overcoming obstacles, the required externally applied shear stress $\tau^*(T_c) = 0$. After making substitutions and rearrangements, the following temperature dependence of flow stress is obtained

$$\frac{\tau^*(T)}{\tau^*(0)} = \left(1 - \frac{T}{T_c}\right) \tag{1.18}$$

It is clear from the above equation that when the temperature reaches the temperature T_c, the required shear stress (mechanical part of the energy required) approaches zero.

1.3 HIGH STRAIN RATE INDUCED FAILURE

The failure of materials loaded in the high strain rate range differs considerably in its mechanisms from the failure induced by static and quasi-static loading. Certain material and physical factors that are not of interest in slow rate loading become of great importance in high rate loading and dominate the deformation mechanisms. Some of these influential properties include thermal softening that starts to predominate the deformation at rates beyond certain limit and plastic deformation is governed by the mechanical and thermal instabilities. Along with these instabilities, the inertial forces that are absent in low loading rates become an important factor in the material behaviour at high strain rates. Zener and Hollomon [3] first introduced the effect of thermal softening that starts to dominate over strain hardening at the point when thermo-mechanical instability first occurs. The following sections describe the important factors that govern the adiabatic shear band formation and mechanical instability that is responsible for the occurrence of the adiabatic shear bands.

1.3.1 Mechanical Instability At High Rates of Strain

When the material is deformed under the conditions of high strain rate, the deformation mechanism is very different than when the material is deformed in the static or quasi-static regime. While the deformation (plastic deformation) in the static and quasi-static regimes is considered to be in equilibrium, i.e., the dislocation motion and the formation of dislocation cell structures are allowed the time for the process, the case for high strain rate deformation is quite different. In this state, the part of the material exhibits the mechanical instability and localisation of plastic deformation takes place. It can be said that the plastic deformation is not uniform, but rather localised. This localisation of the deformation is also a case of the material failure whether or not accompanied by fracture [5, 7].

1.3.1.1 The Maximum Load Criterion

The criterion of maximum load for the description of instability has been used for a long time for the tensile quasi-static loading [28]. The maximum load criterion for the tensile loading states [29]

$$dL = \sigma dA + A\,d\sigma = 0 \tag{1.19}$$

where $dL = 0$ denotes the maximum value of the load, σ denotes the true stress, and A is a transient cross-sectional area.

In the shear, the cross-sectional area A is constant and the above maximum load criterion reduces to

$$\frac{dL}{A} = \frac{A\,d\sigma}{A} \Rightarrow d\tau = d\sigma = 0$$

or,

$$d\tau = 0 \tag{1.20}$$

which now represents the maximum stress criterion.

Shear stress is a function of strain , strain rate and a temperature and can be represented by

$$\tau = \tau(\gamma, \dot{\gamma}, \theta) \tag{1.21}$$

Substituting equation (1.21) into equation (1.20) we obtain

$$\left(\frac{\partial\tau}{\partial\gamma}\right)_{\dot{\gamma},\theta} + \left(\frac{\partial\tau}{\partial\dot{\gamma}}\right)_{\gamma,\theta}\left(\frac{\partial\dot{\gamma}}{\partial\gamma}\right) + \left(\frac{\partial\tau}{\partial\theta}\right)_{\gamma,\dot{\gamma}}\left(\frac{d\theta}{d\gamma}\right) = 0 \tag{1.22}$$

Two assumptions are made: (1) the deformation is adiabatic and (2) the change of the strain rate during the deformation is negligible, i.e., $\partial\dot{\gamma}/\partial\gamma \simeq 0$ [30, 31]. Energy conservation states that all the plastic work done during deformation is converted into heat (adiabatic assumption)

$$\rho c\, d\theta = K\tau\, d\gamma \tag{1.23}$$

In equation (1.23), K is a constant that is, according to Taylor and Quinney, equal to 0.9 - 0.95 [32]. For the sake of simplicity, K is assumed to be 1. Substituting equation (1.23) into equation (1.22) and taking into consideration the two assumptions previously made, we obtain

$$\left(\frac{\partial\tau}{\partial\gamma}\right)_{\dot{\gamma},\theta}\frac{\rho c}{\tau} = \left(-\frac{\partial\tau}{\partial\theta}\right)_{\gamma,\dot{\gamma}} \tag{1.24}$$

With the assumptions of adiabatic conditions and that strain rate does not change during the plastic deformation, the above equation states that the two opposing and rival effects, strain hardening $\partial\tau/\tau\,\partial\gamma$, and thermal softening $(-\partial\tau/\partial\theta)/\rho c$, are equal at the onset of instability. When thermal softening outweighs the strain hardening, the adiabatic shear band will form. More on the individual factor influence on the ASB formation is presented in the section 1.3.2.

In order to obtain tangible criteria for instability, significant work has been done to adopt the ***instability strain*** as the instability criterion. Table 1.1 lists some of the constitutive equations used by different authors to obtain the instability strain γ_i [8, 10, 30, 33, 34, 35, 36]. All the constitutive equations were derived from the equation (1.24). All the equations for the instability strain γ_i say that materials with lower strain hardening exponent n, and higher value of the thermal softening, will have lower value for the instability strain , and therefore will be more susceptible to ASB formation. This is in agreement with the experimental values on ASB formation obtained for different materials (Table 1.2).

Dodd and Atkins [37] derived the instability criterion based on the maximum shears stress criterion, but took into account the void growth and its influence on the softening. The maximum load/stress criterion is now

$$\frac{d\tau}{dA} = -\frac{\tau}{A} \tag{1.25}$$

where $A = W(L-H)$, and W is the width of the gauge length, L is a length of the gauge section, and H is the sum of characteristic diameters of all individual voids. The void growth rate is

$$\dot{H} = \dot{\gamma}\left(a + \frac{b\sigma_H}{\sigma_y}\right) \tag{1.26}$$

where σ_H is a hydrostatic stress, and σ_y is a yield stress. With assumptions of (1) adiabatic conditions and (2) that critical strain for void nucleation γ_c is less than the instability strain for ASB formation γ_i, it follows that the instability strain is [28]

Table 1.1: Instability Criteria for Maximum Shear Stress

		Constitutive Relation	*Instability Strain*
Linear strain hardening with yield strength	1	$\tau = A(1 + a\gamma)$	$\gamma_i = \frac{\rho c}{(-\partial\tau/\partial\theta)} - \frac{1}{a}$
	2	$\tau = A(1 + a\gamma)\exp(-\beta\gamma)$	$\gamma_i = \frac{1}{\beta_1} - \frac{1}{a}$ where $\beta_1 = \beta + \frac{(-\partial\tau/\partial\theta)}{\rho c}$
Power law without yield strength	3	$\tau = A\gamma^n$	$\gamma_i = \frac{n\rho c}{(-\partial\tau/\partial\theta)}$
	4	$\tau = A\gamma^n\exp(-\beta\gamma)$	$\gamma_i = \frac{n}{\beta_1}$
	5	$\tau = A\gamma^n\dot{\gamma}^m\exp\left(\frac{W}{\theta}\right)$	$\gamma_i = \left\{\frac{n\rho c}{AW}\frac{\theta^2}{\dot{\gamma}m}\exp\left(-\frac{W}{\theta}\right)\right\}^{1/(n+1)}$
	6	$\tau = A\gamma^n\dot{\gamma}^m\theta^{-\nu}$	$\gamma_i = \left\{\frac{n\rho c}{A\nu}\frac{\theta^{\nu+1}}{\dot{\gamma}^m}\right\}^{1/(n+1)}$
	7	$\tau = A\gamma^n(1 + b\dot{\gamma}^m)(1 - c_1\theta)$	$\gamma_i = \left\{\frac{n\rho c}{Ac_1}\frac{1}{(1 + b\dot{\gamma})^m}\right\}^{1/(n+1)}$
Power law with yield strength	8	$\tau = A(1 + a\gamma^n)\left(1 + b\ln\frac{\dot{\gamma}}{\dot{\gamma}_0}\right) \times \frac{\theta_M - \theta}{\theta_M - \theta_0}$	$\gamma_i = \frac{n\rho c(\theta_M - \theta_0)}{A(1 + a)} - \frac{\gamma_i^{1-n}}{a}$

References: equation #1 - [8, 33], #2 - [34], #3 - [30], #4 - [34], #5 - [35], #6 - [35], #7 - [36], #8 - [10]

Table 1.2: Susceptibility of Metals to ASB [28]

Material	$(-\partial\tau/\partial\theta)$ (kPa/K)	n	γ_{theo}	γ_{exp}
OFHC copper		0·32	5·3	5·8
Cartridge brass		0·34	3·7	3·0
2024-T 351 Al		0·34	0·66	0·50
7039 Al		0·41	0·77	0·55
6061 T6 Al	496	0·075	0·438	0·35
Nickel 200		0·32	0·03	0·18
Armco IF iron		0·25	4·3	4·1
Carpenter electrical iron		0·43	4·4	5·8
Low carbon steel	423	0·04	0·36	0·28
1006 steel		0·36	3·3	3·5
1018 CRS steel		0·05		0·16
1020 steel	633	0·28	1·94	1·2
RHA steel		0·37	1·2	1·1
AMS 6418 steel		0·18	0·16	0·20
S-7 Tool steel		0·18	0·16	0·50
AISI 4340 steel				
Tempering temp.:				
466°C	1 120	0·054	0·17	0·2–0·23
238–321 °C	1 610–1 780	0·042–0·047	0·09	<0·11
516 °C	1 020	0·061	0·22	0·22–0·26
579 °C	790	0·073	0·33	0·29–0·33
α-Ti		0·17	0·326	1·15
CP-Ti	595	0·104	0·46	0·50
Tungsten alloy (7% Ni, 3% Fe)		0·12	0·03	0·18
Depleted uranium (0·75 Ti)		0·25	0·23	0·25

$$\gamma_i = \frac{n}{\frac{-\partial\tau/\partial\theta}{\rho c} + \frac{\alpha + \beta\sigma_H/\sigma_y}{1 - (\gamma_i - \gamma_c)(\alpha + \beta\sigma_H/\sigma_y)}} \tag{1.27}$$

where $\alpha = a/L$, and $\beta = b/L$. This criterion takes into account both thermal softening and geometrical softening caused by the void nucleation and growth. The validity of the criterion is demonstrated by observing that as the strain hardening coefficient n increases, the value of the instability strain, γ_i, increases, thus making the material less susceptible to the ASB. As the thermal softening factor, $-\partial\tau/\rho c\,\partial\theta$, increases, the material becomes more susceptible to ASB since the value of instability strain decreases.

1.3.1.2 The Localisation Criterion

The maximum load criterion discussed in the previous section does not mention the localisation, which is an integral part of the adiabatic shear band formation. It also does not take into account the effect of the strain rate sensitivity of the material. Another approach to defining the instability at the onset of ASB nucleation is to take into account the degree of inhomogeneities at different locations in the deforming body, and to compare it to the uniform body without defects. The criterion says that if the inhomogeneity is amplified during the deformation, the localisation will occur. If the inhomogeneity is not amplified, there will be no localisation [28].

If the inhomogeneity is defined as $\frac{\Delta \ln \dot{\gamma}}{\Delta \ln \gamma}$, where Δ stands for the difference between the inhomogeneity and the uniform body, the equation can be written,

$$\frac{\Delta \ln \dot{\gamma}}{\Delta \ln \gamma} = \chi \tag{1.28}$$

By solving the equation with respect to time t, the following is obtained

$$\frac{\Delta\gamma}{\Delta\gamma_0} = \left(\frac{\gamma}{\gamma_0}\right)^{\chi} \tag{1.29}$$

where γ_0 stands for the initial strain. From equation (1.29) we can write

$$\frac{\Delta\gamma}{\gamma} = \left(\frac{\gamma}{\gamma_0}\right)^{\chi-1}\frac{\Delta\gamma_0}{\gamma_0} = k(\gamma)\frac{\Delta\gamma_0}{\gamma_0} \tag{1.30}$$

where $k(\gamma) = (\gamma/\gamma_0)^{\chi-1}$ is the amplification factor of relative localisation. For the simple shear, the cross-sectional area remains constant, and by using the constitutive relation #6 from Table 1.1, $\tau = A\,\gamma^n\,\dot{\gamma}^m\,\theta^{-\nu}$, we obtain

$$\frac{\Delta\tau}{\tau} = m\frac{\Delta\dot{\gamma}}{\dot{\gamma}} + n\frac{\Delta\gamma}{\gamma} - \nu\frac{\Delta\theta}{\theta} = 0 \tag{1.31}$$

This criterion says that there has to exist the amplification of the inhomogeneity in order for the localisation to occur. It means that the amplification factor $k(\gamma)$ has to be greater then unity. For $k(\gamma) \geqslant 1$, there has to be $\chi \geqslant 1$. Therefore, $\chi = 1$ marks the onset of localisation. Now, from equation (1.28), the criterion becomes

$$\frac{\Delta\ln\dot{\gamma}}{\Delta\ln\gamma} = 1 \tag{1.32}$$

Assuming the adiabatic conditions and substituting equation (1.32) into equation (1.31) the instability criterion is obtained

$$\gamma_i = \frac{(m+n)\rho c \theta}{\tau \nu} \tag{1.33}$$

This instability criterion derived from the localisation phenomenon is different from instability criteria derived from the maximum stress criterion. First, it takes into account the strain rate sensitivity m which maximum stress criterion fails to achieve. Also, it takes into account both strain hardening, n, and strain rate sensitivity, m, separately.

By examining both maximum stress and localisation criteria, it is obvious that in order to describe the process of formation of adiabatic shear band, it is necessary to take into account localisation as well as strain hardening and thermal softening.

1.3.1.3 Model for ASB Width

The above models based on maximum stress and localisation can tell whether the ASB will or will not form and when it will form. They do not, however, say anything about the extent of the deformation, specifically the size of the adiabatic shear band. In this subsection, the theoretical model for estimating the adiabatic shear band width will be discussed.

According to Bai [28], the process of adiabatic shear band formation can be described by four different steps, each step being the necessary predecessor of the next one. These four steps in a way represent the theoretical model of the ASB nucleation, growth, and the final geometry. These four steps are:

(1) Scaling. The first step is to properly scale equations used in the ASB description [38],

(2) Wave Trapping and Momentum Diffusion - Early Regime. Heat diffusion is neglected in this early stage [39],

(3) Heat Diffusion in Localisation - Intermediate Regime.

(4) Late State Analysis. Describes the final ASB geometry.

Here, in this section, the last regime, i.e., the final ASB geometry model will be described. The following mathematical approximation gives the estimate only of the fully formed ASB. However, it has been suspected that adiabatic shear bands may not always grow unrestricted, but can be truncated [28].

The governing equations for the ASB formation are

$$\rho \frac{\partial^2 \gamma}{\partial t^2} = \frac{\partial^2 \tau}{\partial y^2} \tag{1.34}$$

$$\tau \frac{\partial \gamma}{\partial t} = \rho c \frac{\partial \theta}{\partial c} - k \frac{\partial^2 \theta}{\partial y^2} \tag{1.35}$$

$$\tau = \tau(\gamma, \dot{\gamma}, \theta) \tag{1.36}$$

In the intermediate regime, i.e., heat diffusion consideration, the rate of change of the ASB width, δ, can be described by taking the boundary velocity to be

$$v = \int_0^\delta \dot{\gamma}\, dy = \dot{\gamma}_* \int_0^\delta \left(\frac{\theta}{\theta_*} + \frac{\tau}{\tau_*} - 1 \right) dy = \frac{\dot{\gamma}_*}{\theta_*} \left(\int_0^\delta \theta\, dy - \theta_\delta(t) \delta(t) \right) \tag{1.37}$$

where the subscript * denotes the reference quantity. By differentiating equation (1.37) with respect to time and constant velocity boundary conditions, the following equation is obtained

$$\frac{\partial\theta}{\partial y}\Big|_{\delta}\,\delta(t)\frac{d\delta}{dt} = \frac{\tau(t)v}{\rho c} + \frac{k}{\rho c}\frac{\partial\theta}{\partial y}\Big|_{\delta} - \delta(t)\frac{\partial\theta}{\partial t}\Big|_{\delta} \qquad (1.38)$$

Equation (1.38) can be rewritten as

$$\frac{d\delta}{dt} = \frac{\dfrac{\tau(t)\bar{\dot{\gamma}}(t)}{\rho c} + \dfrac{k}{\rho c}\left(\overline{\dfrac{\partial^2\theta}{\partial y^2}} - \dfrac{\partial^2\theta}{\partial y^2}\Big|_{\delta}\right)}{\dfrac{\partial\theta}{\partial y}\Big|_{\delta}} \qquad (1.39)$$

which gives the rate of change of the ASB width, where the bar on top of the quantity represents the average value of the quantity in the shear band. Figure 1.5 clarifies some of the boundary conditions used to develop the above equations.

At the late state, it is assumed that the adiabatic shear band is completely formed, unhindered by any mechanism that may have caused truncating of the band. By solving equations (1.34) and (1.35), the following solution is obtained for the band halfwidth

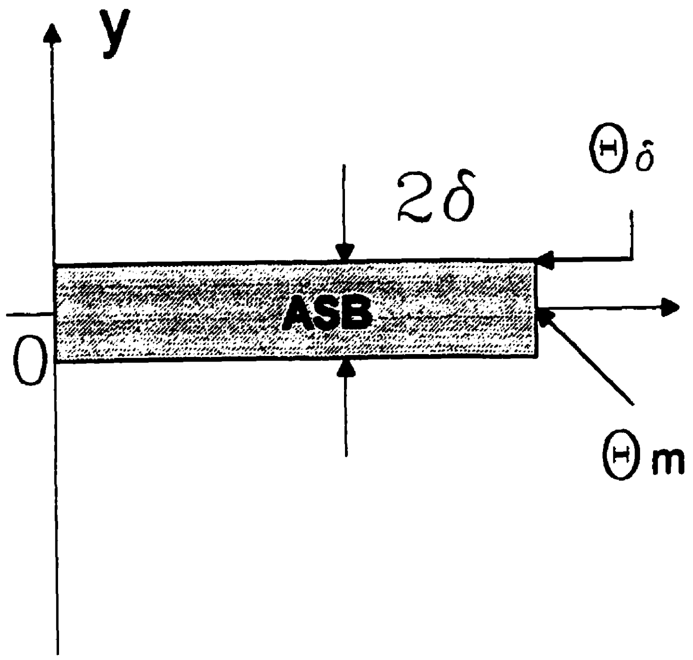

Figure 1.5: Boundary Conditions

$$\begin{aligned}
\tau &= \tau(t) \\
y &= \int_{\theta}^{\theta_m} \frac{d\zeta}{\sqrt{\int_{\zeta}^{\theta_m} \tau(t) g(\tau(t), \eta) d\eta}} \\
\delta(t) &= \int_{\theta_\delta}^{\theta_m} \frac{d\zeta}{\sqrt{\int_{\zeta}^{\theta_m} \tau(t) g(\tau(t), \eta) d\eta}}
\end{aligned} \tag{1.40}$$

where θ_m is a temperature at the centre of the band, and θ_δ is a temperature at the boundary of the band at $y = \delta$ which is a halfwidth of the band. Simplified equation describing the halfwidth of the band δ is obtained by balancing the heat source and heat transfer terms

$$\delta(t) \simeq \sqrt{\frac{\kappa\theta_*}{\tau_* \dot{\gamma}_*}} \tag{1.41}$$

Table 1.3 shows the comparison between adiabatic shear band width obtained from these mathematical models, and from the experiments.

Table 1.3: Comparison of Calculated and Experimental Values for ASB Width [40]

		Al	*Cu*	*Mild steel*
τ_f	(MPa)	~300	~200	~300
θ_M	(K)	775–877	1 355	1 800
λ	(W/(mK))	236	403	50
η	(kPa s)	2·1	3·6	2·8, 2·1
$2\delta_{pred}$	(mm)	0·14	0·44	0·11
$2\delta_{exp}$	(mm)		0·34	0·19

		Low carbon steel	*Tool steel*	*CP-titanium*
λ	(W/(mK))	48	40	17
$\Delta\theta_*$	(K)	201	241	265
τ_*	(MPa)	430	1 169	435
$\dot{\gamma}_*$	(s^{-1})	2 226	1 548	2 283
$2\delta_{pred}$	(mm)	0·1	0·073	0·067
$2\delta_{exp}$	(mm)	0·13–0·17	0·1	0·06–0·10

1.3.2 Factors Governing ASB Formation

In this section, it will be explained what material factors are responsible for the emergence of the adiabatic shear band. It is known [28] that the formation of the ASB is a process that is so complex, that it is very difficult to narrow down and pinpoint all the parameters that play role in its formation. Besides the material variables, other factors, such as stress distribution, loading conditions and type of the specimen, also play an important role in the process of destabilisation of the material and nucleation of the ASB.

In light of the material properties that influence the ASB, the following variables are of the interest

ρ - Density $\left(\frac{kg}{m^3}\right)$

c - Specific Heat $\left(\frac{m^2}{s^2 {}^\circ C}\right)$

α - Thermal Diffusivity $\left(\frac{m^2}{s}\right)$

$\frac{\partial \tau}{\partial \gamma}$ - Strain Hardening Factor $\left(\frac{kg}{ms^2}\right)$

$\frac{\partial \tau}{\partial \theta}$ - Thermal Softening Factor $\left(\frac{kg}{ms^2 {}^\circ C}\right)$

$\frac{\partial \tau}{\partial \dot{\gamma}}$ - Strain Rate Sensitivity Factor $\left(\frac{kg}{ms}\right)$

$\dot{\gamma}$ - Strain Rate $\left(\frac{1}{s}\right)$

τ - Shear Stress $\left(\frac{kg}{ms^2}\right)$

γ - Shear Strain

All variables are material variables except the strain rate, shear stress and shear strain, which are the description of the stress state.

The combination of the above variables gives four dimensionless numbers that govern the ASB formation. These numbers are

$$Pr = \frac{\tau}{\rho\dot{\gamma}a}$$ Effective Prandtl Number, ~ 10^6 for mild steel [28]

$$N = \frac{\partial\tau}{\tau\,\partial\gamma}$$ Strain Hardening, ~ 10^{-1} for mild steel

$$S = \frac{-\partial\tau/\partial\theta}{\rho c}$$ Thermal Softening, ~ 10^{-1} for mild steel

$$m = \frac{\dot{\gamma}\,\partial\tau}{\tau\,\partial\dot{\gamma}}$$ Strain Rate Sensitivity, ~10^{-2} for mild steel

From these dimensionless parameters that describe the initiation of the ASB, only strain hardening N and thermal softening S are competitive. That means that during the deformation, there will be both thermal softening and strain hardening dominating, and depending which one takes over the control, the adiabatic shear band will or will not form.

Two main assumptions are considered here: (1) deformation is adiabatic (there is no heat escape from the region under deformation), and (2) rate effects are negligible. The first assumption of adiabatic condition requires that thermal diffusivity $a = 0$. Under this assumption, the effective Prandtl Number Pr, will be equal to infinity and will not play role in the deformation process.

Since we are left with two major competitors for the role of control over the deformation process and ASB formation, namely strain hardening, N, and thermal softening, S, the following dimensionless number (or parameter) is formed,

$$B = \frac{S}{N} = \frac{-\frac{\partial \tau}{\partial \theta}\tau}{\rho c \frac{\partial \tau}{\partial \gamma}} \tag{1.42}$$

This factor considers the effects of thermal softening and strain hardening and can serve as the approximate basis for determining the process of deformation, especially if it is rewritten in the form

$$\left(-\frac{\partial \tau}{\partial \theta}\right) \geq \frac{\rho c \frac{\partial \tau}{\partial \gamma}}{\tau} \tag{1.43}$$

The above relation states that when thermal softening outweighs the strain hardening, the adiabatic shear band will form. Another relation developed by Staker [33] using the contained exploding cylinder (CEC) technique is analogous to equation (1.43) in view of the two leading processes taking place, thermal softening and strain hardening. Staker defined the critical shear strain γ, representing the strain hardening, as opposed to the thermal softening factor $\rho cn/(-\partial\tau/\partial\theta)$. In the mathematical form it states

$$\gamma = \frac{\rho c n}{\left(-\frac{\partial \tau}{\partial \theta}\right)} \tag{1.44}$$

When plotted, the following curve is obtained (figure 1.6)

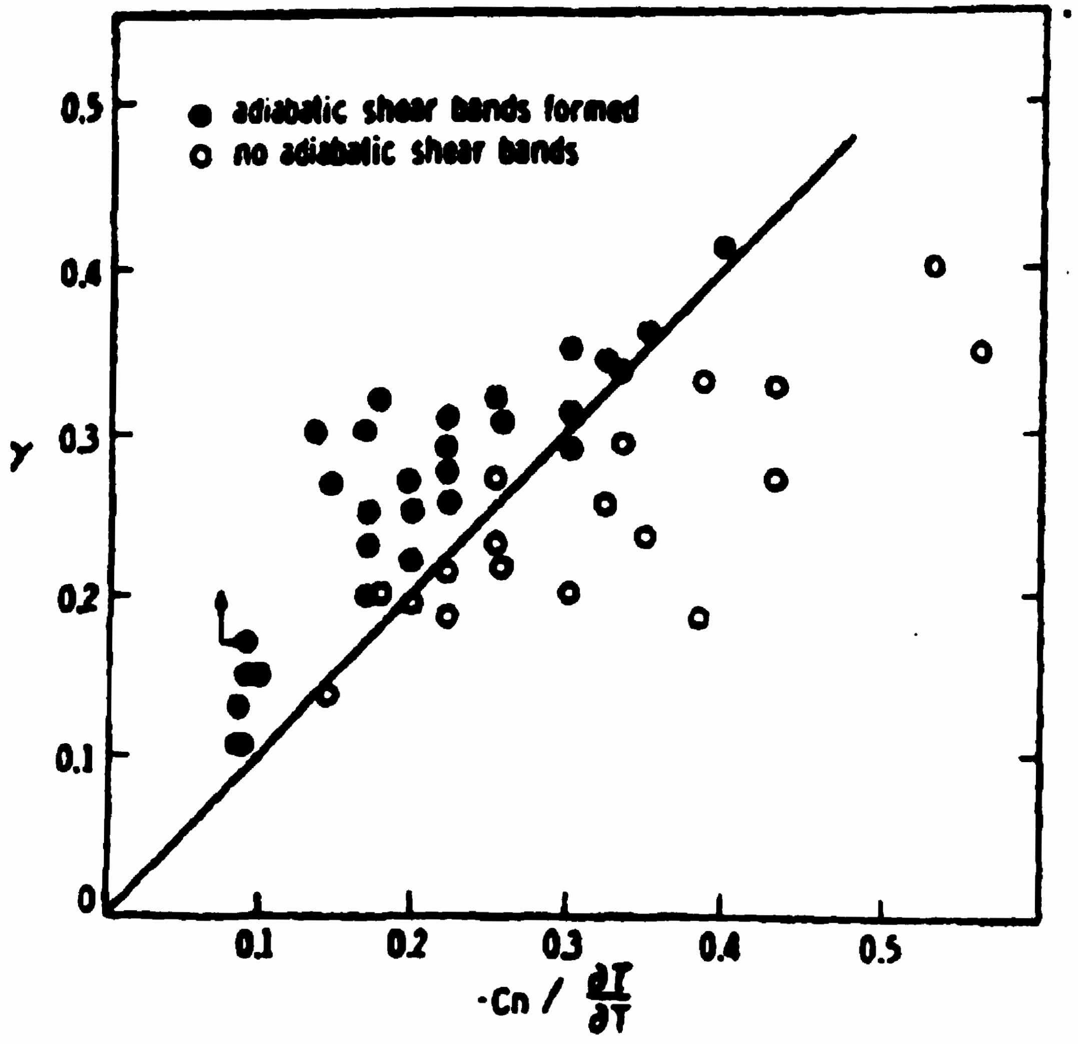

Figure 1.6: The Relation Between Measured True Shear Strain and Material Parameter $\rho cn/(-\partial\tau/\partial\theta)$ Defining the Shear Instability [33]

At the beginning of this section, it was mentioned that the assumption was that the process was totally adiabatic. This means that there is no heat exchange between the ASB region and the surrounding matrix material. However, this is not quite true. If totally adiabatic conditions were to exist, than the thermal diffusivity coefficient a would have to be zero which is not the case for any metal. However, as the diffusivity coefficient a approaches zero, the thermal conditions approach that of adiabatic conditions. Thus, the lesser the thermal diffusivity, the more susceptible material is to the ASB formation. This fact comes from the thermal instability that exists between the deformed region and surrounding matrix since the heat generated during plastic work cannot escape the region because of the low coefficient of thermal diffusivity, and thus the dimensionless parameter S (thermal softening) outweighs the strain hardening number N. Table 1.4 presents some data on the coefficient a for different materials. It is seen that the value for Titanium (Ti) is the smallest on the list and the value for the Copper (Cu) is the largest. This means that Ti is more susceptible to ASB formation than other metals, and that Copper is the least susceptible to ASB formation. Figure 1.7 shows the graphical representation of the material susceptibility to adiabatic shear band formation depending on the coefficient of thermal diffusivity [41]. This is in agreement with the experimental data on ASB formation in different metals. Therefore, the coefficient of thermal diffusivity is yet another factor entering the equation of susceptibility of material to ASB.

So far, the effects of strength and hardness of the material on the ASB formation have not been mentioned. Nevertheless, these two factors also influence the deformation process. It was observed by some researchers [42, 43] that the adiabatic shear bands are more pronounced in high strength materials than in the different treated lower strength materials of the same composition. This means that ASB favours high strength and high hardness, although the material is the same, just the heat treatment is different. One explanation is that high strength steels need to dissipate more energy that is converted into heat in order to achieve the same deformation than the lower strength steels. Another explanation comes from the fact that the strain hardening exponent n decreases with the

Table 1.4: Physical Properties of the Selected Metals [28]

	ρ ($10^3\ kg/m^3$)	c ($J/(kg\,.\,K)$)	*Debye temperature* (K)	*Melting temperature* (K)	*Molal volume* ($10^{-6}\ m^3/$ *mole*)	k ($W/(m\,.\,K)$)	α ($10^{-4}\ m^2/s$)
Li	0·534	3 570	343	452	12·7	71	0·372
Al	2·70	903	428	933	10·0	238	0·974
Cu	8·96	385	345	1 356	7·1	400	1·16
Fe	7·87	449	462	1 808	7·1	82	0·232
Ni	8·90	444	453	1 726	6·7	90	0·228
Ti	4·54	522	420	1 948	10·6	19	0·08

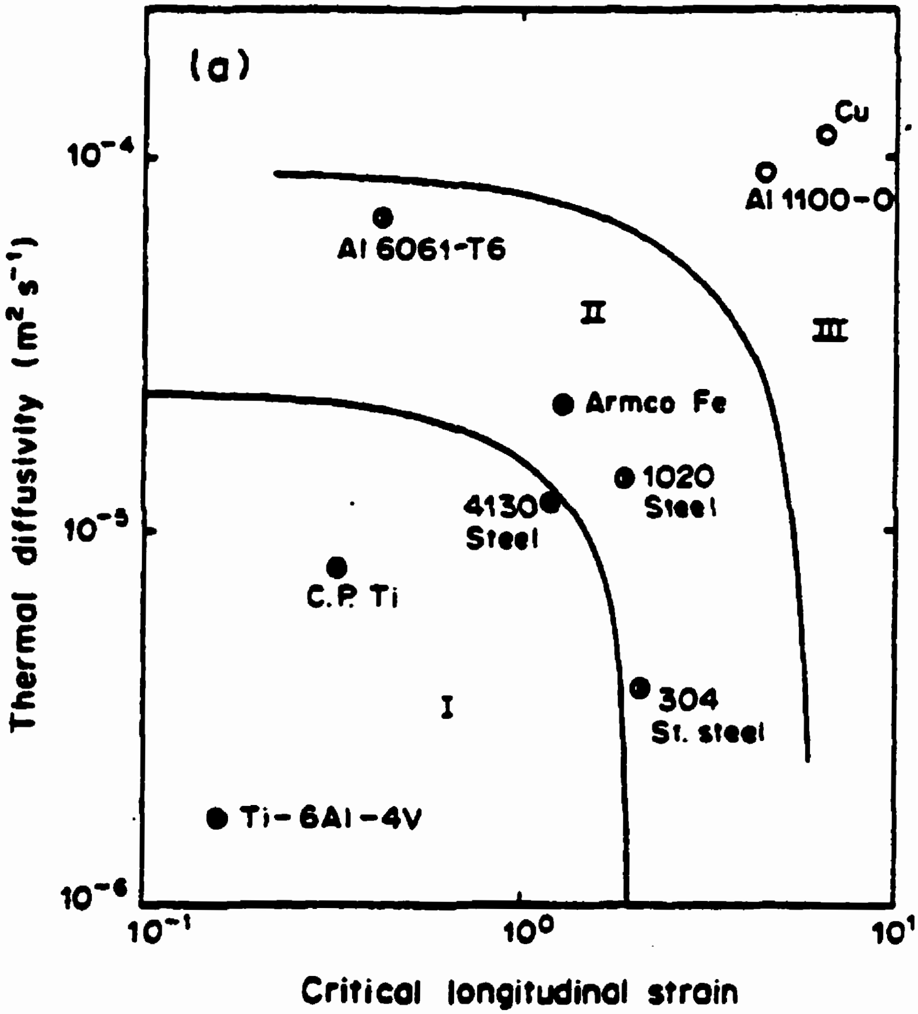

Figure 1.7: Thermal Diffusivity Coefficient in Relation to ASB Formation [41]. Black circles represent transformed ASB, half black-half white circles represent deformed band, white circles represent no ASB formed.

increase in the strength of the material [44]. Figure 1.8 demonstrates this observation for different steels. Since higher strength steels have a lower strain hardening exponent and the same thermal properties as their lower strength counterparts, it means that thermal softening will dominate the deformation in high strength steels, while the strain hardening dominates the deformation process for their counterparts.

Table 1.2 shows data for different metals. It can be seen that Copper has the combination of the low thermal softening coefficient (first column) and high strain hardening exponent, while high strength steels have the opposite; the high thermal softening coefficient and low strain hardening exponent. These results confirm findings by Staker, Shockey and Rogers [33, 42, 43] that higher strength materials are more susceptible to ASB.

It is also observed from Table 1.2 that the critical shear strain (γ) is different for different materials. It is calculated using equation (1.43), and can serve as an estimate to how much the material is susceptible to ASB. It is observed from Table 1.2 that Copper which has low susceptibility to ASB has very high value of critical shear strain, while high strength alloy steels have very low value of critical shear strain. Therefore, the lower the value of the critical shear strain, the more susceptible material is to ASB formation.

Another material property with effect on the formation of adiabatic shear band is the thermal conductivity k (W/m°C). Batra and Kim [45] reported results on influence of the thermal conductivity on ASB formation and behaviour. The material under investigation was structural steel with all material properties constant except thermal conductivity which was changed in the computer simulation from 0 to 5000 W/m°C with increments of the order of magnitude. The use of three different computer codes enabled the authors to examine the sole effect of thermal conductivity, keeping all other physical material properties constant which would be impossible in the conventional test where different heat treatments need to be applied to

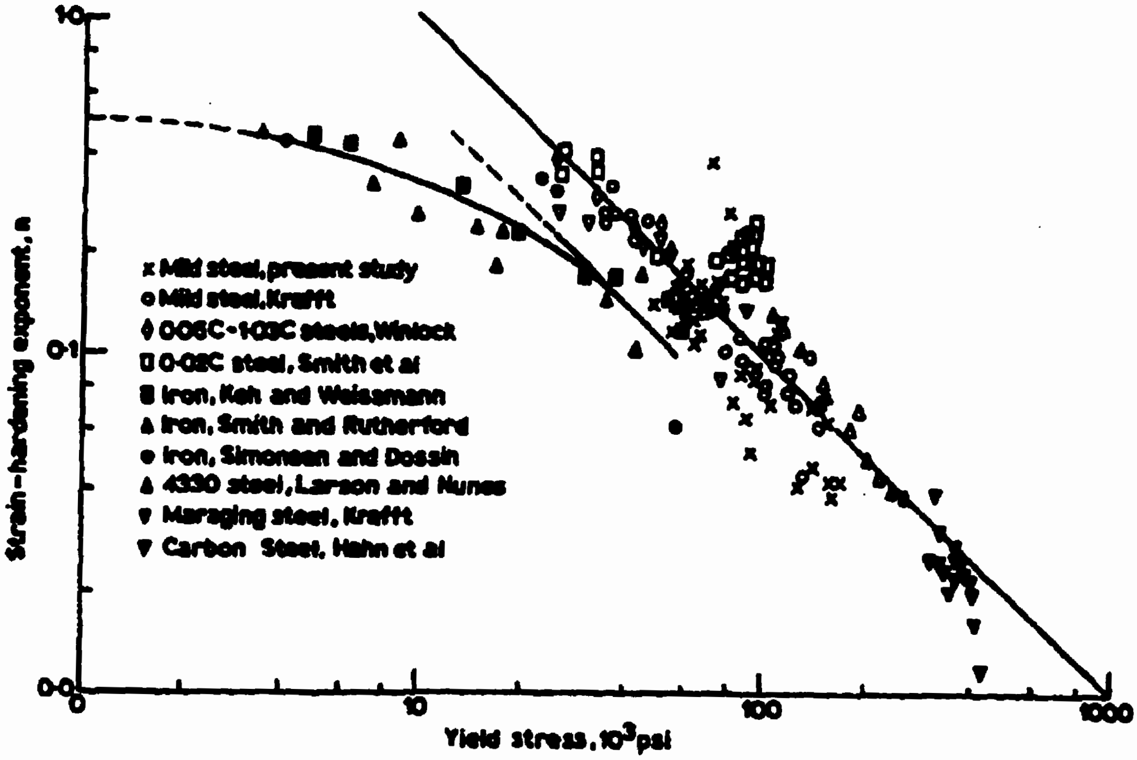

Figure 1.8: Effect of Strength on the Strain Hardening Exponent [44]

each specimen which in turn changes, though slightly, the same properties that need to remain constant. Another advantage of using computer codes is that in order to examine the influence of the wide range of the thermal conductivity on ASB using conventional test methods, it would require the use of different materials, since the values of thermal conductivity changes only slightly with the heat treatment [28], and therefore the values obtained would not be comparable. The results are presented in figure 1.9, and it is seen that as the thermal conductivity increases, there is a less obvious sharp drop in the stress which is a characteristic for a shear band formation [46]. Also, immediately after the stress reaches its maximum value, there is an abrupt temperature rise within a band (Figure 1.9 b) which decreases with the increase in the thermal conductivity. The width of the ASB is also affected, and increases as the value of thermal conductivity increases (Figure 1.9 c). All these numerical results are in agreement with the previous discussion on influence of the material properties on the formation and behaviour of ASB.

Zhu and Batra have shown [47] that at the time point of initiation of the adiabatic shear band, the strain rate becomes larger for the greater coefficient of thermal softening and is smaller for the lower coefficient of thermal softening. Again this numerical study was performed on the same material parameters, only the coefficient of thermal softening being changed.

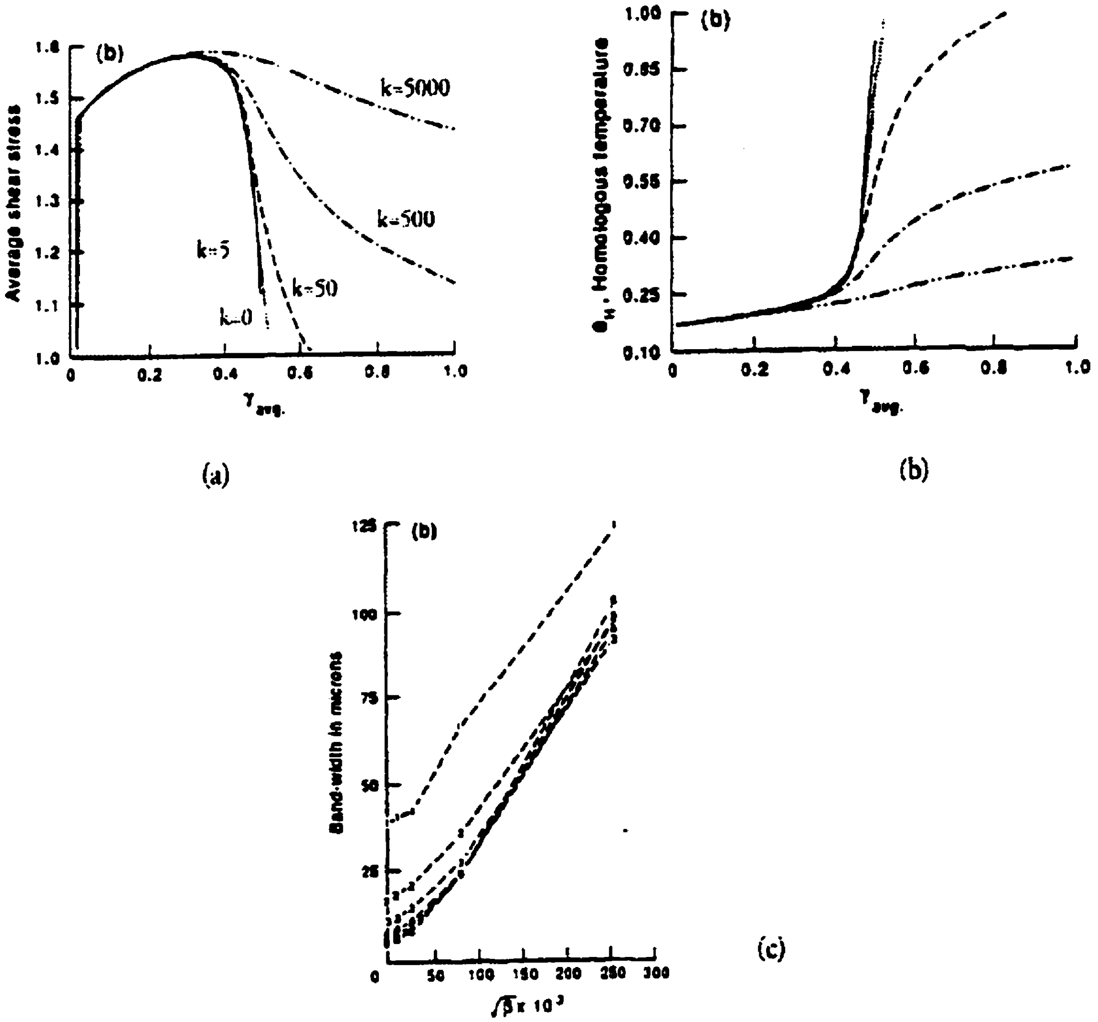

(a)

(b)

(c)

k in W/m deg.C. β is non-dimensional thermal conductivity

Figure 1.9: Influence of Thermal Conductivity *k* on Stress, Temperature and ASB Width [45]

1.3.3 Adiabatic Shear Bands

Adiabatic Shear Band (ASB) is a widely accepted name for the very narrow region of a localised plastic deformation characterised by a very large value of plastic strain. The word adiabatic assumes that there exists adiabatic thermal condition during the deformation so that there is no heat exchange between the locally deforming region and the surrounding matrix material. The mechanism of ASB formation will be discussed in section 1.3.4, but it is worth noting again, that the basic principle of ASB formation lies in the rivalry between the strain hardening and thermal softening as first suggested by Zener and Hollomon in 1944 [3]. If the rate of thermal softening exceeds the rate of strain hardening, the material exhibits localised weakening and the ASB forms.

The adiabatic shear bands are normally classified into two categories: deformed or transformed bands. This classification was made in 1944 by Beckman and Finnegan [48] who observed white bands after etching with a Nital solution. Whether a band is termed transformed or deformed, depends whether the phase transformation occurred within a band. What type of ASB will exist depends on material and also on other factors, such as loading conditions, testing temperature and the rate of strain [28]. Transformed bands are usually found in materials that undergo a phase transformation such as iron, steel, uranium and titanium alloys. Normally, transformed bands appear white after etching (Figure 1.10) and have distinct boundaries and well-defined width [49]. Local shear strains within a transformed bands were reported to be as high as 100 with the local shear strain rates in the range from 10^6 to 10^7 s^{-1} [49, 50, 51]. The width of the band ranges from 10 μm to 100 μm and decreases as the hardness increases (figure 1.11) [52, 53].

The deformed ASBs usually form in a materials that do not undergo a phase transformation and that have higher thermal diffusivities like copper and aluminum [41]. The characteristic of the deformed type of the band is an extensive localised shear

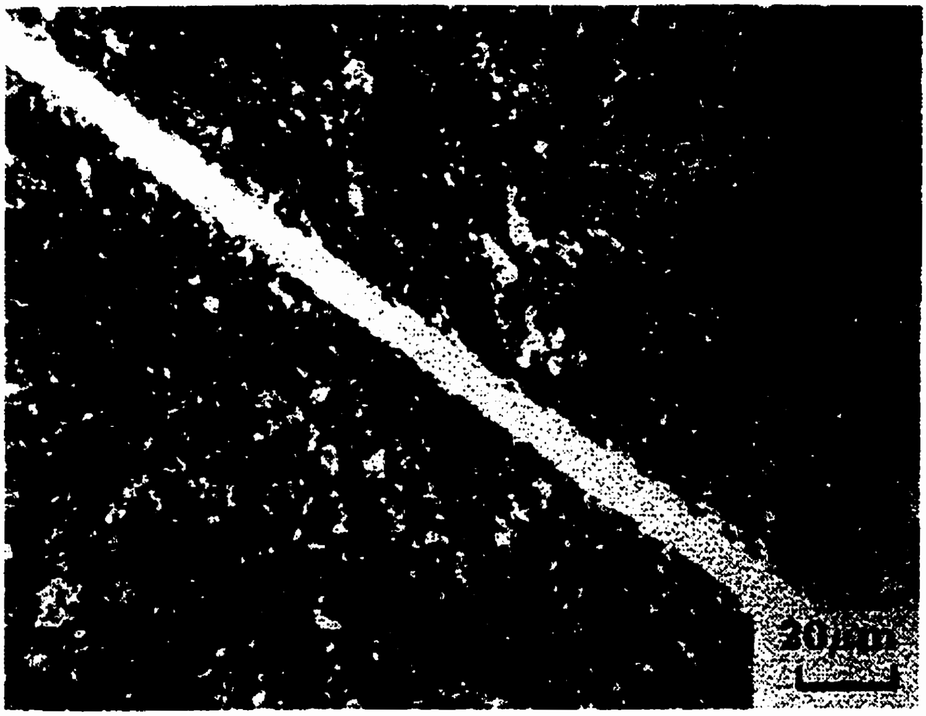

Figure 1.10: Transformed ASB [54]

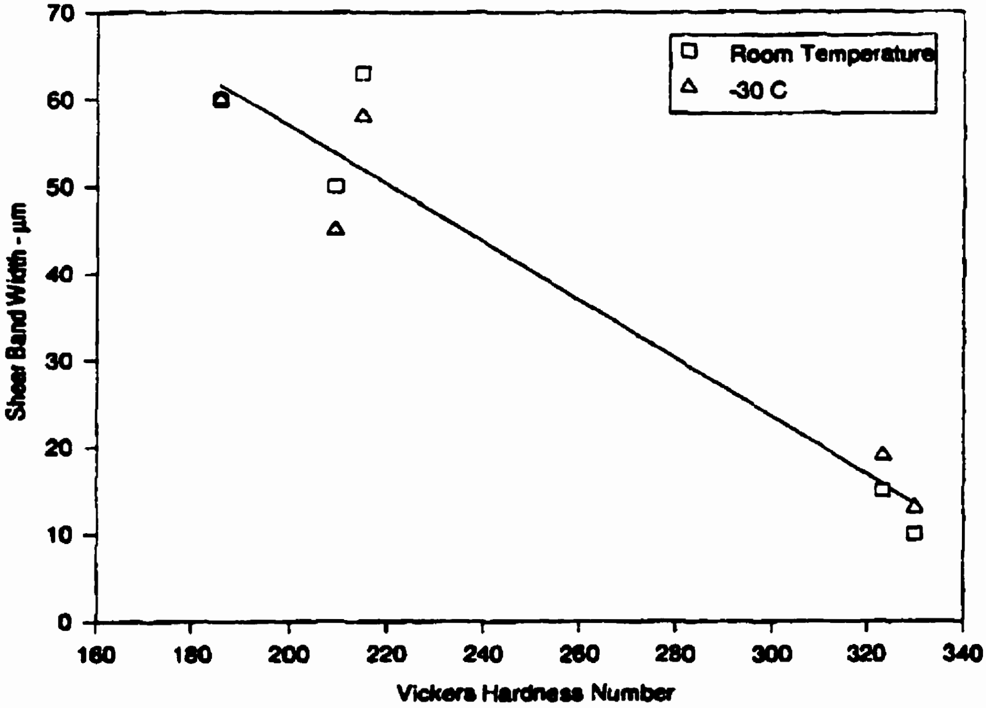

Figure 1.11: Influence of Hardness on ASB Width [53]

deformation exhibiting very high local strains that range from 5 to 100 [55, 56, 57, 58]. Some authors also reported strains of up to 570 [9]. The reported widths of the deformed adiabatic shear bands range from 10 μm to 360 μm [5, 40, 55].

There has been a lot of inconsistency in the reported results on the topic of the microstructure inside the transformed ASB. While there is no doubt that the deformed band consists of the same structure (with some recrystallisation) as the matrix material surrounding the band [59], the structure of the transformed band is still a mystery [28], although much of the work has been done in determining the nature of the so-called "white bands" [49, 50, 60, 61]. Zener and Hollomon [3] first reported that the white etched bands are untempered martensite owing to their high hardness and white appearance. The evidence for untempered martensite is somewhat divided. By the recent availability of TEM (transmission electron microscopy), X-ray and electron diffraction equipment and numerical techniques, some of the mystery has been revealed. Nevertheless, it is still not clear whether the structure is untempered martensite or not. The evidence favouring untempered martensite comes from X-ray and electron diffraction measurements, along with the fact that the material inside the band is hard and white when etched. On the other side, there is evidence that there is no untempered martensite present whatsoever [49, 50].

While the reported temperature rise within a band ranges from 450°C reported by Craig *et al.* [62], to anywhere between 500 °C and 1000 °C reported by Wittman *et al.* [63], there is no evidence of the transformation to austenite which is a precursor to martensitic transformation. According to Wittman *et al.*, the reason for white coloured etch is the absence of the carbides which are too small or have been dissolved. The calculated temperature in the band suggests that there is enough temperature for the austenitic transformation to occur. However, the duration of the high temperature needed for the transformation was not reached (the duration of the temperature rise within the band was reported to be 200 μs). The explanation that authors gave was that although there was not enough time for the transformation to occur [64], there was evidence that the time was enough for the carbon diffusion to occur, thus allowing for the martensite-like material to be formed. Similar results were reported by Mgbokwere *et al.* [65] who did not find any evidence of the phase transformation using the TEM study.

It is also often observed that deformed and transformed bands coexist together. In other words, close to the centre of the band, the transformed region is found, with the deformed part of the band existing on the edges of the transformed part of the band [63].

As mentioned earlier, the hardness of the ASB is usually higher than the hardness of the surrounding matrix material. This is true for the most of the materials except for the Titanium alloys where the hardness of the band can be either higher or lower than that of the matrix [58]. Hardness of KHN_{25} 1195 inside the band was reported [63] with the hardness of about KHN_{25} 850 outside the band in the adjacent matrix of 4340 steel (figure 1.12). The reported hardness in the band corresponds to the hardness of the quenched 4340 steel. Similar results were reported by Rogers for 1040 steel [61].

More on recent findings on microstructure inside the adiabatic shear bands can be found in references [65, 66, 67, 68].

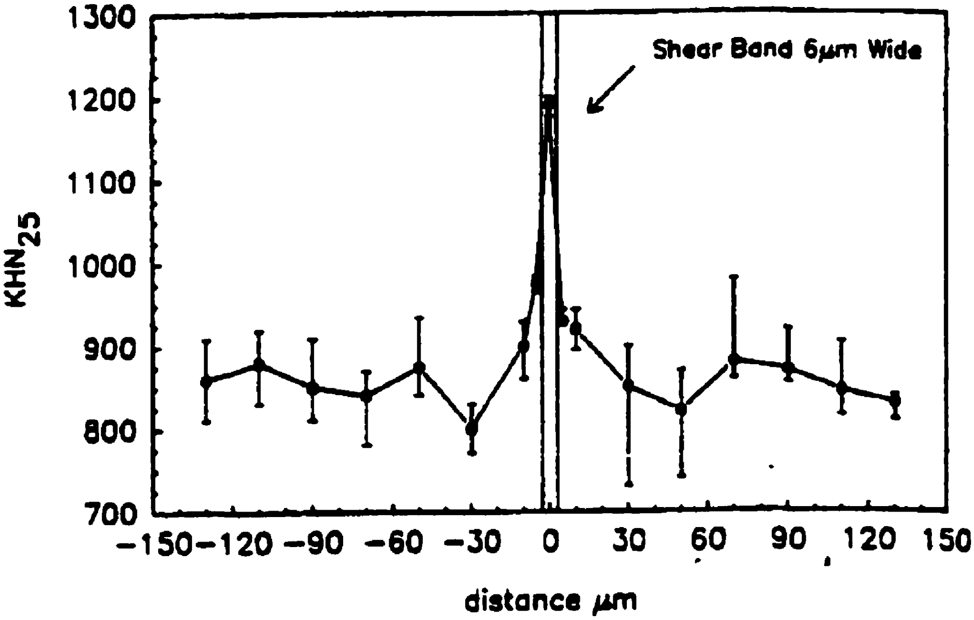

Figure 1.12: Microhardness Measured Over the Shear Band [63]

1.3.4 Formation of Adiabatic Shear Bands

The actual formation of the adiabatic shear band is a very fast process lasting anywhere between 2.5 μs and 10 μs. However, the whole process of strain localisation, stress drop and ASB formation can last for about 60 μs to 320 μs, depending on the loading conditions, material and a strain rate. Giovanola [69] performed test on 4340 steel using the torsional split Hopkinson bar (TSHB). The study of the ASB development was performed by depositing the fine grid on the outer surface of the tubular gauge section of the specimen with a distance between the lines of 100 μm. High speed photographic technique was used to capture the whole process of ASB initiation to fracture and thermocouples were used to record a temperature rise within a band. The results report that the yielding starts at 25 μs with the shear strain localisation at 42.5 μs. After this first strain localisation, 60 μm wide shear band formed in the next 5 μs. The final fracture inside the band occurred at 60 μs. Giovanola reported the temperature rise of 200 °C inside the band at the onset of the localisation, while the temperature reached 1100 °C at the fracture.

Very similar studies were performed by Marchand and Duffy [7], Hartley *et al.* [5], and Cho *et al.* [70] in order to determine the process of formation and transient behaviour of ASB. Cho, Chi and Duffy [70] performed tests on HY-100 steel using a torsional split Hopkinson bar on specimens with a deposited grid pattern. Figure 1.13 present the results from the high speed camera used in the study, and figure 1.14 presents the corresponding stress-strain curve for the same specimen with corresponding numbers for the time frames in figure 1.13. Homogeneous straining was reported to take place to about 25 % of strain after which an instability occurs and ASB forms. The ASB forms after about 160 μs (in the fifth frame in figure 1.13) and fracture occurs about 160 μs after the shear band has initiated. The reported local strains range from 600 % for 1018 CRS steel, to 2000 % for 4340 VAR steel for the strain rates of 1000 1/s with the recorded temperature rise in the range from 400 °C to 600 °C.

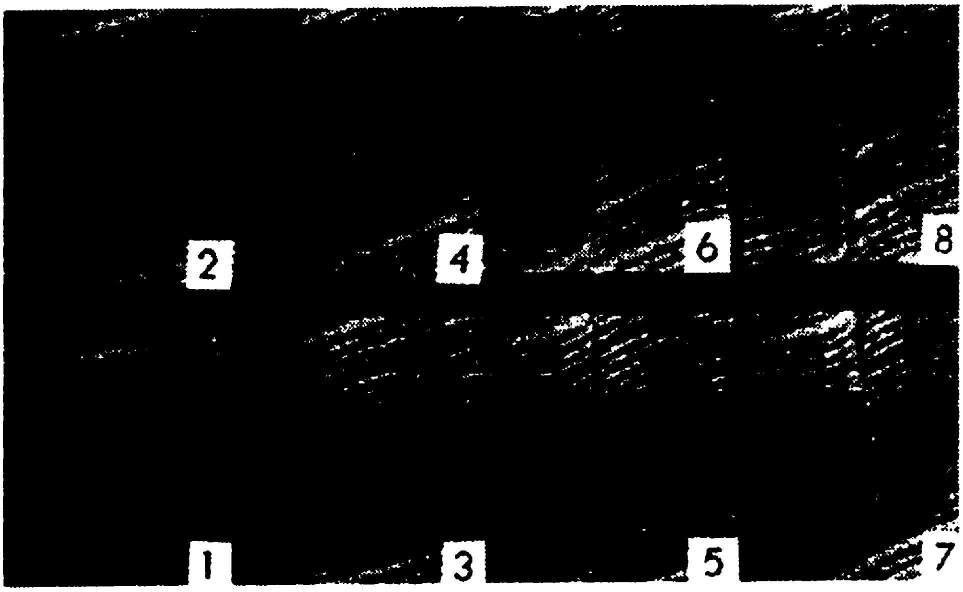

Figure 1.13: The Formation Sequence of ASB [70]

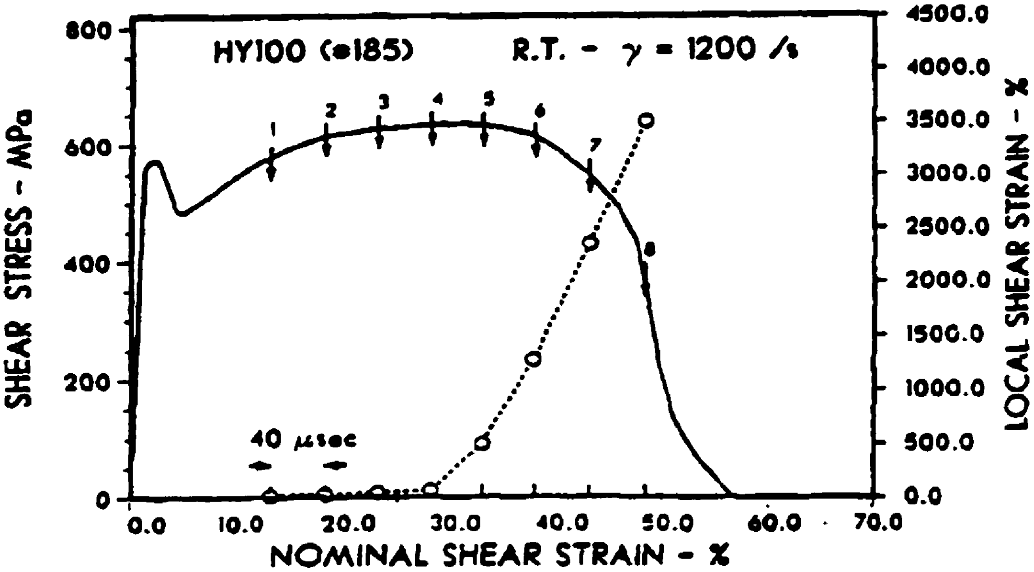

Figure 1.14: The Stress-Strain Curve Corresponding to the ASB Formation in Figure 1.4 [70]

The process of the adiabatic shear band formation is usually followed by the rapid drop in stress [28, 46, 70]. The temperature-stress-strain history reveals that the sharp drop in stress occurs when the maximum temperature within the band is reached, and that is just before the fracture occurs. Figure 1.14 shows the characteristic stress-strain curves for the specimen tested with the torsional split Hopkinson bar. After the maximum stress in the specimen is reached, there is a slight decrease in the stress with further straining, followed by the rapid drop in stress just before the fracture.

There are some results reported on the tests using the compressive split Hopkinson bar. Nakkalil, Hornaday and Bassim [46] reported very interesting feature of the ASB formation under compression on several plain carbon and low alloy eutectoid rail steels. After the yield drop (termed here as a continuous yield drop) characteristic for carbon steels when tested under low strain rate conditions, there is an abrupt drop in stress, termed as discontinuous yield drop, followed by an increase in stress (figure 1.15). This discontinuous yield drop was associated with the development of adiabatic shear band. Similar results were reported by Chung *et al.* in a computer simulation on 4340 steel under compression [71].

One interesting characteristic of adiabatic shear bands is that their occurrence depends on the loading conditions and stress state [28, 46, 59]. For example, it is known that shear bands do not occur in tensile stress state, actually, the tensile stress inhibits the formation of ASB [28]. However, the compressive stress, while inhibiting the fracture, it promotes the formation of the adiabatic shear bands. Nevertheless, not all specimen tested in compression [46] exhibited the ASB, while all the samples tested under torsional loading exhibited the adiabatic shear bands [59]. Thus, it is yet another variable for the future research to consider in order to fully understand the nature and occurrence of adiabatic shear bands.

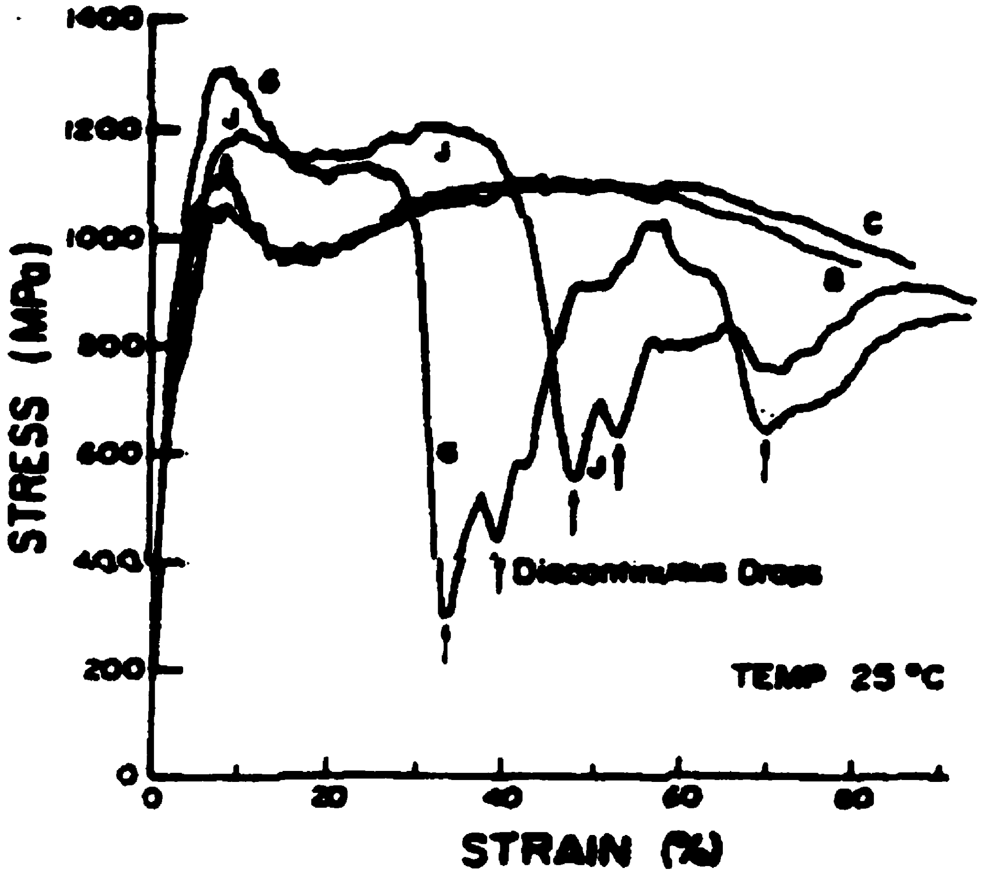

Figure 1.15: Stress-Strain Curve for the Compressive Loading With Discontinuous Yield Drop [46]

There are many instances when shear bands occur. Besides the intentionally induced deformation in the test laboratories for the sake of research, adiabatic shear bands form in metal cutting at the surface of the machined material or at the surface of the tool, in the explosive welding processes, in the rail tracks under the heavy dynamic load of the train, in the punching processes in the metal fabrication facilities, in the mining from the explosive applications, in the military from the penetration, in aviation from the dynamic loads induced by rope breaking system on the aircraft carriers, etc.

The formation of adiabatic shear bands is not limited to one per loaded material. In many instances, multiple ASBs are observed in the same sample [43, 59, 72]. While in torsion the bands are all parallel to each other and depending on the length of the gauge section there can be anywhere from 1 to more than 10 ASBs, in the plate impact experiments the bands can have a tree-like structure. The formation of the multiple bands is thought to be a consequence of heterogeneities in the material [28].

1.3.5 Fracture Inside the Adiabatic Shear Bands

As mentioned earlier, the adiabatic shear bands present a mode of failure in materials, and provided the strain rate, load and material are right, the ASB also acts as a precursor to fracture. It is observed that the initiation, growth and coalescence of microvoids is responsible for the fracture in the formed adiabatic shear band [70, 63, 73].

Irwin [73] observed the equiaxed microvoids in the transformed shear band in the U-2Mo alloy that have the appearance as though they were formed during tension (figure 1.16). These voids probably formed during the ASB formation and their coalescence led to fracture. Another interesting investigation of the cracking in adiabatic shear band was performed by Cho *et al.* [70]. They found that the microvoids nucleate at the interface of ferrite and cementite in the pearlite in 1018 CRS steel (figure 1.17). The weak ferrite phase is responsible for the excessive deformation and void nucleation leading to void coalescence and crack formation and propagation in these steels. The crack formation in HY-100 steel follows the same mechanism, the difference being that the microvoids nucleate at the MnS particles or stringers. 4340 steel tested exhibits the same fracture formation, but particles responsible for the void nucleation are the carbides.

It is clear from the experimental evidence that the mechanism for the fracture in ASB is related to void nucleation and coalescence. The variable, though, is a type of the material and the second phases or particles present. Voids can nucleate in the weaker phase due to the more excessive local deformation in that phase relative to the stronger phase as in the pearlitic steels. Also, voids can nucleate due to the stress concentration factors that raise the stress level at the interface between the stronger particle (carbide for example) and the weaker matrix as in the 4340 steels with the martensitic phase.

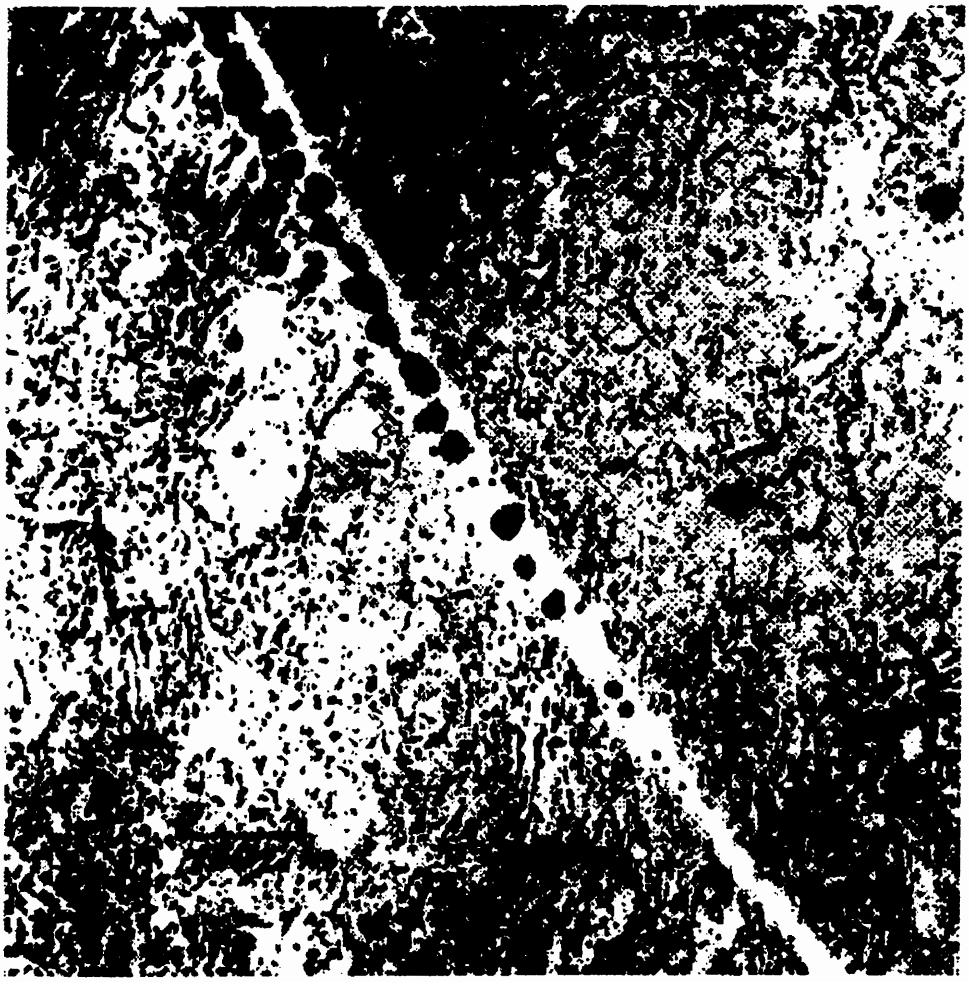

Figure 1.16: Void Coalescence in Shear Band in U-2Mo Alloy [73]

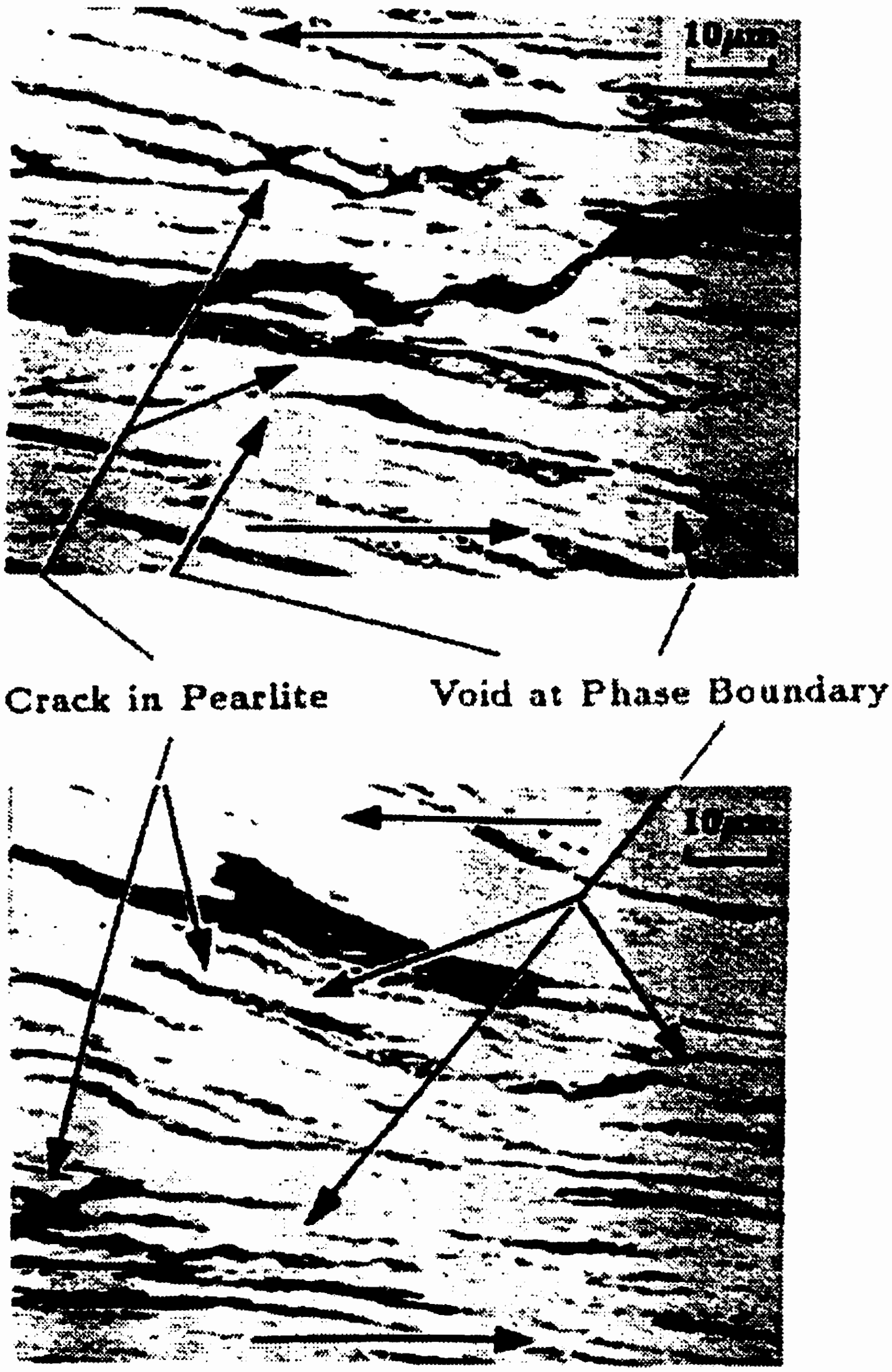

Figure 1.17: Crack and Voids in 1018 CRS Steel [70]

The formation of voids is also reported to occur in different planes parallel to each other, not always on the path of the propagating crack [28, 70, 59]. As the crack grows, it may change its plane of propagation, thus leaving behind different fracture morphology. Some experimental results show [70] the areas of larger dimples enclosed in the matrix of smaller dimples. The reason behind this is the tearing of the material between the primary and secondary planes on the crack front.

The most commonly observed fracture surface of the fractured ASB is characterised by dimples that may or may not be elongated. This is an indication of the ductile-type fracture inside the shear band. This is true whether the band is of the transformed or the deformed type. However, some authors [43, 74] reported the cleavage-type fracture in the shear band, although they were produced by the flyer plate and penetration tests. According to Bai [28], the type of the fracture that occurs within the ASB depends on when the fracture occurred. If the fracture is ductile, it means that the fracture occurred during the formation of the band, while it still hot from the arrested temperature developed due to the high plastic work. If the fracture surface appears to have cleavage characteristics, than the fracture probably happened after the band was formed and quenched by the surrounding matrix, thus the fracture happened in the hard material formed due to the phase transformation.

There are normally four distinct regions that may be present on the fracture surface in the adiabatic shear bands. These include the ductile dimples, cleavage, smoothed surface (present in the torsional tests) and knobbly structure. Smoothed surface probably occurs due to the rubbing of the two broken parts of the specimen. The most interesting feature is the knobbly structure (figure 1.18). It represents the melting of the peaks of ductile dimples on the fracture surface which can mean that the temperature inside the band reaches that of the melting temperature of the material. However, the melted peaks can also be a consequence of the two surfaces rubbing against each other producing the frictional temperature rise after the fracture.

Figure 1.18: Knobbly Structure on the Fracture Surface of ASB [75]

1.4 HIGH STRAIN RATE EXPERIMENTAL TECHNIQUES

1.4.1 Introduction

The material response to loading depends on the strain rate that is applied. As mentioned earlier, the behaviour of the material is much different at high rates of strain than at lower rates of strain. In recent years, much of the attention is placed on the material response at high strain rates. This interest comes with the developments in industry such as nuclear, space, military, etc., that need more understanding of the material behaviour at high rates of strain in order to facilitate further research in industry and to be able to properly select and apply the materials.

According to the strain rate applied, the division of the experimental techniques was made. The whole spectrum of the available strain rates in the research field is summarised below [76].

10^{-6} to 10^{-5} s^{-1}	This range of strain rates represents the creep, and tests are usually performed at high temperatures. Occurrence of these rates is found in turbines.
10^{-4} to 10^{-2} s^{-1}	These rates correspond to static and quasi-static loading conditions. These include the conventional tensile and compression tests. As in the above range of strains, the results obtained for the stress-strain behaviour of the material in this range can be used to describe the behaviour only in these strain rate ranges, since the material behaviour changes when the strain rate is changed.

10^{-2} to 10^{-1} s^{-1}	This is an intermediate strain rate range where the inertia effects first become important.
10^{2} to 10^{4} s^{-1}	High strain rate range where inertia effects and other high strain rate phenomena start to influence the material response. Split Hopkinson bar (SHB) tests fall in this range. Test include tension, compression, shear and torsion performed on the SHB.
10^{4} to 10^{6} s^{-1}	Flyer plate experiments fall in this category. In this high strain rate range, it is important to consider thermodynamic response of the material.

Figure 1.19 summarises the above spectrum of strain rates with the experimental applications.

1.4.2 Split Hopkinson Bar

There are different arrangements for the split Hopkinson bar. It can be used to perform tests in compression, tension, shear, torsion and direct impact in the strain rate range of 10^{2} to 10^{5} s^{-1}.

1.4.2.1 Compressive Split Hopkinson Bar

Compressive SHB is used to test specimens in compression at strain rates of 10^{2} to 2×10^{3} s^{-1}. The equipment consists of two bars; incident bar and transmitter bar, plus the striker bar (short in length) which is fired from the gun barrel and hits the incident bar. The specimen is cylindrical and is placed between the incident and transmitter bars. When the striker bar hits the incident bar, the incident pulse is generated that travels at

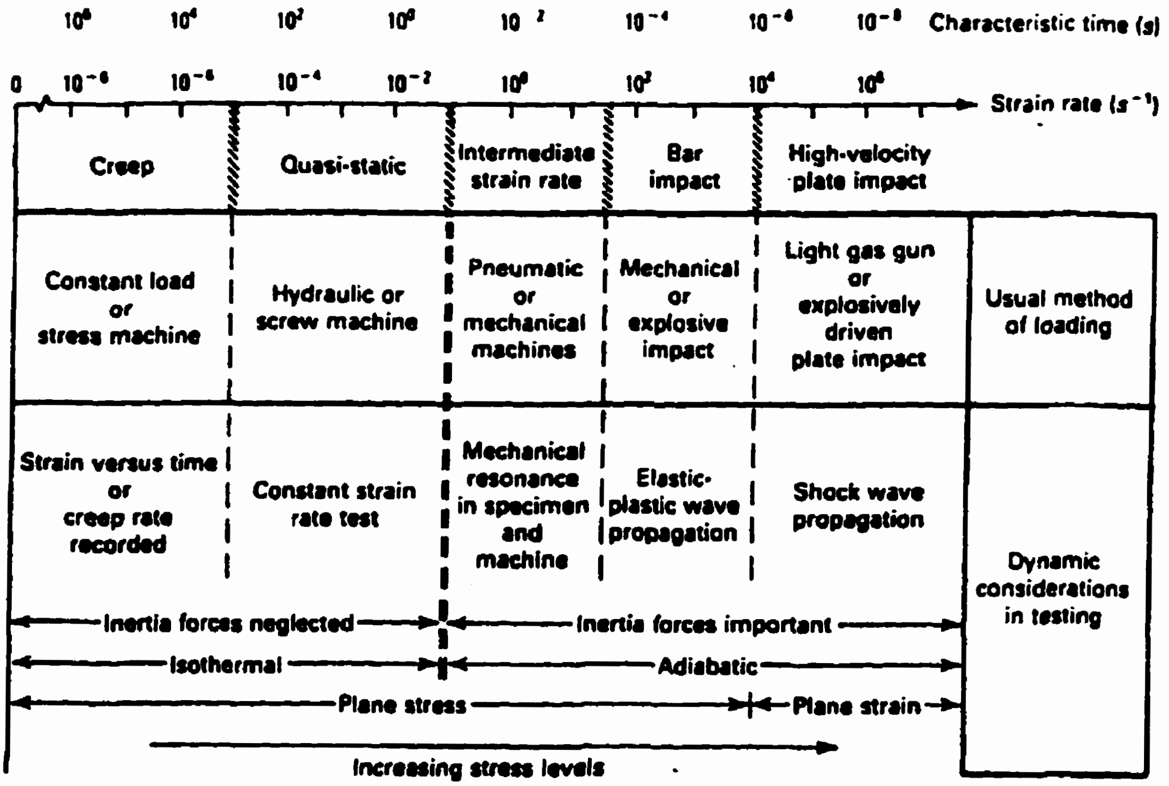

Figure 1.19: Dynamic Aspects of Mechanical Testing [1]

speed $c = \sqrt{E/\rho}$ towards the specimen. The part of the incident pulse is transmitted to the transmitter bar through the specimen, and part is reflected from the specimen back to the incident bar due to acoustical impedance and difference in the cross-sectional areas of the specimen and the transmitter bar. By recording the strain-time history in the incident and transmitter bars, it is possible to obtain data on stress and strain.

Since the specimen is small, 15.8 mm in diameter and 6.8 mm in length in the study performed by Yokoyama [77], the stress state can be considered uniform since many reflections take place in the specimen. Besides this assumption of the uniform stress, some other assumptions have to be realised in order to obtain the satisfactory data. First, it is assumed that the waves propagate through the bars undistorted at the elastic wave velocity. Second, the pressure bars have to be long enough to allow for the observation of the entire loading event, without the interruptions caused by wave reflections. One version of the compressive SHB with the data acquisition equipment is presented in figure 1.20.

There are some disadvantages and limitations of the compressive SHB. At higher strain rates, some of the major assumptions seize to be valid, including the wave propagation effects, radial inertial effects and barrelling. Barrelling is indicator that there is no uniform state of stress present which was the main assumption. These considerations have limited the use of the compressive SHB to strain rates of up to 2×10^3 s^{-1}.

1.4.2.2 Tensile Split Hopkinson Bar

Tensile SHB set-up is very similar to the compressive SHB. The difference is in the specimen mount. Specimen is made with threads at each end and is screwed in the collars at the ends of incident and transmitter bars. The practical limit for strain rate is

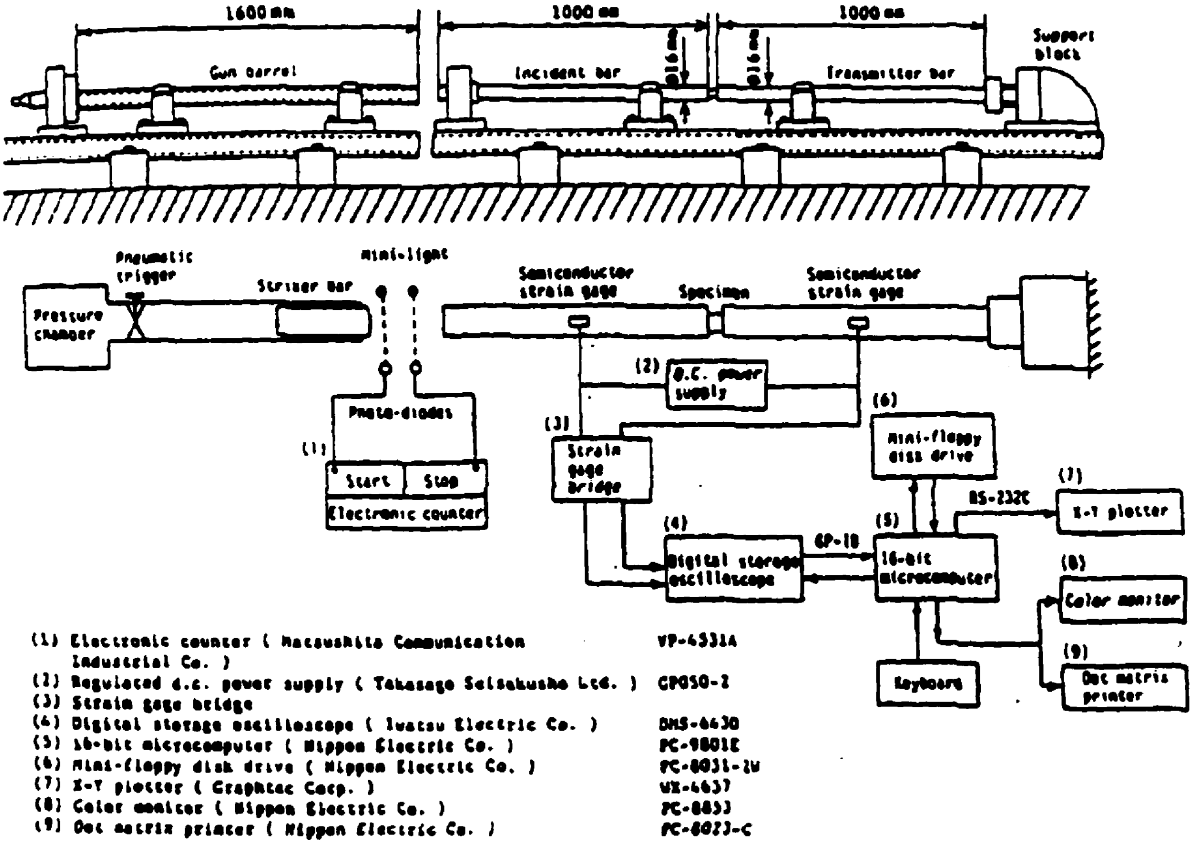

(1)	Electronic counter (Matsushita Communication Industrial Co.)	VP-4531A
(2)	Regulated d.c. power supply (Takasago Seisakusho Ltd.)	GP050-2
(3)	Strain gage bridge	
(4)	Digital storage oscilloscope (Iwatsu Electric Co.)	DMS-6430
(5)	16-bit microcomputer (Nippon Electric Co.)	PC-9801E
(6)	Mini-floppy disk drive (Nippon Electric Co.)	PC-8031-2W
(7)	X-Y plotter (Graphtec Corp.)	WX-4637
(8)	Color monitor (Nippon Electric Co.)	PC-8853
(9)	Dot matrix printer (Nippon Electric Co.)	PC-8023-C

Figure 1.20: Set-up of Compressive SHB [76]

10^3 s^{-1} due to the longer time rise of the incident pulse. Wave reflections and interactions also start to interfere with the data at higher strain rates.

1.4.2.3 Torsional Split Hopkinson Bar

Torsional SHB enables testing tubular specimens in torsion. With the development of this equipment, higher strain rates were achieved with the higher available strains. The equipment consists of two bars; incident and transmitter bar, and the tubular specimen between the bars. Loading is achieved by storing the torque in the portion of the incident bar by means of some kind of clamp, depending on the specific set-up. When the torque is released, the short pulse is generated and travels towards the specimen. As in the compressive and tensile SHBs, part of the pulse is transmitted and part is reflected. By recording the strain-time history, the data on stress, strain and strain rate can be obtained.

There are advantages of the torsional SHB over the tensile and especially compressive SHB. The higher strain rates can be obtained (up to 10^4 s^{-1}) , and there is no effect of barrelling found in compressive SHB. More on torsional split Hopkinson bar is be presented in Chapter 2.

1.4.2.4 Direct Impact Split Hopkinson Bar

This version of the split Hopkinson bar was developed in order to achieve even higher strain rates. Strain rates achieved with this set-up are up to 10^5 s^{-1}. Here, the specimen is impacted directly and the incident bar is eliminated.

1.4.3 Flyer Plate Experiment

The flyer plate experiments offer the highest achievable strain rate in testing. Strain rates of 10^6 to 10^7 s^{-1} can be achieved by the impact of two plates. The advantage of these experiments, beside the highest strain rate, is the absence of two components of strain, thus there is only uniaxial strain present. However, the stress state cannot be assumed to be uniaxial as in the SHB tests, and all three components of stress have to be considered. Moreover, the plate design allows for higher stress amplitudes accompanied by higher strain rates. The analysis of the stress and strain is performed by considering the uniaxial strain distribution, and the stress triaxiality problem is eliminated.

1.4.4 Expanding Ring Technique

This experiment employs a specimen in the shape of the ring that is either explosively or, more recently, electromagneticaly expanded. The advantage of this experiment is the uniformity of the stress and ease of measuring variables. The difficulty with this experiment is that it is not easy to do the actual tests. Moreover, the data at higher strain rates begin to deviate and the practical strain rate is limited by problems such as radial inertial effects, wave propagation effects and strain and stress state in the specimen among others.

1.4.5 Numerical Techniques and Simulations

More recently, with the development of computer codes and other simulation programs, the study of the high strain rate effects on materials has been done by computer simulations. The advantage of this technique is that the material and other variables can be easily changed and results for different conditions can be obtained. Studies were done on materials with variables such as thermal conductivity, hardness, plasticity, etc. By simply changing some or all of the variables, different material is created and can be tested without the difficulty of manually preparing specimens for the actual experimental examination. The disadvantage, however, is that usually results obtained by computer simulations have to be verified by the experimental results in order to become valid.

CHAPTER 2 DESIGN OF EXPERIMENT AND EXPERIMENTAL PROCEDURE

2.1 INTRODUCTION

The experiment was performed on the torsional split Hopkinson bar using the tubular-shaped specimens. The strain rates achieved with this equipment ranged from about 250 s^{-1} to 850 s^{-1}. This chapter presents the equipment description and experimental procedure along with the specimen properties.

2.2 TORSIONAL SPLIT HOPKINSON BAR

2.2.1 Historical Development

The split Hopkinson bar was developed as an improved version of the Hopkinson bar which was first developed and used by British engineer John Hopkinson in 1914. Hopkinson realised that displacements in the bar were directly related to the stresses in the bar and that length of the wave in the bar was related to duration of impact through the velocity of the sound in the bar. This first version of the bar utilised only one bar which was struck by bullet or detonation of explosive.

Kolsky [78] modified the original version of the Hopkinson bar in 1949, and he developed the split Hopkinson bar that utilises two bars instead of one. Specimen was placed between the bars (transmitter bar and incident bar), and by sending the compression wave through the incident bar towards the specimen, one part of the wave was transmitted through the specimen and the other part was reflected back from the specimen. The values for axial stress were thus obtained from the transmitted wave, and values for the strain rate were obtained from the magnitude of the reflected wave.

The first torsional split Hopkinson bar was developed by Baker and Yew in 1966 [79]. They used the same idea as in the original SHB but they applied a torsional step wave. The torque was stored in a portion of the incident bar and than released, providing the step torsional pulse that was loading the specimen placed between the bars. Again, the analysis of the stress and strain was obtained from the reflected and transmitted pulses on each side of the specimen.

Since the torsional SHB was developed in 1966, much of the advancement has taken place in the design of the bar. Today, many facilities exist that use the split Hopkinson bar for the high strain rate testing in the range of 10^2 to 10^4 s^{-1}. One such instrumentation exists at the University of Manitoba where the study on high strain rate behaviour of materials has been progressing for many years. The torsional version of the bar was developed at the University of Manitoba in 1995 by C. D. Liu, E. Cepus and M. N. Bassim.

2.2.2 Design and Implementation of the TSHB

In this study, the stored torque torsional split Hopkinson bar was used. The standard set-up is shown in figure 2.1 and the wave diagram for three pulses (incident, reflected and transmitted pulses) is presented in figure 2.2. The version developed by C. D. Liu, E. Cepus and M. N. Bassim used in this study is presented in figure 2.3.

The TSHB consists of two bars; incident and transmitter bar (figure 2.1 and 2.3). Bars are 25.4 mm in diameter made of 6061-T6 Aluminum alloy and are supported by Teflon bearings along the length. The loading pulse is produced by releasing the torque that is stored by the means of the clamp. Clamping must be adequate so that no slipping occurs during torque-storing, and upon release of the torque it must release the torque fast enough so that sharp step wave is generated.

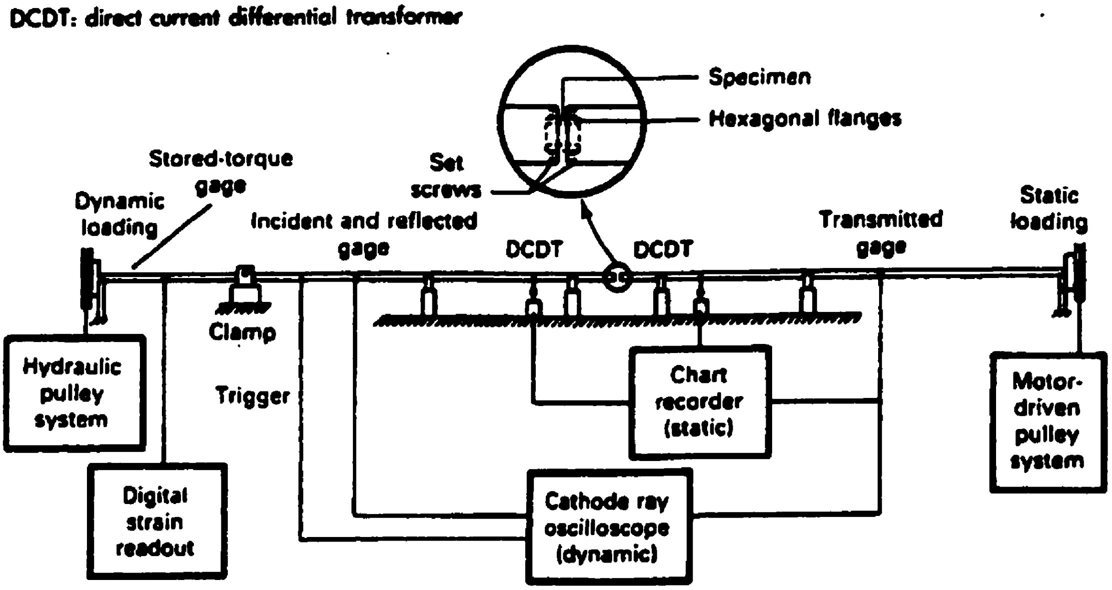

Figure 2.1: Standard Set-up of the Torsional Split Hopkinson Bar [80]

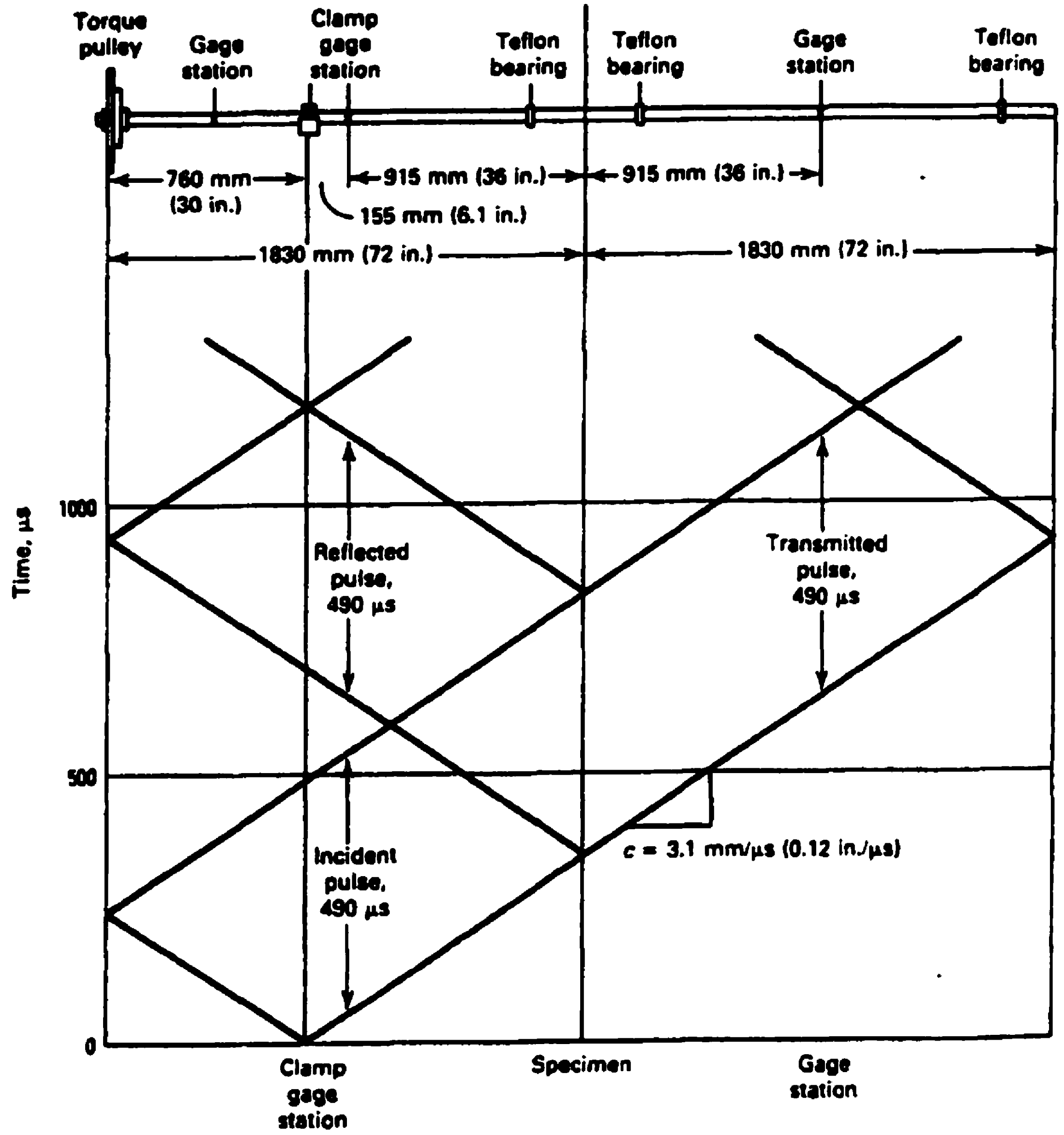

Figure 2.2: Wave Characteristic Diagram For the Stored-Torque Kolsky Bar [80]

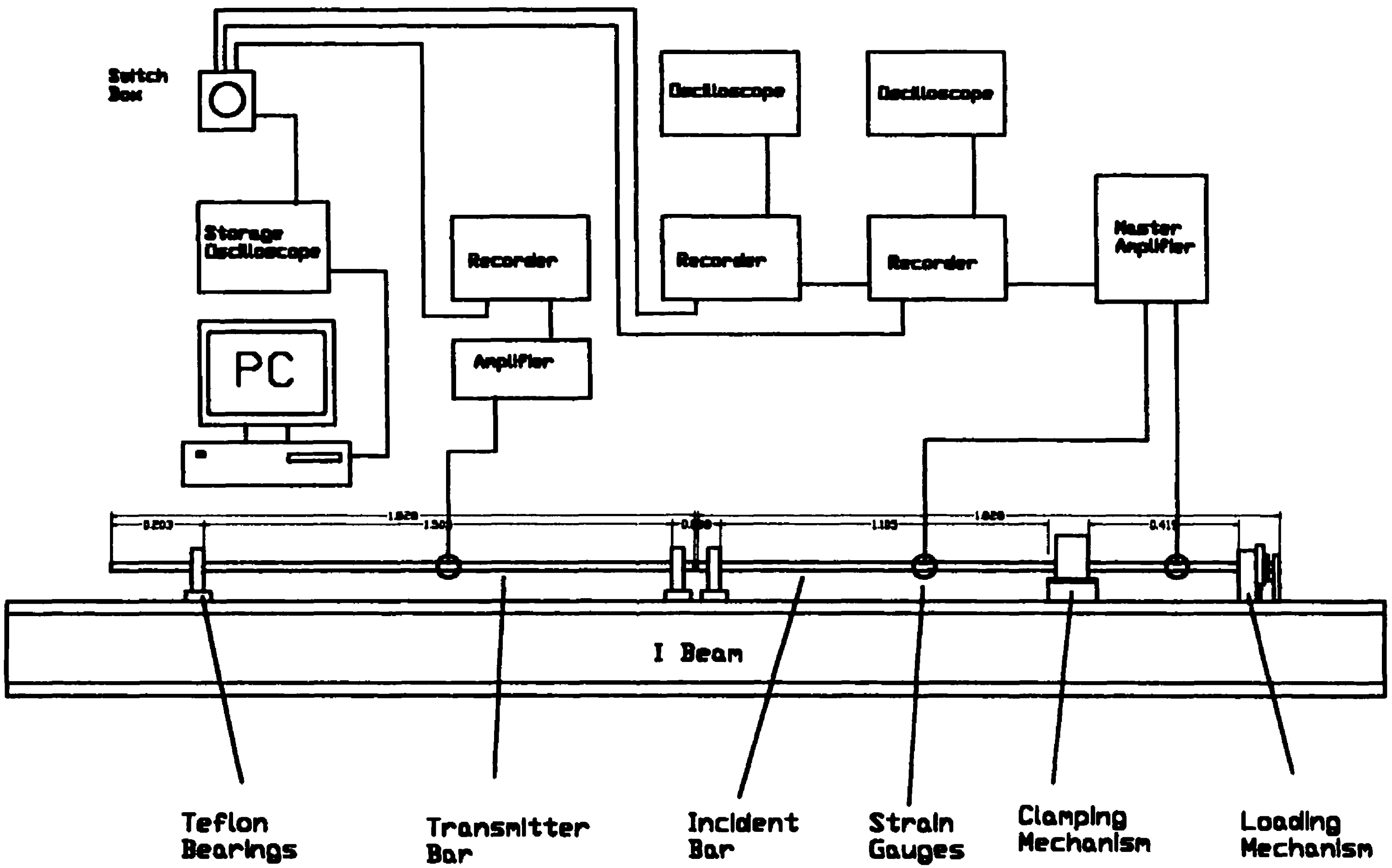

dimensions are in metres

Figure 2.3: Torsional SHB With Equipment Used in This Study

When the torque is released, the loading pulse (the incident wave) travels towards the specimen. The unloading pulse is also generated and travels in the opposite direction, from the clamp towards the loading mechanism (figure 2.2). When the incident wave (the loading pulse) reaches the specimen, one part is transmitted through the specimen, and the other part is reflected back. The incident pulse, reflected pulse and transmitted pulse are recorded with the digital wave recorder through the strain gauges placed on the bars. The strain gauge on the incident bar captures both the incident and reflected waves. The transmitted pulse is captured by the strain gauge on the transmitter bar. Strain gauges are placed at certain distances from the specimen to avoid the interference of the incident and reflected pulses. More on the actual design of the TSHB can be found in [53] and [80].

There are some advantages of the torsional split Hopkinson bar over the axial split Hopkinson bars. The compressive pulse in axial loading is accompanied by the Poisson's ratio effect and this produces the radial expansion of the specimen which presents the violation of the assumption made in axial testing. Under higher strain rates, the radial expansion is opposed by the inertia effects and the results obtained from the tests are not valid because of geometric dispersion. Due to the torsional loading in the tests performed on TSHB, the radial component of the stress is not present due to the absence of Poisson's ratio.

Another advantage of the TSHB is the absence of the wave dispersion. In compressive SHB, the pulse that is generated is dispersed because the different frequency components of the pulse travel at different velocities. Higher frequencies travel at lower velocities. In the torsional pulse, all frequency components travel at the same velocity and there is no wave dispersion. However, the disadvantage of the non-dispersive pulse is that if the pulse is noisy (high frequency components superimposed on the main pulse) when initiated, the noise will travel along with the main pulse causing non-constant strain rate. This does not happen in the compressive SHB since higher frequencies attenuate due to the wave dispersion.

The main disadvantage of the torsional SHB is the higher cost of specimen preparation. Specimens for the TSHB are of tubular shape and are more difficult to machine than the cylindrical specimens for the axial SHB. Another problem is the mounting or gripping of the specimen. If specimen is placed in the hexagonal slots at the end of the two bars, care must be exercised to obtain a good grip, so that there are no unwanted reflections off the specimen..

To obtain the values for the stress and strain in the specimen, the strains in the incident and transmitter bars are recorded through the strain gauges. The reflected pulse gives the value of the strain rate in the specimen . By integration of the strain rate, the shear strain in the specimen can be obtained. The shear strain in the specimen is obtained by taking the difference in rotation of its two ends and dividing the difference by the specimen gauge length

$$\gamma_s = \frac{D_s \phi_1 - D_s \phi_2}{2L_s} \tag{2.1}$$

where D_s is a mean diameter of the specimen, ϕ_1 is angle of twist of the incident bar, ϕ_2 is the angle of twist of the transmitter bar, and L_s is a gauge length of the specimen.

The angle of twist of the transmitter bar ϕ_2 can be obtained from the measured strain in the transmitter bar

$$\gamma_T = \frac{D}{2}\frac{\partial \phi_2}{\partial x} = \frac{D}{2c}\frac{\partial \phi_2}{\partial t} \tag{2.2}$$

where D is diameter of the bar, and $c = \sqrt{G/\rho}$ is the velocity of the torsional wave (G is modulus of rigidity, ρ is density). From equation (2.2)

$$\phi_2 = \frac{2c}{D} \int_0^t \gamma_T(t)\, dt \tag{2.3}$$

The angle of twist in the incident bar is determined from the difference between incident and reflected pulses

$$\phi_1 = \frac{2c}{D} \int_0^t [\gamma_I(t) - \gamma_R(t)]\, dt \tag{2.4}$$

From equations (2.1), (2.3) and (2.4), the strain rate in the specimen is obtained

$$\dot{\gamma}_s(t) = \frac{c}{L_s} \frac{D_s}{D} [\gamma_T(t) - [\gamma_I(t) - \gamma_R(t)]] \tag{2.5}$$

Equation (2.5) can be simplified for the case of homogeneous strain when $\gamma_T \doteq \gamma_I - (-\gamma_R)$ and the strain rate becomes

$$\dot{\gamma}_s(t) = \frac{2cD_s}{L_s D} \gamma_R(t) \tag{2.6}$$

From the recorded history of strain in the incident bar from the reflected pulse, the strain rate in the specimen is obtained from equation (2.6). The strain in the specimen is obtained by numerical integration of equation (2.6). Therefore, by recording the reflected wave in the incident bar, strain rate and strain in the specimen are obtained.

Transmitted pulse provides the measure for the shear stress in the specimen. The shear stress in the tubular specimen is given by

$$\tau_s = \frac{2T_s}{(D_s^2 \pi) t_s} \tag{2.7}$$

where t_s stands for specimen wall thickness and T_s for torque in the specimen. The torque in the specimen is given by the average of the torques at each end, T_1 at the interface with incident bar, and T_2 at the interface with transmitter bar

$$T_s = \frac{T_1 + T_2}{2} \tag{2.8}$$

The torque T_1 can be found from the strains of the incident and reflected waves

$$T_1 = \frac{D^3 \pi}{16} G(\gamma_I + \gamma_R) \tag{2.9}$$

Again, for the homogeneous state of stress in the specimen, $\gamma_T = \gamma_I + \gamma_R$, and the stress in the specimen is obtained

$$\tau_s(t) = \frac{G D^3}{8} \frac{\gamma_T(t)}{D_s^2 t_s} \tag{2.10}$$

More information on the torsional split Hopkinson bar and its design can be found in reference [53].

2.3 DESIGN OF SPECIMENS

This section describes the type of specimens used in this study. Material, geometry and heat treatment with corresponding microstructure are explained. Attention is also placed on the specimen preparation since it is of great importance that specimens be machined properly with the fewest defects.

2.3.1 Material for Specimens

This study was performed on AISI 4140 steel received as hexagonal bar in cold drawn and partially annealed condition. The composition of the steel is presented in Table 2.1 along with some thermophysical data. It is seen that the values of thermal conductivity and thermal diffusivity are relatively low which explains the susceptibility of this material to adiabatic shear band formation.

2.3.2 Specimen Geometries

Three different variations on the basic geometry of the specimen were utilised in this study. The basic specimen shape with dimensions is presented in figure 2.4. The gauge section of the specimen is tubular in shape with the outer diameter 13.36 mm and wall thickness of 0.4 mm. Ends of the specimen are hexagonal and fit into the slots at the ends of the bars which are the same size hexagonal groves.

Three different gauge lengths machined for this study are 3.00 mm, 3.78 mm and 10 mm. Different gauge lengths were made in order to obtain different strain rates and this will be discussed in more detail in the section on experimental results. All other geometrical properties of the specimen remained the same for each sample.

Table 2.1: Properties of AISI 4140 Steel [81, 82]

C	Mn	P (max.)	S (max.)	Si	Cr	Mo
0.38-0.43	0.75-1.0	0.03	0.04	0.25-0.4	0.8-1.1	0.15-0.25

- Thermal Conductivity $k = 41$ W/m K
- Thermal Diffusivity $\alpha = 11.2 \text{ x}10^{-6}$ m^2/s
- Density $\rho = 8100$ kg/m^3
- Specific Heat $c_p = 435$ J/kg K

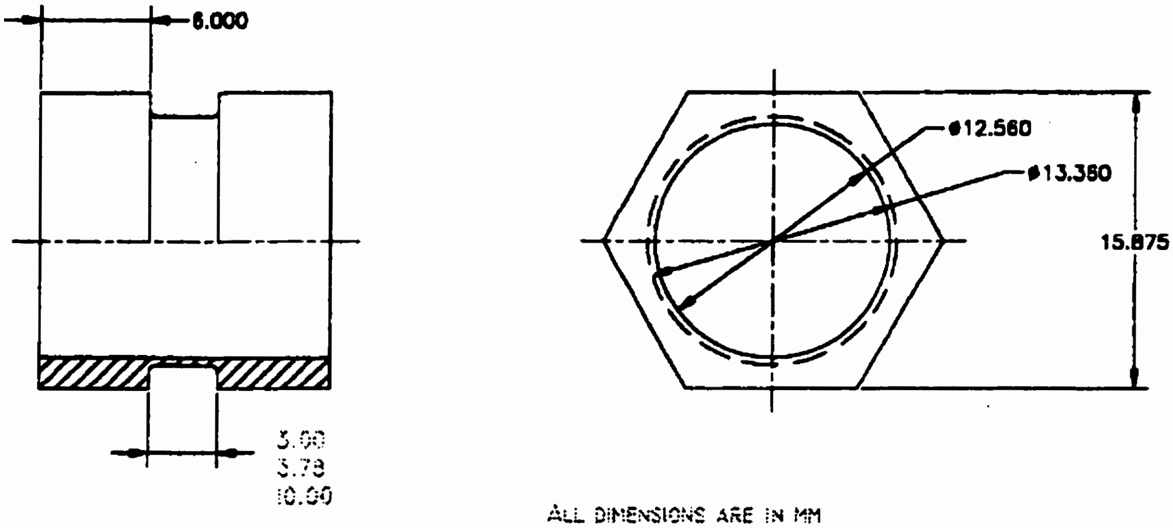

ALL DIMENSIONS ARE IN MM

Figure 2.4: Specimen Geometry and Dimensions

2.3.3 Specimen Preparations

This section is included, because for the valid experimental data, it is crucial to have properly prepared specimens. This includes the exercised care in machining. According to Molinari and Clifton [83] the geometrical variation influences the material response. They defined the defect parameter , ε, that is related to variations in the wall thickness. It was concluded that the larger the variation in the wall thickness, therefore the greater ε , the earlier is the yield drop and fracture with smaller maximum strains. According to this, special care has to be taken in order to have the same ε for all specimens if the results are to be compared. It was also concluded that the circumferential variation in geometry does not influence the behaviour considerably.

The hexagonal bar was first cut in length approximately 15 centimetres for easier handling. First, the hole was drilled with the centring drill to ensure the proper centring of the internal diameter. Cooling fluid was used to take away the chips and heat that was generated during machining.

Next, the hole was drilled with 31/64 in. drill to about 2.5 cm depth. The final dimension of the hole was then achieved by reaming with 12.7 mm reamer. The reamer was carefully chosen in order to obtain the best possible finish of the internal dimension. While reaming, instead of the cooling fluid, the cutting grease was used, since it provides better surface finish.

The next step was to machine the gauge section of the specimen. Here is where extra care was taken to ensure the consistency among specimens. Three different gauge lengths were machined for this study. Group 1 of specimens with 3.00 mm gauge length, group 2 with 3.78 mm gauge length and group 3 with 10 mm gauge length. 3.00 and 3.78 mm gauge lengths were cut using specially designed cutting tool that cuts notches of 3.00 mm and 3.78 mm respectively. The notch was cut to diameter of 13.46 mm to ensure that after sanding and polishing, the outer diameter is 13.36 mm. Again, while machining these notches, the cutting grease was used to obtain satisfactory surface finish. Before machining the gauge section, the cutting tool had to be squared in order to satisfy for the minimal geometrical defect parameter ε defined by Molinari and Clifton. The measurement of the depth of the feed was observed on the digital displacement meter installed on the lathe. Further to this measurement, frequent measurements with digital calliper were performed to ensure the dimension is met.

Specimens with the gauge length of 10 mm were cut in the similar fashion. Since the gauge length is long, it was not possible to machine it with 10 mm cutting tool because of vibrations produced due to high contact area between the tool and the material. Here, two notches 3 mm wide were cut first and than, the 10 mm wide cutting tool was used to take off the rest of the material.

When gauge sections were machined, the specimen was separated from the bulk material with the parting tool while still in the lathe.

After the separation, specimen was polished in the lathe. Sanding was first performed with sand papers from coarser to finer, the fines one being 600 (or 1200P) grit size. After each change of the sand paper, specimen was cleaned in the ultrasonic bath to ensure that contamination with larger particles does not happen. After sanding was done, the gauge section was polished with the diamond paste from $6\,\mu$ to $1\,u$. Polishing with 1 u diamond paste was done after specimens were heat treated because of the scale that grows on the metal during the heat treatment.

The final cleanup of the specimens was performed in the ultrasonic alcohol bath to clean all the remaining particles and grease.

2.3.4 Specimen Heat Treatment

Since the material was received in cold drawn and partially annealed condition, specimens were heat treated to achieve the desired microstructures. There are four groups of specimens (A, B, C and D) according to heat treatment and produced microstructure, and that is presented in table 2.2. Annealing was done at 850 °C for 1 hour followed by quenching in oil or air cooling. After quenching the specimens were tempered at different temperatures in order to obtain different microstructures. Hardness produced by heat treatment is different for each group of specimens (A, B, C and D) and is presented in table 2.3.

Heat treatment was performed in the inclined Marshall furnace in the presence of inert Argon gas in order to reduce the oxidation and scale formation. Nevertheless, some of the scale occurred and specimens were finally polished to remove the oxide film with 1 u diamond paste.

It is beneficial to emphasise here that there are three groups of specimens according to the gauge length and strain rate (group 1, group 2 and group 3), and there are four groups of specimens according to the heat treatment and microstructure (group A, group B, group C and group D). For the convenience, this classification is presented in the tabular form (table 2.4). Therefore, each group of strain rate (1, 2 or 3), has all four groups of heat treatment (A, B, C and D).

Table 2.2: Specimen Heat Treatment

Designation	Specimen Heat Treatment
A	As received. No heat treatment was performed
B	Specimen was heated at 850 °C for 1 hour and air cooled.
C	Specimen was heated at 850 °C for 1 hour and oil quenched, followed by tempering at 315 °C for 1 hour and air cooled.
D	Specimen was heated at 850 °C for 1 hour and oil quenched, followed by tempering at 480 °C for 1 hour and air cooled.

Table 2.3: Specimen Hardness

Group	A	B	C	D
Hardness (VHN)	250	207	292	352

Table 2.4: Classification of Specimens

According to Strain Rate	According to Heat Treatment			
Group 1	A	B	C	D
Group 2	A	B	C	D
Group 3	A	B	C	D

2.3.5 Pre-Test Specimen Microstructures

As mentioned earlier, there are four groups of specimens according to the heat treatment. These are A, B, C and D. The heat treatment performed on specimens is presented in table 2.2 and is discussed in the previous section. The resulting microstructures are explained in this section.

Sample A is in as received condition. The optical micrograph of specimen A is presented in figure 2.5. It is seen that the structure consists of ferrite (white) and pearlite (dark) phases. The pearlite phase is very fine consisting of fine lamellae of cementite and ferrite. The grains are somewhat elongated due to the cold rolling. As mentioned earlier, it seems that only partial annealing was performed which is explained by the elongated structure.

Sample B is presented in figure 2.6 and it is observed that the microstructure consists also of ferrite and pearlite phases. In this case, the grains are equiaxed because of the annealing that was performed at 850 °C. By observing the micrograph, one can also see that the pearlite phase is coarser than in sample A. This is due to the longer total annealing time for sample B than for sample A that was annealed by the supplier.

The hardness of the sample A is higher than hardness of the sample B (table 2.3) due to the finer pearlite phase present in A, as well as due to the remainder of the strain hardening effect produced during rolling. Partial annealing of specimen A did not produce essential recovery of the residual strain and recrystallisation for the uniform and strain free microstructure. The result is a present strain field that hinders the dislocation motion and increases hardness, along with the effect of finer phase that is more resistant to plastic deformation due to the greater interphase/interface area between phases that serves as the dislocation motion barrier.

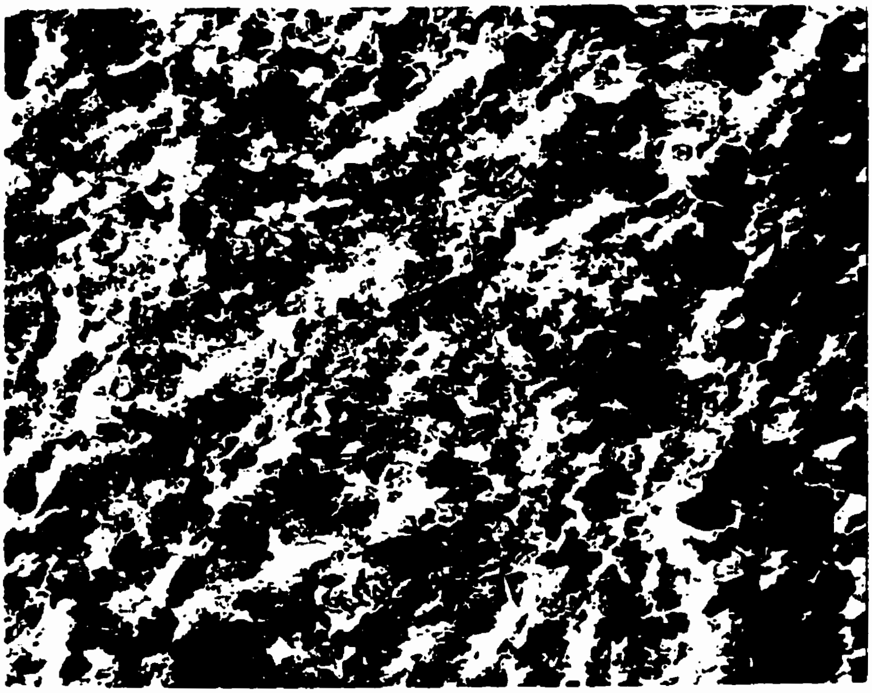

Figure 2.5: Sample A Pre-Test Optical Micrograph

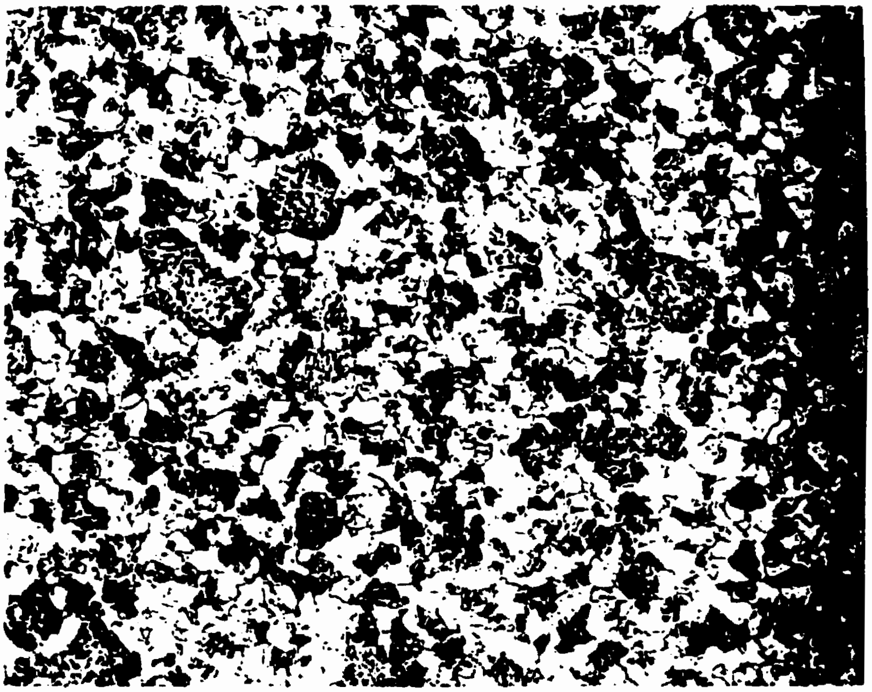

Figure 2.6: Sample B Pre-Test Optical Micrograph

Figure 2.7 shows the microstructure of sample C. This specimen was quenched and tempered at 315 °C. The microstructure shows tempered martensite consisting of martensite and very fine dispersed cementite particles inside the ferrite matrix. After quenching, since diffusion did not occur, all of the carbon remained in the BCT (body centred tetragonal) distorted lattice single phase (martensite). After tempering was performed, the diffusion was allowed to occur, and carbon started diffusing forming the cementite (Fe_3C) phase out of martensite, leaving the ferrite matrix with finely dispersed cementite. The dark boundaries in the micrograph are believed to be the prior austenite grain boundaries occupied by the precipitated carbides during tempering.

Sample D pre-test optical micrograph is presented in figure 2.8. The structure is also tempered martensite (martensite-ferrite-carbide aggregate) as sample C, but tempering was performed at higher temperature. The structure shows mixture of cementite phase (dark) dispersed in the ferrite (white) matrix, and martensite (light). Prior austenite grain boundaries are absent in this micrograph, and the cementite phase is coarser and more uniformly dispersed than in the sample C micrograph.

One would probably expect the hardness of the sample C to be higher than for the sample D because of the higher tempering temperature for sample D. This is, however, not the case, probably due to the more uniform distribution of the cementite phase within the ferrite matrix in sample D. Also, the cementite phase in sample C seemed to have just started to segregate, which is explained by the dominance of the white ferrite phase in the micrograph (figure 2.7). The consequence is the lower hardness of sample C due to the dominant softer ferrite phase.

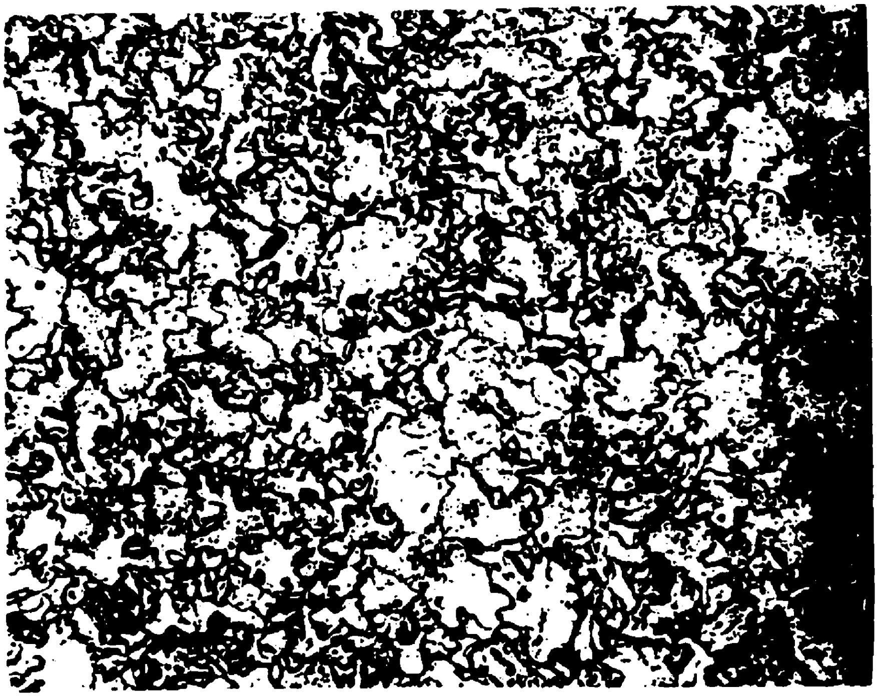

Figure 2.7: Sample C Pre-Test Optical Micrograph

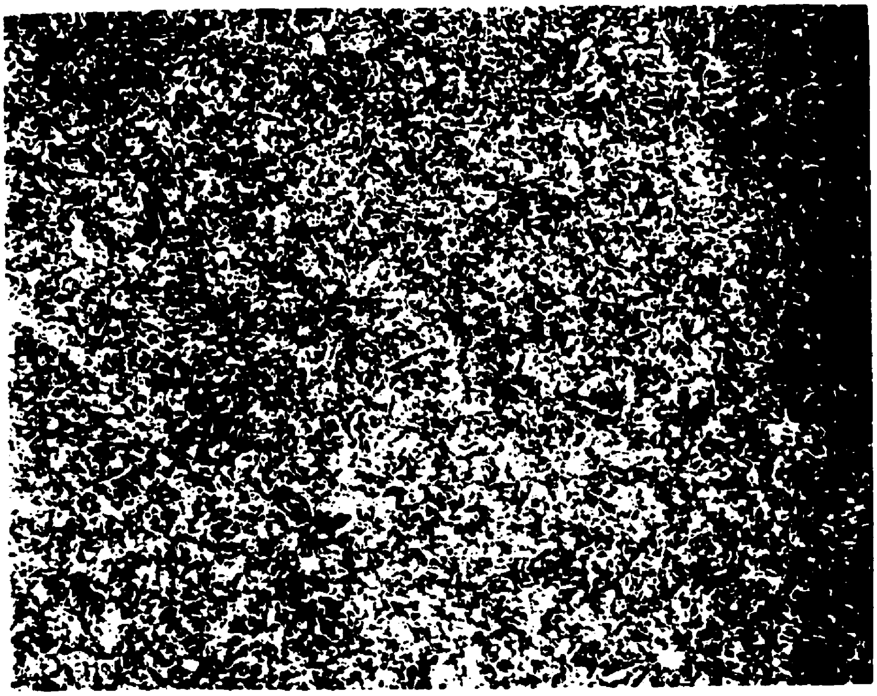

Figure 2.8: Sample D Pre-Test Optical Micrograph

2.4 EXPERIMENTAL PROCEDURE

This section describes the experimental procedure, post-test specimen preparation for examination and the procedure for the experimental evaluation.

2.4.1 Split Hopkinson Bar Procedure

Some explanations for the testing procedure are presented in this section. The preliminary preparation included lowering the hydraulic jack to the lowest position. Hydraulic jack was used to apply the torque to the portion of the incident bar. The torque was stored by the clamping mechanism. After the hydraulic jack was lowered, the release valve on the jack was tighten and the jack was prepared for applying the torque. Next, the notched bolt was placed in the slot and tightened with the wrench. The bolt was used in the clamping mechanism to serve as the torque release pin. As a safety measure, the protective mash was placed over the clamping mechanism because after the torque release by breaking the bolt, the broken pieces of the bolt fly all over. After the bolt and the mash were in place, the clamping mechanism was further tightened by the lever-wrench to secure the incident bar in the position during torque-storing by the hydraulic jack.

After all of the above was done in the exact sequence as described, the torque was applied to the loading arm connected to the incident bar. The load placed on the loading arm was 130 kg, which translated to the torque on the bar was 130 kg x 0.3 m = 382 Nm.

After the torque was stored, the specimen was placed in the slots between the incident and transmitter bars. The transmitter bar was then tightened in the opposite direction from the loading pulse to ensure that there was no gap between the specimen and the transmitter bar. Otherwise, the noise would have been initiated at the interface of the specimen and the transmitter bar which would result in invalid data.

With the specimen in place, all of the equipment for data collection was turned on and armed for capturing pulses. These include three wave-form recorders and oscilloscopes. The computer programme for storing the captured pulses by the recorders was initiated and test was ready to be performed.

Test proceeded in the following manner. With everything in place and ready as described above, the pin breaking bolt on the clamping mechanism was tightened until the notched bolt (or pin) fractured. Upon the fracture of the bolt, the torque was released and the loading pulse (the torsional wave) travelled down the incident bar from the clamping mechanism towards the specimen. When the pulse reached the specimen, part of it travelled through the specimen loading it and continuing down the transmitter bar. Another part reflected off the specimen and travelled back from the specimen towards the clamping mechanism. Three pulses were captured during this very short-time process. These three pulses included the incident pulse, the transmitted pulse and the reflected pulse. All of them were used later in the computer analyses to obtain the data on material response to the loading.

2.4.2 Post-Test Specimen Preparation

After the test was performed, specimens were prepared for examination. In order to examine the adiabatic shear band characteristics the gauge section needed to be separated from the hexagonal ends at both sides of the gauge section. In order to do this, a diamond saw was used to cut thin cuts as close to the hexagonal ends of the specimen as possible. After the gauge section (now the hollow thin-walled cylinder) was separated, the burrs left from cutting were removed by grinding.

The last preparation was cleaning the specimens in the ultrasonic cleaner in alcohol and subsequent etching of the localised plastic deformation area.

During this preparation, special care was taken to avoid touching the surface of the specimen in order to preserve as much as possible the morphology that was created during the tests.

2.4.3 Procedure For Experimental Evaluation

This section will explain the procedure used in the evaluation of the test data and what type of data were sought for.

The three different gauge length specimens were subjected to three different strain rates due to the length of the gauge section. The dependence of strain rate on the gauge length follows the following relation [53]

$$\dot{\gamma}_{\max} = \frac{2cD_s}{L_sD}\gamma_{\max} \cdot 0.25 \cdot 0.6$$

The equation works in a very close proximity with the experimental data on the strain rate. Here, c is the wave speed in Aluminum bar, D_s is the specimen mean diameter, L_s is the specimen gauge length, D is the diameter of the Hopkinson bar, $\gamma_{\max}$ is the maximum allowable shear strain in the Aluminum bar found to be 5.38×10^{-3} for this specific set-up. The factors 0.25 and 0.6 come from the fact that there is energy dissipation, and that the part of the produced energy is lost due to the pulse passing through the sample. As well, the maximum available load in the bar was limited to about 60 % in order to reduce the fatigue in the Aluminum bar which is very susceptible to fatigue failure.

When the specimen data are substituted in the above relation, the following strain rates were obtained, and they are in agreement with the experimentally obtained values.

Speed of sound in the bar $c = \sqrt{\frac{G}{\rho}} = \sqrt{\frac{26.9\ \frac{N}{m^2}}{2710\ \frac{kg}{m^3}}} = 3097\ \frac{m}{s}$

Specimen mean diameter $D_s = 13\,mm$

Specimen gauge length $L_s = \begin{array}{l} 3.00\,mm \\ 3.78\,mm \\ 10.00\,mm \end{array}$

Diameter of the bar $D = 25.4\,mm$

Maximum alowable strain in the bar $\gamma_{\max} = \frac{\tau_y}{G} = \frac{140 \cdot 10^6}{26 \cdot 10^9} = 5.38 \cdot 10^{-3}$

Gauge length 3.00 mm $\dot{\gamma}_{3.00} = \frac{2 \cdot 3097 \cdot 13 \cdot 10^{-3}}{3 \cdot 10^{-3} \cdot 25.4 \cdot 10^{-3}} \cdot 5.38 \cdot 10^{-3} \cdot 0.25 \cdot 0.6 = \mathbf{852\,s^{-1}}$

Gauge length 3.78 mm $\dot{\gamma}_{3.78} = \frac{2 \cdot 3097 \cdot 13 \cdot 10^{-3}}{3.78 \cdot 10^{-3} \cdot 25.4 \cdot 10^{-3}} \cdot 5.38 \cdot 10^{-3} \cdot 0.25 \cdot 0.6 = \mathbf{680\,s^{-1}}$

Gauge length 10.00 mm $\dot{\gamma}_{10.00} = \frac{2 \cdot 3097 \cdot 13 \cdot 10^{-3}}{10.00 \cdot 10^{-3} \cdot 25.4 \cdot 10^{-3}} \cdot 5.38 \cdot 10^{-3} \cdot 0.25 \cdot 0.6 = \mathbf{255\,s^{-1}}$

Specimens were observed under both Nikon Epiphot optical microscope and JEOL JXA - 840 scanning electron microscope. Both the surface of the specimen and the fracture surface inside the adiabatic shear band was examined. The fracture surface examination was conducted under the scanning electron microscope because of higher depth of focus and higher available magnification. Throughout the examination, the photographs of the adiabatic shear bands and fracture surfaces were taken for each specimen. For the sake of clarity, there were 4 specimens in each group of strain rate. Since there were three different strain rates, the number of specimens is 12. Table 2.5 presents the summary of the specimens used in the experiment.

Table 2.5: Summary of the Test Samples [♦]

A at 255 s^{-1}	A at 680 s^{-1}	A at 852 s^{-1}
B at 255 s^{-1}	B at 680 s^{-1}	B at 852 s^{-1}
C at 255 s^{-1}	C at 680 s^{-1}	C at 852 s^{-1}
D at 255 s^{-1}	D at 680 s^{-1}	D at 852 s^{-1}

[♦] A, B, C, D stands for the specimen heat treatment designation, and number after the letter designation stands for the strain rate at which the specimen was tested.

The local strain measurement in the sample was performed simply by measuring the shear angle γ in radians and taking its tangent. Figure 2.9 illustrates the procedure for obtaining the local strain. Measurement of the adiabatic shear band width was taken from the photomicrographs for each sample and is measured in micrometers.

The measurement of the number of dimples per square millimetre was somewhat more complicated. It was performed by the method similar to intersect method used to obtain the grain size. Measurement was taken from the photomicrograph for each sample. The procedure was to draw about 20 lines in different directions on the high magnification photograph of the fracture surface. The number of intersections between each line and dimple was recorded. By comparing, it was possible to find the number of dimples per line length, and from there, knowing the magnification of the photograph, it was possible to find the number of dimples per square millimetre. The error involved with this procedure was negligible on the final result since the number of dimples was too great (from over 1 million to over 16 million).

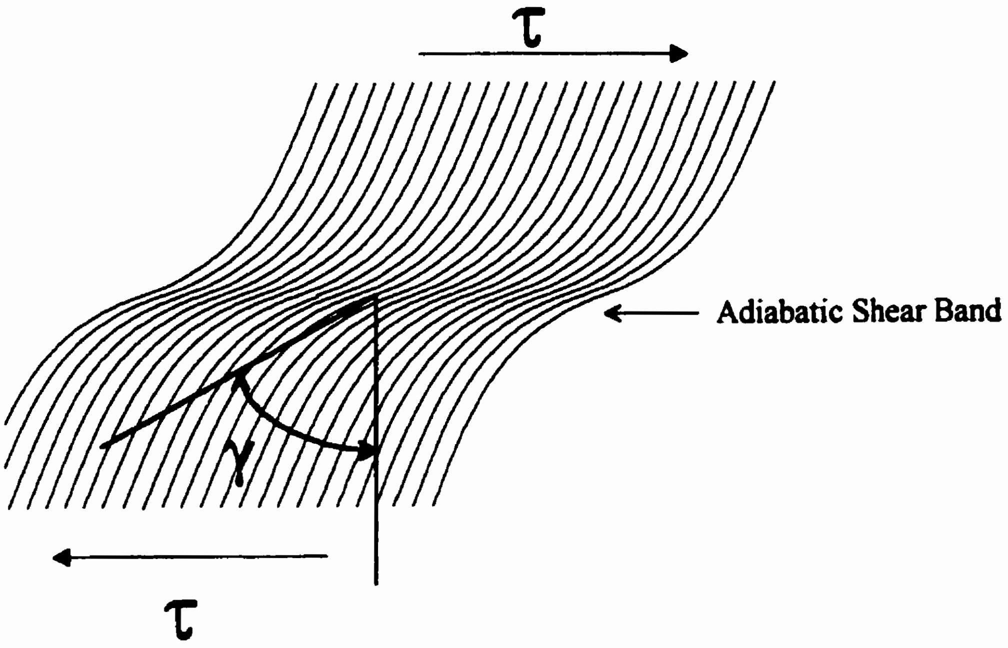

Figure 2.9: Measurement of the Local Strain in the Sample

CHAPTER 3 RESULTS

3.1 INTRODUCTION

This chapter presents the results obtained from the torsional split Hopkinson bar tests. It presents the photomicrographs of the adiabatic shear bands and fracture surfaces for all samples tested. The chapter is subdivided into sections according to the strain rate that was applied to the sample. The discussion on the findings is presented in the next chapter.

3.2 SHORT GAUGE LENGTH - STRAIN RATE 852 s^{-1}

3.2.1 Adiabatic Shear Band Morphology

This section describes the morphology of the adiabatic shear bands on the surface of the specimens. The strain rate applied to these samples was 852 s^{-1} due to their shortest gauge length of only 3.00 millimetres. Specimens tested in this strain rate range were all four groups of microstructure and hardness, i.e., group A, B, C and D.

Figure 3.1 shows the adiabatic shear band in sample A. The shear band is of transformed type with local strain of 275 % and width of 120 μm. It is seen from the photomicrograph that only the locally deformed region exists. The rest of the material is not deformed. This also suggests the transformed type of the band.

The adiabatic shear band in specimen B is presented in figure 3.2. It shows the transformed type of the band with microcracks formed within the band. The cracks formed inside the band originate at interfaces between the ferrite and pearlite or are

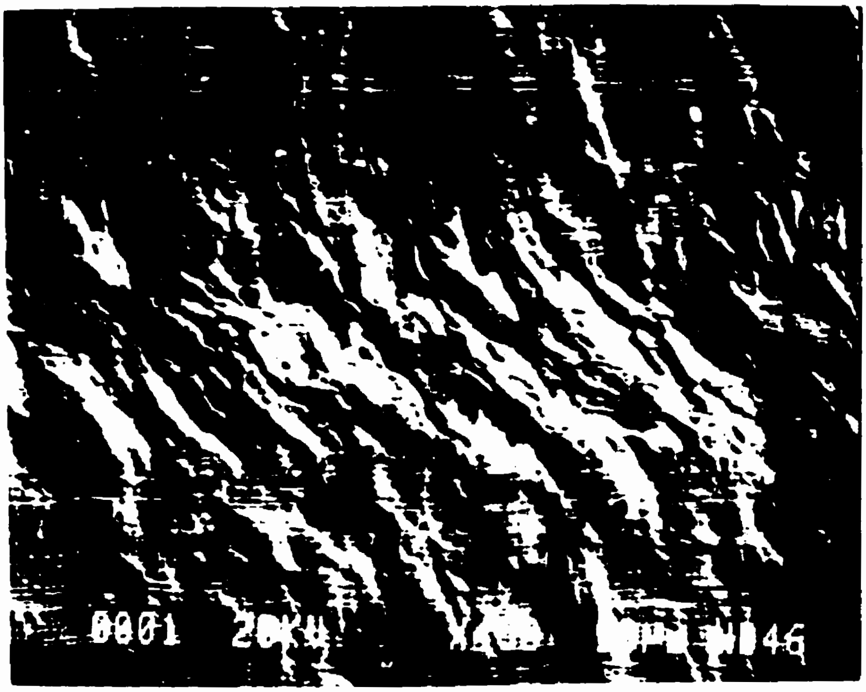

Figure 3.1: ASB in Sample A Tested at 852 s^{-1}

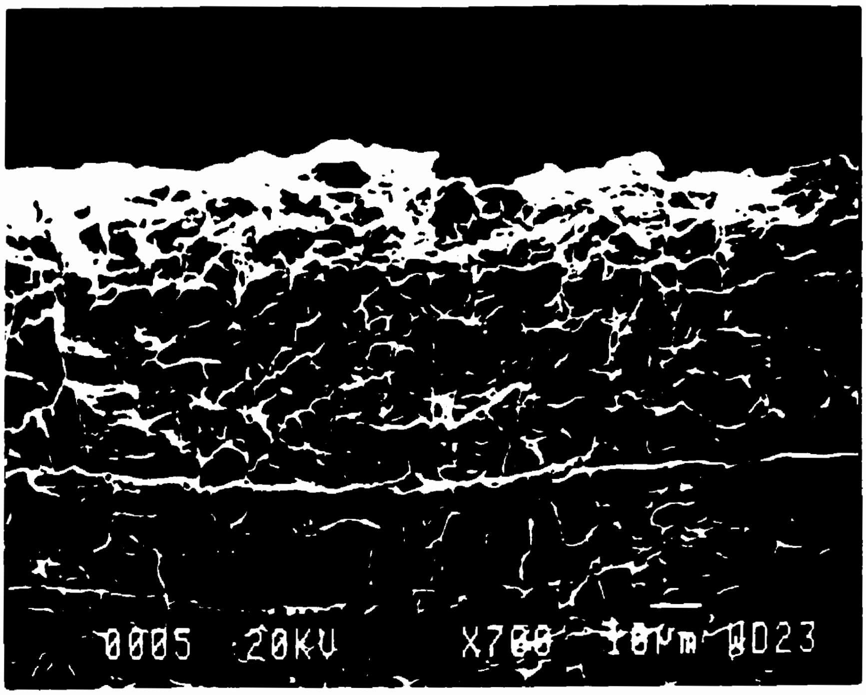

Figure 3.2: ASB in Sample B Tested at 852 s^{-1}

formed by decohesion between lamellae of a single pearlite grain. As presented in section 2.3.5 in Chapter 2, the pre-test microstructure of sample B consists of pearlite and ferrite grains. The cracks originate at the interface because of the great difference in strength of soft ferrite and hard pearlite phases. It is also observed from figure 3.2 that the fracture is of intergranular type. As will be presented later in the chapter, the fracture surface of all the specimens tested shows the ductile mode of failure characterised by dimples. The width of the band for sample B is 157 *um*, and local strain was not available due to the material transformation in the band.

Sample C also produced the transformed type of the band when tested at this strain rate with the band width of 100 *um*. The local strain measurement was impossible to obtain for the same reason as for the sample B. The shear band appearance for sample C is presented in figure 3.3. As in sample B, the microcracks formed inside the band are evident. However, the nucleation sites for cracks in this sample are different than nucleation sites for cracks in sample B due to different original microstructures. Sample C has structure of tempered martensite, and nucleation sites for the cracks are most probably prior austenitic grain boundaries present in the original microstructure of sample C. It is believed that prior austenitic grain boundaries served as sites for the initial carbide precipitation during tempering. With these strong boundaries occupied by carbides, there exist large difference in strength between the boundaries and surrounding softer phase consisting of martensite and ferrite-carbide phase, which led to cracking along these boundaries.

The adiabatic shear band in specimen D is presented in figure 3.4. The band is of transformed type with width of 58 *um* and local strain of 275 %. Cracks were present in this sample as well, and the crack nucleation sites are believed to be the interfaces between carbide phases and softer ferrite phase.

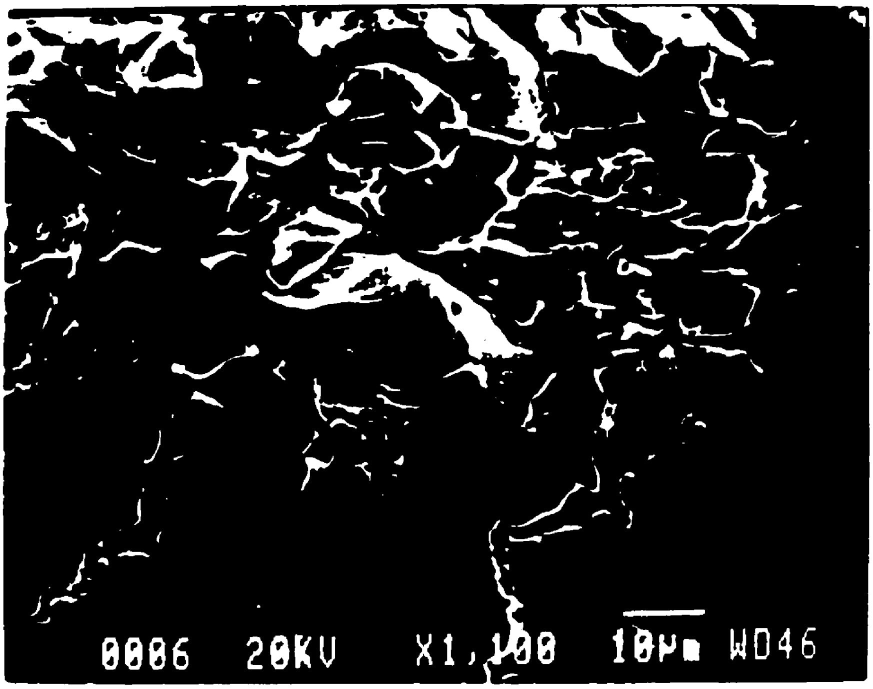

Figure 3.3: ASB in Sample C Tested at 852 s^{-1}

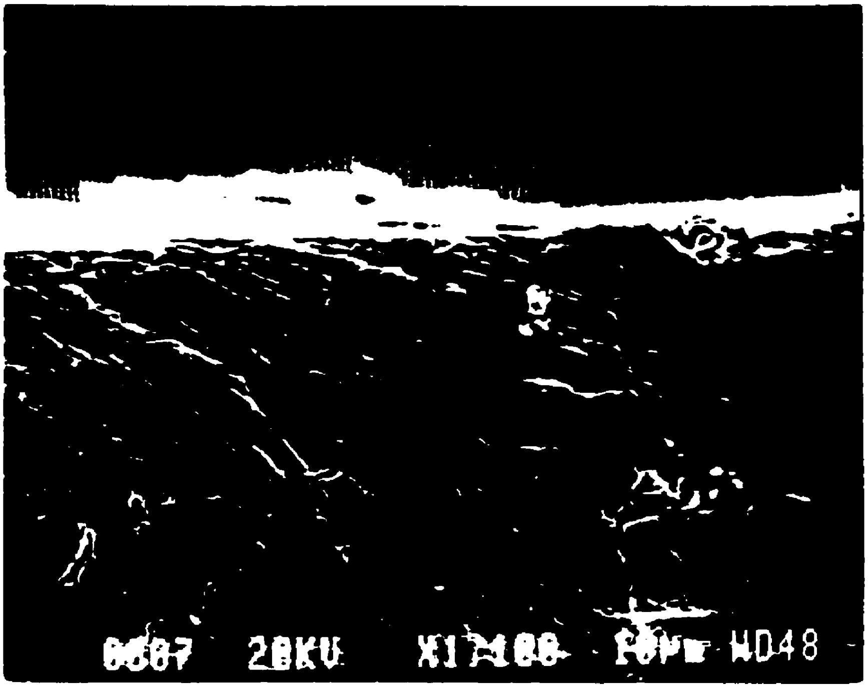

Figure 3.4: ASB in Sample D Tested at 852 s^{-1}

3.2.2 Fracture Surface of the Band

All the specimens tested exhibited the fracture inside the band. The fracture surface is characterised by the ductile dimples, which indicates the ductile mode of fracture. Same type of the ductile fracture was found in all samples, with the difference in the size of the dimples. Figures 3.5 to 3.8 present the fracture surfaces of samples A, B, C and D respectively. This section presents the photomicrographs of the fracture surfaces, while the Chapter 4 presents the discussion on specific aspects of the fracture surface.

It was found that the hardness does not have the influence on he fracture type, but it has the influence on the size of ductile dimples. More on this relationship is presented in Chapter 4.

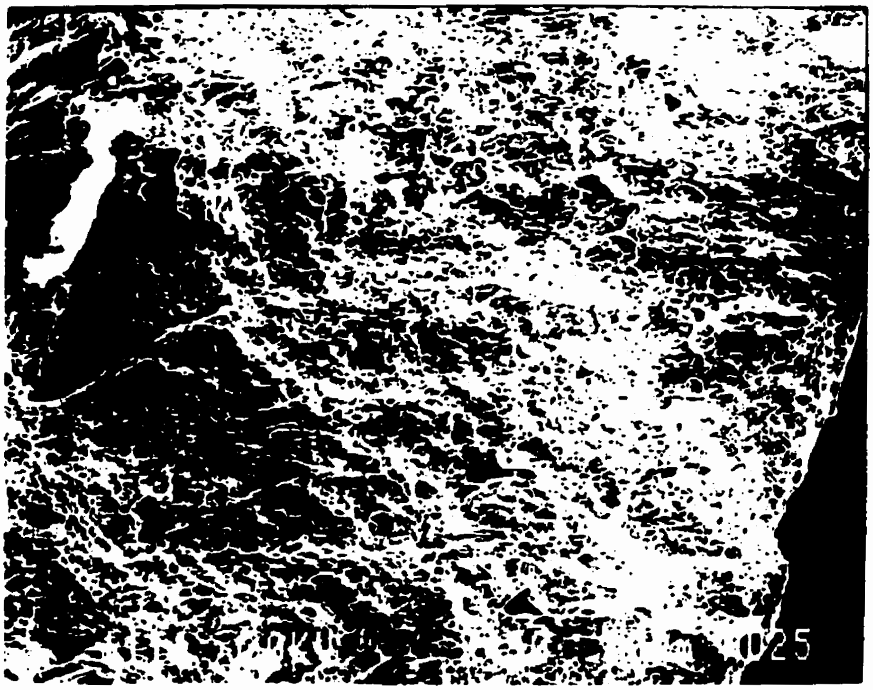

Figure 3.5: Fracture Surface of Sample A Tested at 852 s^{-1}

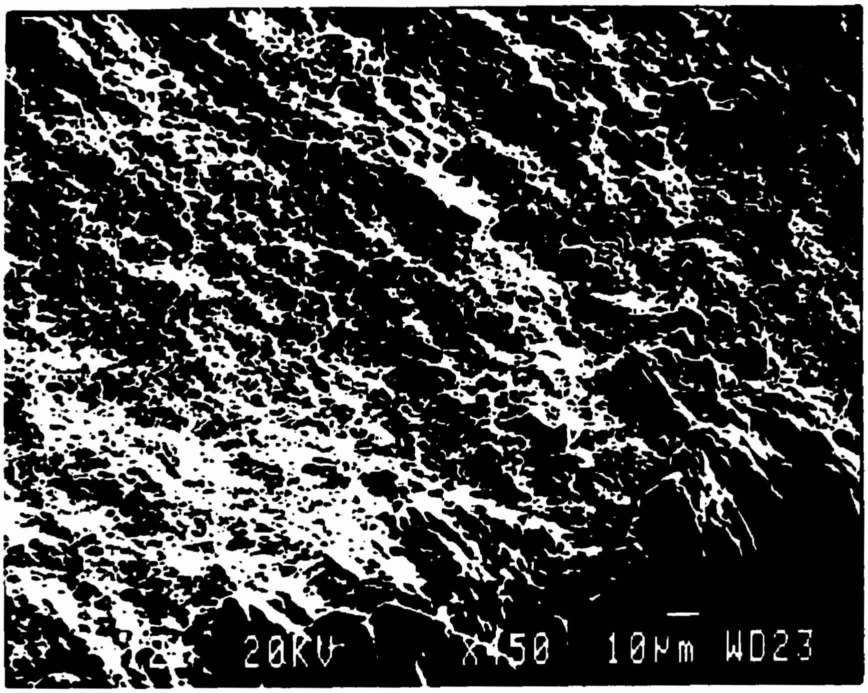

Figure 3.6: Fracture Surface of Sample B Tested at 852 s^{-1}

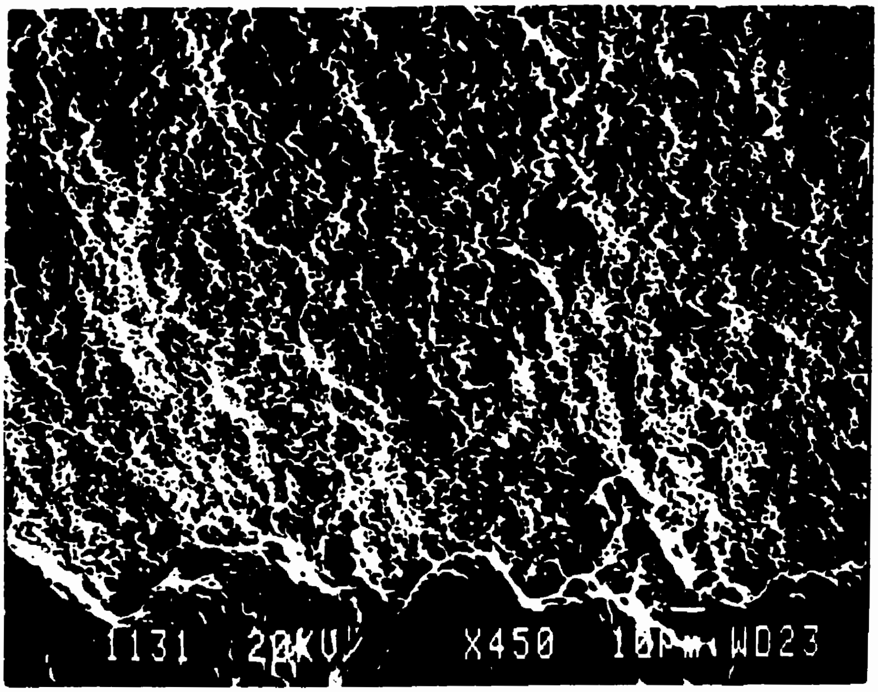

Figure 3.7: Fracture Surface of Sample C Tested at 852 s^{-1}

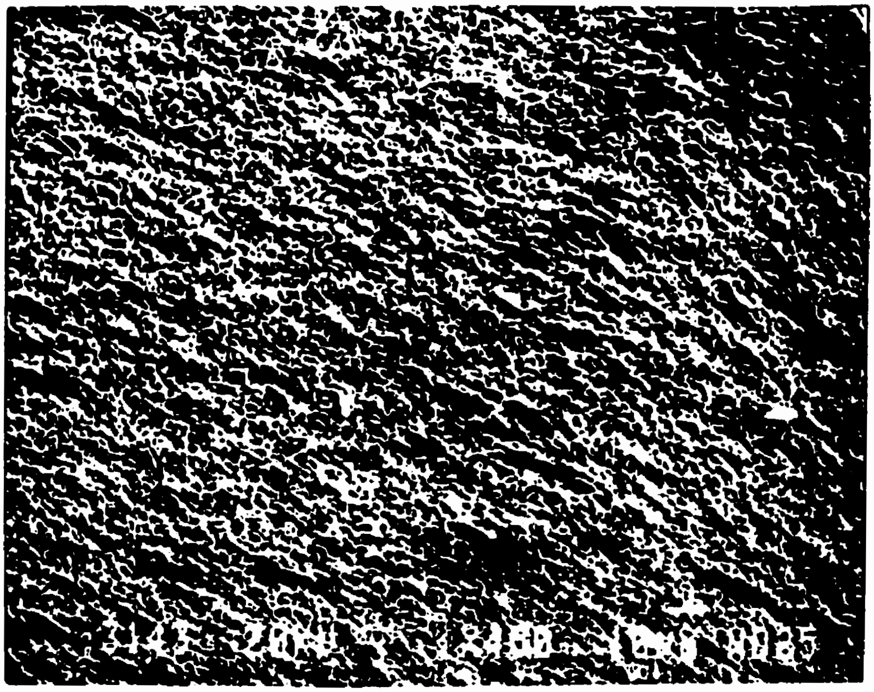

Figure 3.8: Fracture Surface of Sample D Tested at 852 s^{-1}

3.3 MEDIUM GAUGE LENGTH - STRAIN RATE 680 s^{-1}

3.3.1 Adiabatic Shear Band Morphology

All the specimens tested at strain rate of 680 s^{-1} exhibited the adiabatic shear band. However, the type of the band is not the same for all specimens as it was for the strain rate of 852 s^{-1}.

Sample A exhibited the deformed type of the band and the band appearance is presented in figure 3.9. Figure 3.10 presents the same band but the surface was etched and the microstructure of the band was revealed. It is clear that the material in the band did not undergo any phase transformation. The microstructure inside the band consists of the same ferrite-pearlite structure as the original pre-test microstructure. It is evident, though, that the material exhibited heavy local strain characterised by the elongated grains within the band. The shear band width for sample A is 220 μm, with the local strain of 470 %.

Figure 3.11 presents the adiabatic shear band for sample B. The material exhibited the same deformed type of the band as the sample A. The etch-revealed microstructure of the band is presented in figure 3.12. From this figure, it is evident that the band is of deformed type since the microstructure consists of ferrite and pearlite elongated grains due to the high local straining. As seen in figure 3.12, this material exhibited two parallel shear bands whose formation will be given more detailed discussion in Chapter 4. The width of the band is 280 μm with the local strain of 275 %.

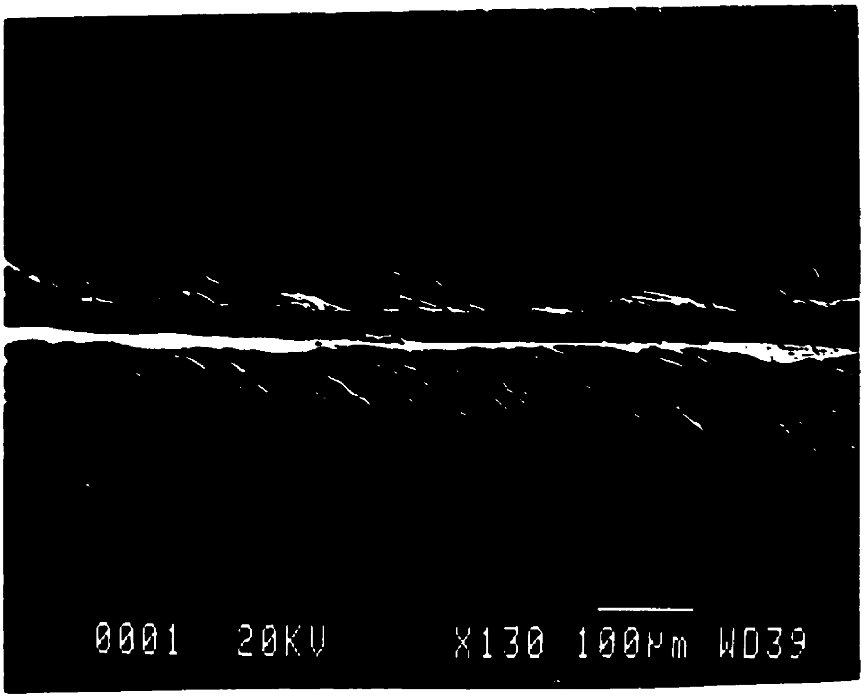

Figure 3.9: ASB in Sample A Tested at 680 s^{-1}

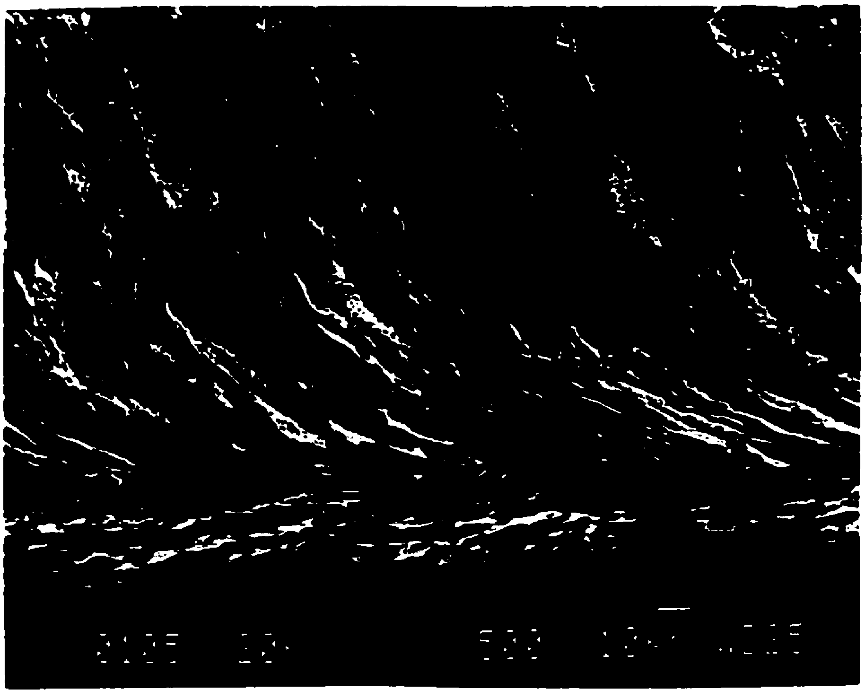

Figure 3.10: ASB in Sample A - Etched, Tested at 680 s^{-1}

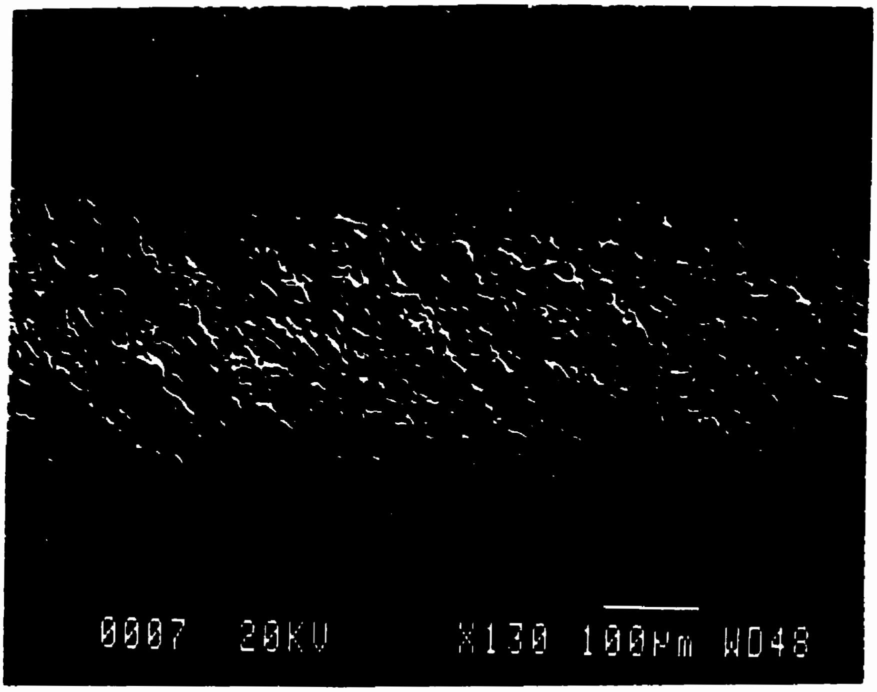

Figure 3.11: ASB in Sample B Tested at 680 s^{-1}

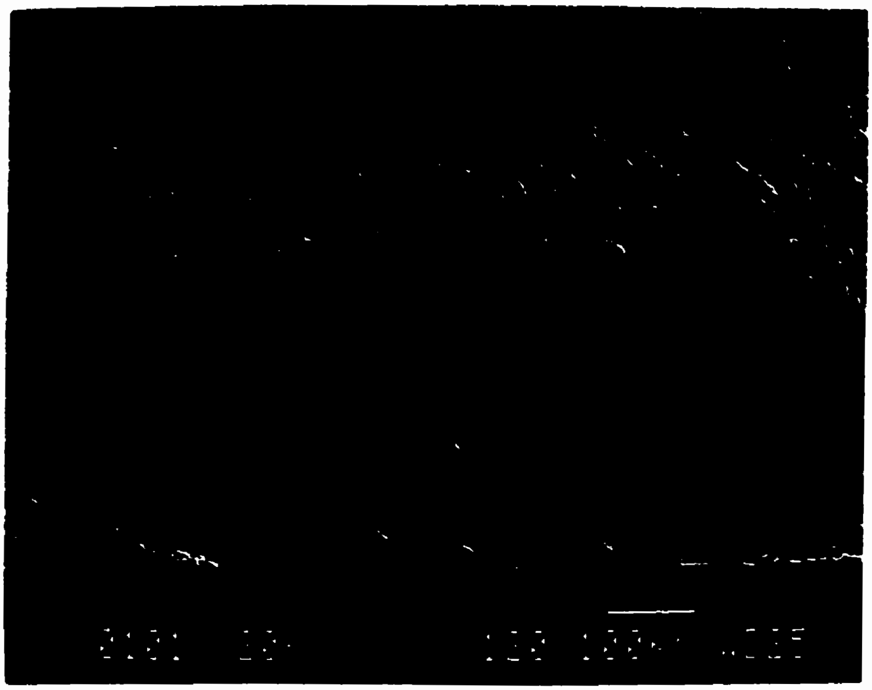

Figure 3.12: ASB in Sample B - Etched, Tested at 680 s^{-1}

Sample C exhibited the transformed type of the band. The adiabatic shear band morphology is presented in figure 3.13, and the etched band with revealed microstructure is presented in figure 3.14. It is seen from figure 3.14 that the microstructure of the band differs from the original pre-test microstructure of this material. The band etched white with Nital, and it is seen that the surrounding material did not experience any deformation whatsoever, while the material in the band experienced heavy localised shear deformation with shear strain of 348 %. The band width for this sample is 180 μm. The formation of the transformed band was discussed in detail in Chapter 1 and is not repeated here.

Figure 3.15 presents the adiabatic shear band in sample D. The band is of transformed type and photomicrograph of the etched band is presented in figure 3.16. As with sample C, the band etched white with Nital, and has experienced heavy localised strain of 173 %, while the surrounding material did not undergo any plastic shearing. This is a characteristic of the transformed type of the shear band. The shear band width for this sample is 108 μm. Figure 3.15 also shows the initiation of microcracks in the shear band of sample D. The nucleation sites for crack initiation are the same as described for sample D tested at strain rate of 852 s^{-1}, i.e., decohesion between the carbide and ferrite phases or between retained martensite and ferrite.

The fracture surface morphologies for this strain rate range are not presented here. The discussion on the influence of hardness and microstructure on fracture will be based on available data for strain rates of 852 s^{-1} and 255 s^{-1} and is presented in Chapter 4.

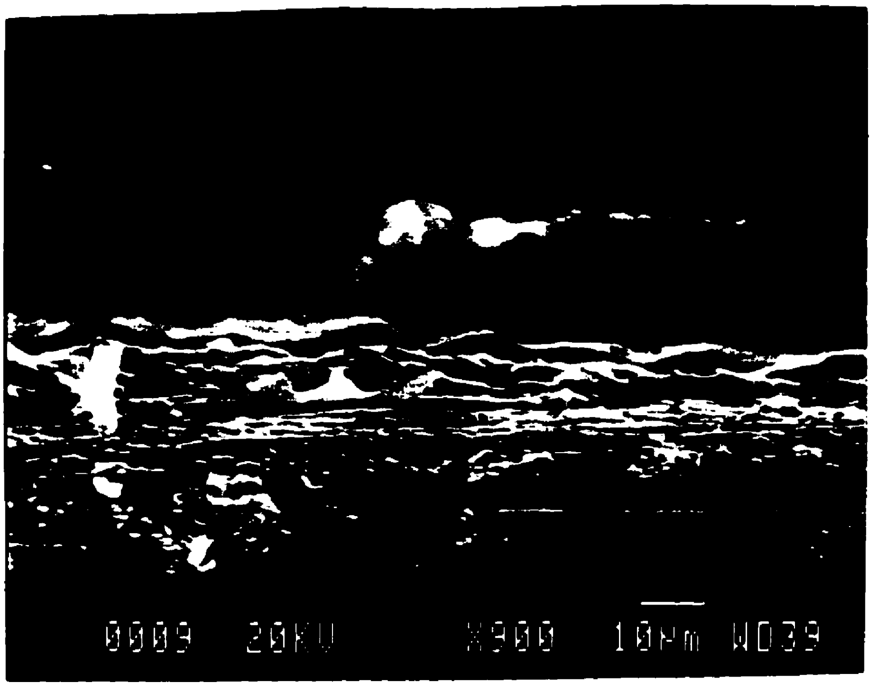

Figure 3.13: ASB in Sample C Tested at 680 s^{-1}

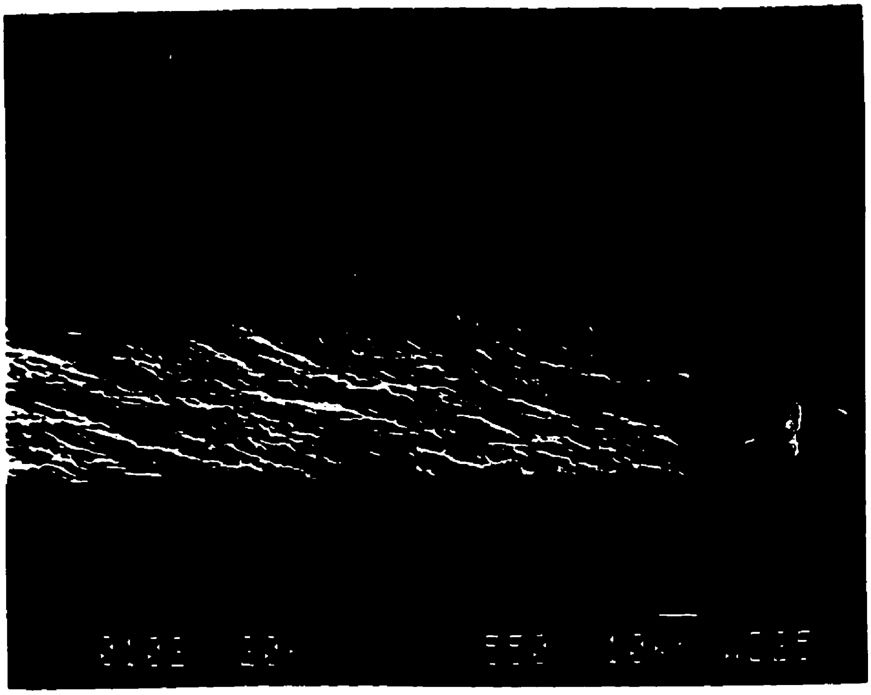

Figure 3.14: ASB in Sample C - Etched, Tested at 680 s^{-1}

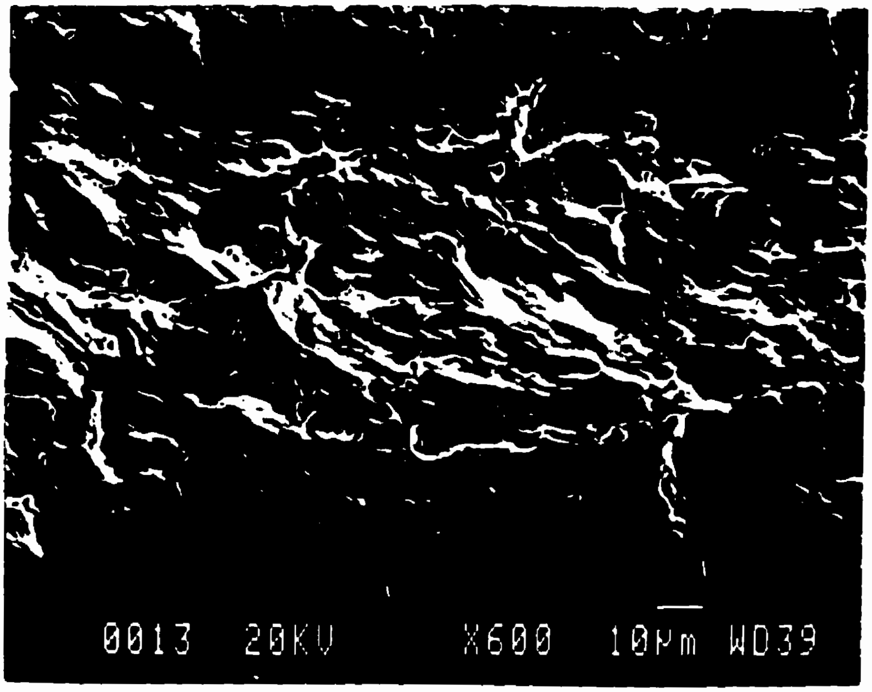

Figure 3.15: ASB in Sample D Tested at 680 s^{-1}

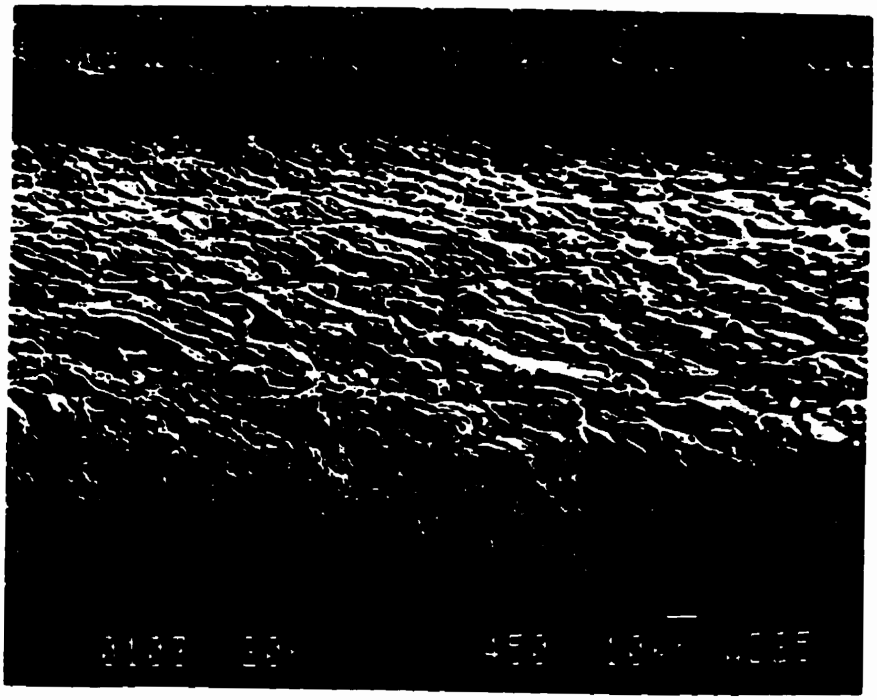

Figure 3.16: ASB in Sample D - Etched, Tested at 680 s^{-1}

3.4 LONG GAUGE LENGTH - STRAIN RATE 255 s^{-1}

3.4.1 Adiabatic Shear Band Morphology

Specimens tested at strain rate of 255 s^{-1} all exhibited the deformed type of the shear band. For comparison, it was seen that samples tested at 852 s^{-1} all exhibited the transformed adiabatic shear band, samples tested at 680 s^{-1} exhibited either transformed or deformed type of the band, and samples tested at 255 s^{-1} all exhibited the deformed type of the band.

Figure 3.17 presents the shear band formed in specimen A. The band is of deformed type with width of 300 μm and local strain of 275 %.

Sample B exhibited also a deformed type of the shear band and is shown in figure 3.18. The visible microcracks are formed in the same manner described for sample B in section 3.2.1. The width of the band is 340 *um* with local strain within the band of 100 %.

The adiabatic shear band formed in sample C is presented in figure 3.19. The band is of deformed type as well, with the width of 200 *um* and local strain of 143 %.

The shear band for sample D is presented in figure 3.20. The band is also deformed type with local strain of 100 % and width of 130 *um*.

The details of formation of the shear bands formed in samples tested at strain rate of 255 s^{-1} are analogous to ones explained for the samples tested at two previous strain rates and are therefore not discussed in more detail here.

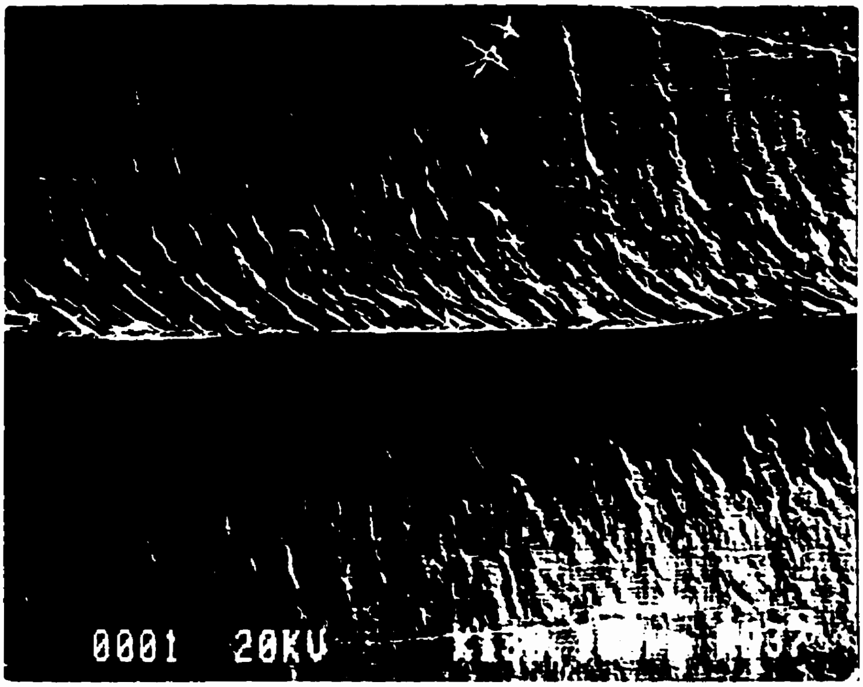

Figure 3.17: ASB in Sample A Tested at 255 s^{-1}

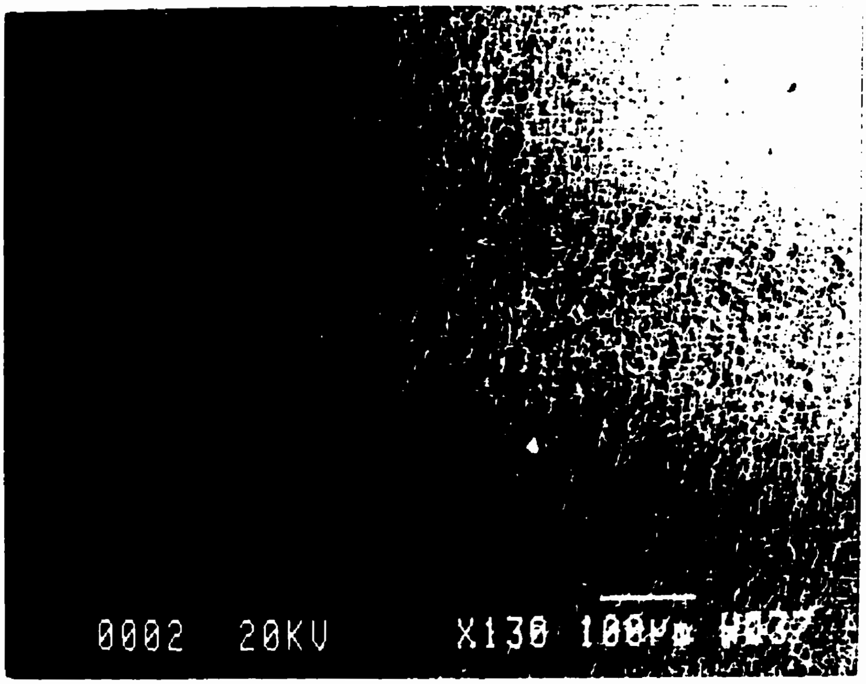

Figure 3.18: ASB in Sample B Tested at 255 s^{-1}

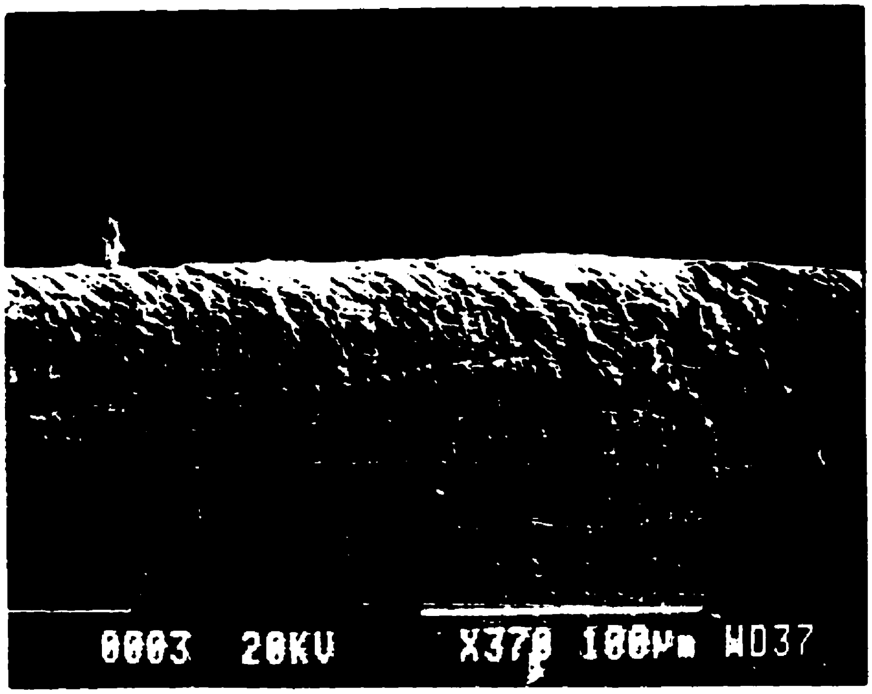

Figure 3.19: ASB in Sample C Tested at 255 s^{-1}

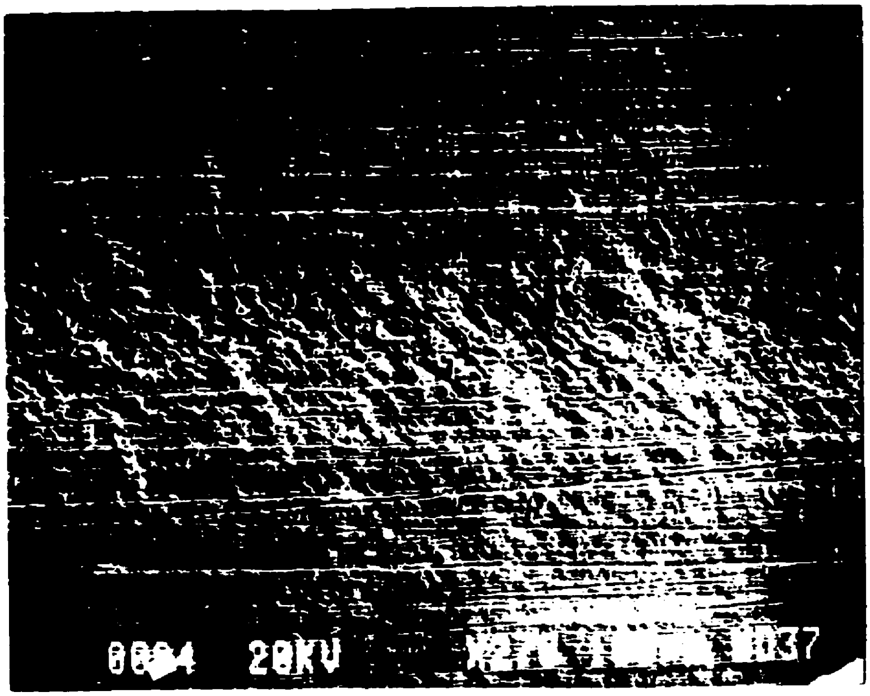

Figure 3.20: ASB in Sample D Tested at 255 s^{-1}

3.4.2 Fracture Surface of the Band

As with samples tested at strain rate of 852 s^{-1} described in section 3.2, all of the samples tested at strain rate of 255 s^{-1} exhibited fracture along the shear band. The fracture type is ductile characterised by the ductile dimples formed at the fracture surface. The fracture surfaces for samples A, B, C and D are presented in figures 3.21 to 3.24 respectively. As mentioned, all of the four samples showed ductile fracture, with the difference of the dimple size. The harder samples showed smaller dimples than the softer samples.

More on the characterisation of the fractures is presented in Chapter 4 on discussion of the results.

It is worth summarising here some of the characteristics of the shear bands and fractures formed in all of the tested samples. Samples tested at strain rate of 852 s^{-1} all showed the transformed type of the band with ductile fracture along the centre line of the band. Strain rate of 680 s^{-1} caused mixed types of the bands. Thus, samples A and B exhibited deformed shear bands, while samples C and D showed the transformed bands. Samples tested at strain rate of 255 s^{-1} all exhibited deformed types of shear bands with the ductile type of fracture along the shear band. The concise summary of the findings is presented in table 3.1 and presents data on the type of the band, width and local strain.

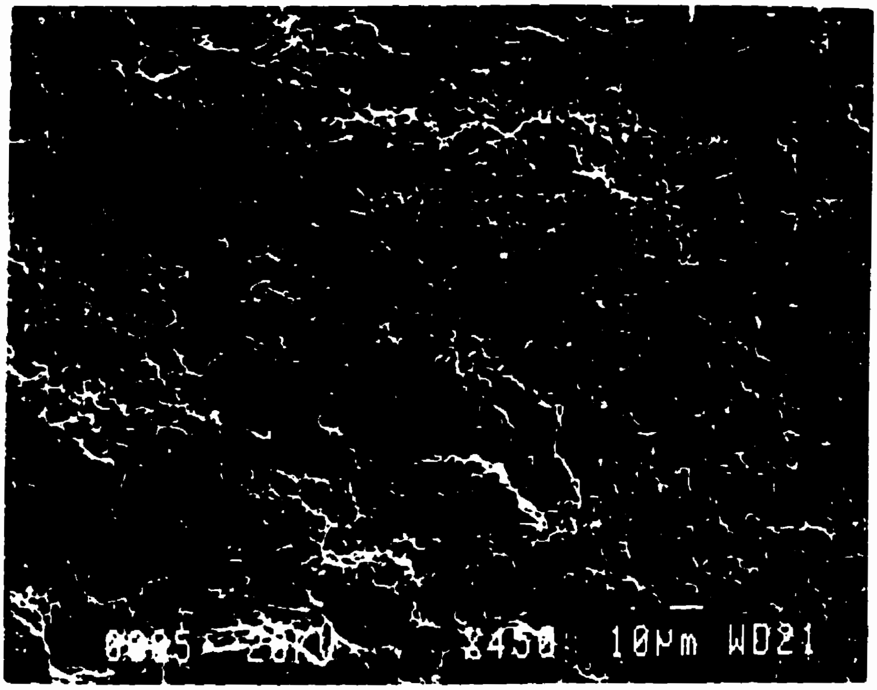

Figure 3.21: Fracture Surface of Sample A Tested at 255 s^{-1}

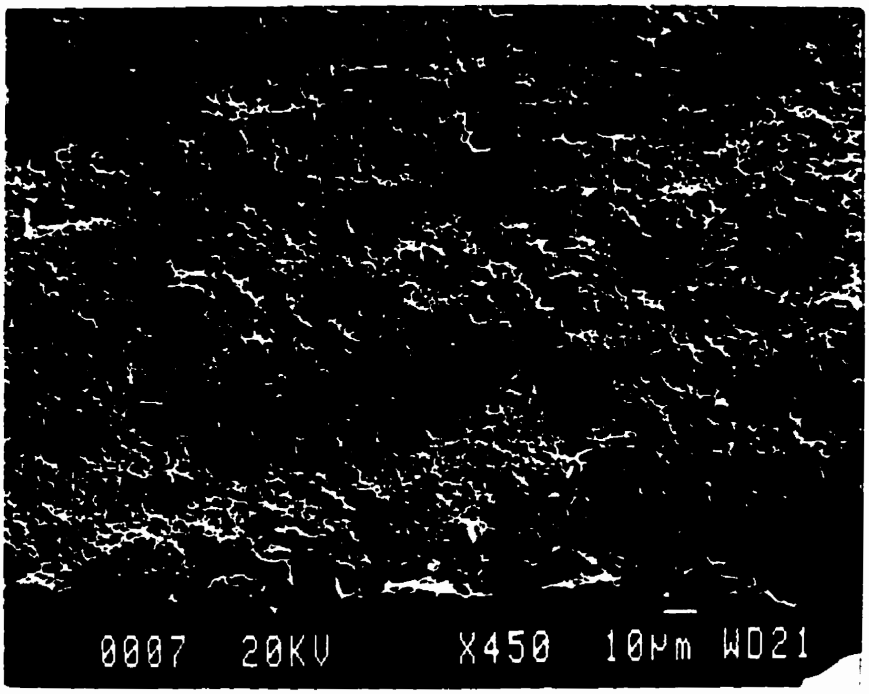

Figure 3.22: Fracture Surface of Sample B Tested at 255 s^{-1}

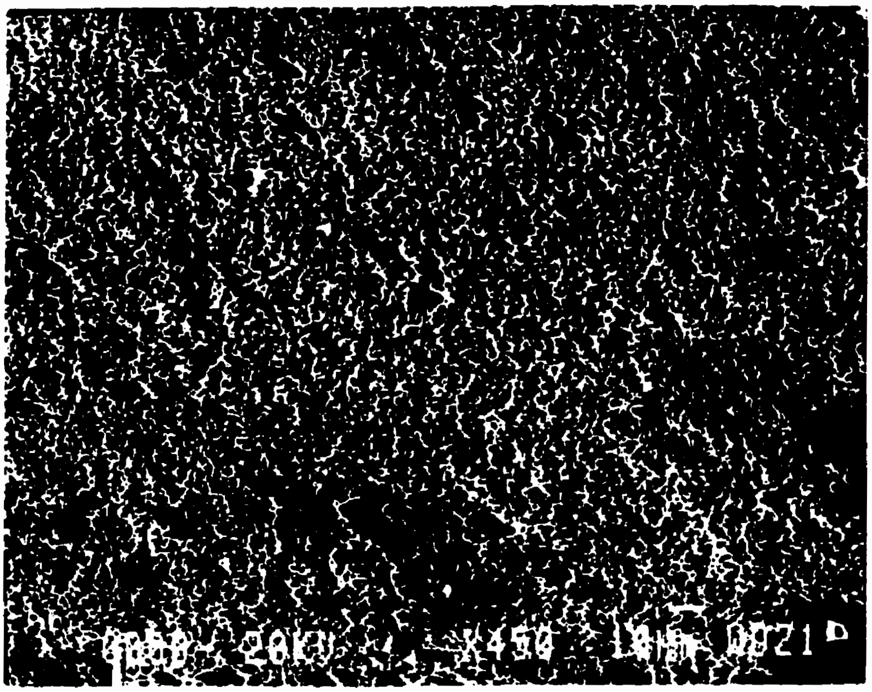

Figure 3.23: Fracture Surface of Sample C Tested at 255 s^{-1}

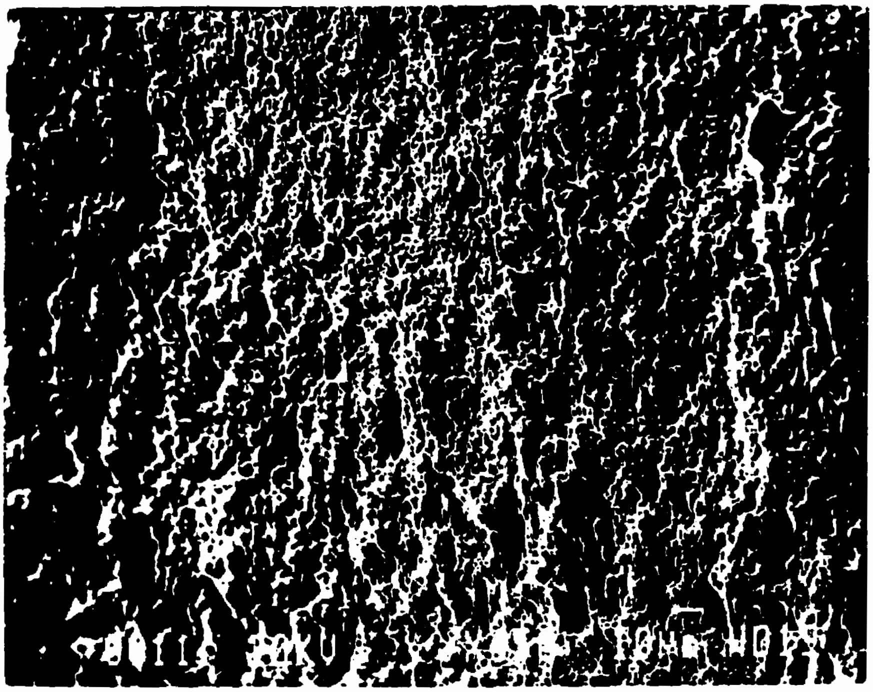

Figure 3.24: Fracture Surface of Sample D Tested at 255 s^{-1}

Table 3.1: Summary of the Test Data

Strain Rate	**Sample**	**Type of ASB**	**ASB Width (μm)**	**Local Strain (%)**
852 s^{-1}	A	Transformed	120	275
	B	Transformed	157	❖
	C	Transformed	100	❖
	D	Transformed	58	275
680 s^{-1}	A	Deformed	220	470
	B	Deformed	280	275
	C	Transformed	180	348
	D	Transformed	108	173
255 s^{-1}	A	Deformed	300	275
	B	Deformed	340	100
	C	Deformed	200	143
	D	Deformed	130	100

❖ Data not available.

CHAPTER 4 DISCUSSION

4.1 INTRODUCTION

Test results described in Chapter 3 are discussed in more detail here. The nature of the shear bands is discussed with some characteristics not described in Chapter 1. Nucleation of the shear band by void nucleation and coalescence is presented evidence in this chapter along with some evidence of high temperature rise within the band during its formation.

This chapter concerns primarily with material hardness, microstructure, and applied strain rate influence on the adiabatic shear band formation and fracture characteristics.

4.2 TRANSFORMED VERSUS DEFORMED SHEAR BAND

As presented in Chapter 3, depending on the strain rate and material hardness and microstructure, there can exist either deformed shear band or transformed shear band. The difference in the appearance of these two types of the band is shown in figures 3.10 and 3.12 which show the deformed type of the band, and figures 3.14 and 3.16 which show the transformed type of the band. The main distinction between these two types of the band is in the microstructure of the band material. Deformed bands have the original microstructure characterised by some recrystallisation that usually leaves finer microstructure than the original one. Figure 4.1 shows the microstructure inside the deformed band occurred in sample A tested at strain rate of 680 s^{-1}. It is seen that the structure inside the band is the same as the structure surrounding the band, i.e., the original, matrix material. The characteristic appearance is elongated grains within the

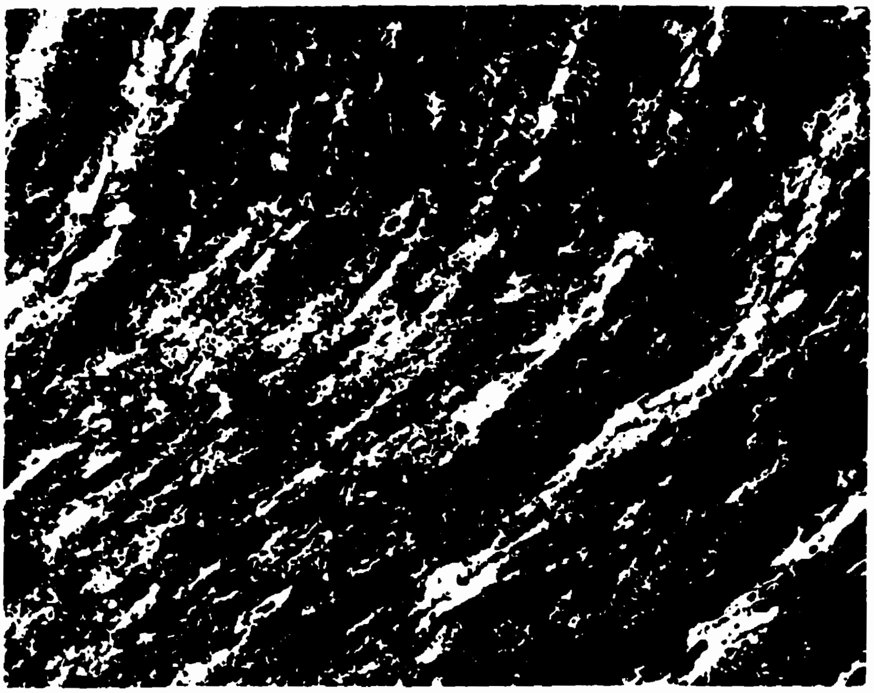

Figure 4.1: Optical Micrograph of Deformed Shear Band

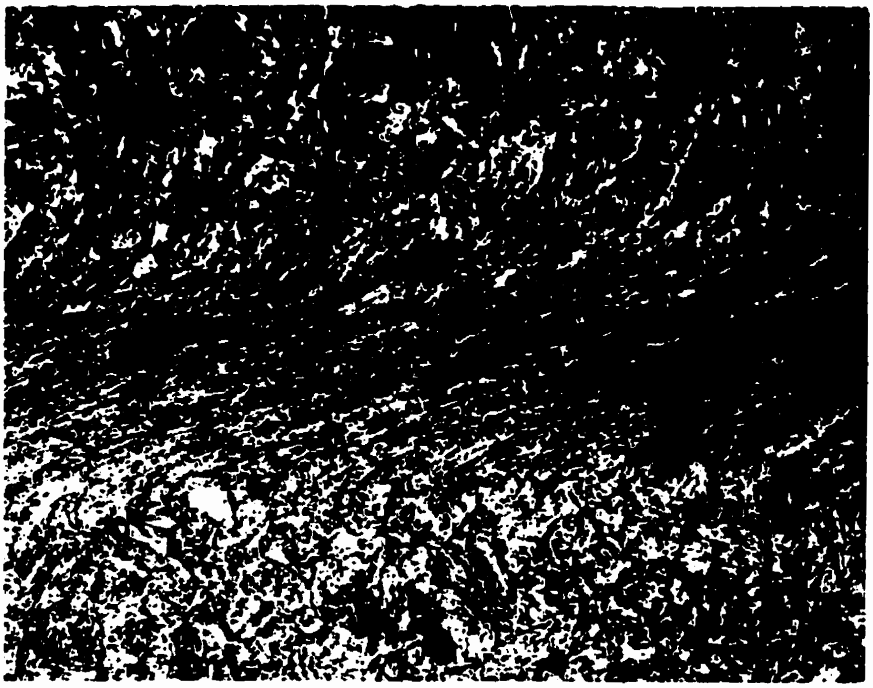

Figure 4.2: Optical Micrograph of Transformed Shear Band

band depicted as black and white stringer-like pearlite-ferrite grains. The elongation appears as a result of very high local strain inside the band (470 % for sample A in figure 4.1). The recrystallisation takes place as a result of very high temperature rise within the shear band that leads to enough thermal energy for recrystallisation to occur.

The process of formation of the deformed shear band in pearlitic steel (samples A and B) can be explained through the difference in strength of adjoining phases. During the deformation process, the weaker ferrite phase will take the majority of the deformation. The pearlite phase consisting of lamellae of cementite and ferrite will also take certain amount of deformation in its ferrite lamellae since they are weaker than the cementite lamellae.

Figure 4.2 presents the typical optical photograph of the transformed shear band. It is evident from photomicrograph that the material within the band has different microstructure from the surrounding matrix material which has the original pre-test microstructure. The original structure is tempered martensite characterised by carbide particles in ferrite matrix (lite) and martensite (dark). The microstructure of the shear band is typical of untempered martensite which suggests that the phase transformation occurred due to very high temperature rise within the band followed by rapid quenching of the material in the band by the surrounding matrix material.

4.3 MULTIPLE SHEAR BAND FORMATION

Chapter 3 focused only on the types and characteristics of the shear bands formed in different material microstructures. There is however, additional characteristic of the shear band formation that was not mentioned so far, and that is the multiple shear band occurrence. The number of shear bands formed in the sample depends on the material and on the strain rate as well as on the length of the gauge section. In this experiment, it was observed that the number of shear bands depended strongly on the gauge length. The number of shear bands ranged from 1 to more than 10. Specimens with the shortest gauge length of 3.00 mm exhibited from 1 to 3 shear bands, the same number as medium gauge length (3.78 mm) specimens. Specimens with long gauge length of 10.00 mm showed from 1 to more than 10 parallel shear bands. Sample A tested at 255 s^{-1} was the sample with the highest number of shear bands (more than 10). Figure 4.3 shows the multiple shear band in sample A tested at 852 s^{-1}. It was also observed that during fracture, the propagating crack along the shear band can change the plane of propagation and jump from one band to another, leaving steps on the fracture surface. Figure 4.4 shows two bands joined together by the propagating crack.

4.4 VOID NUCLEATION AND FRACTURE

As mentioned earlier in Chapter 3, the fracture surface in all samples tested appeared to be characterised by dimples which is the indication of ductile fracture. The dimple size varied according to the specimen hardness and strain rate and is discussed in more detail in section 4.5. This section deals with characteristics of the fracture surfaces exhibited by all samples tested.

High magnification of the fracture surface for sample B tested at 255 s^{-1} is presented in figure 4.5. In all specimens tested, there was no indication of brittle fracture. All specimens exhibited the same fracture surface appearance as presented for sample B in figure 4.5, with the difference in the size of the dimples. It is believed that the fracture is ductile because of the very high temperature rise within the band during deformation. The major portion of the plastic work generated during straining is converted into heat which softens the material in the shear band. Since the fracture is ductile, it was concluded that crack formed and propagated before material in the band cooled down or was quenched by the surrounding matrix in the case of the transformed band formation. Therefore, the fracture occurred while the material was still hot. If it were

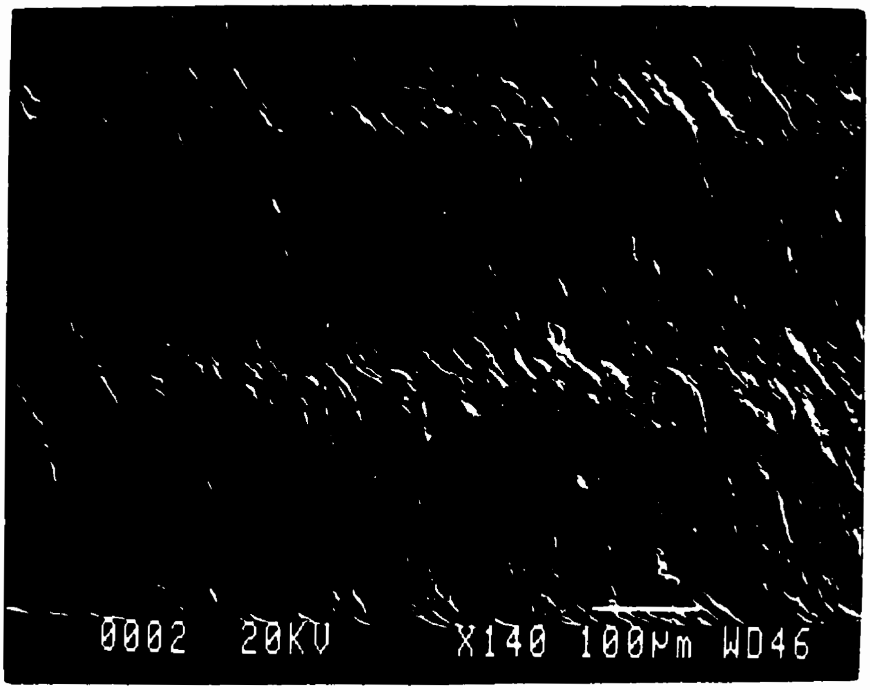

Figure 4.3: Triple Shear Band in Sample A at 680 s^{-1}

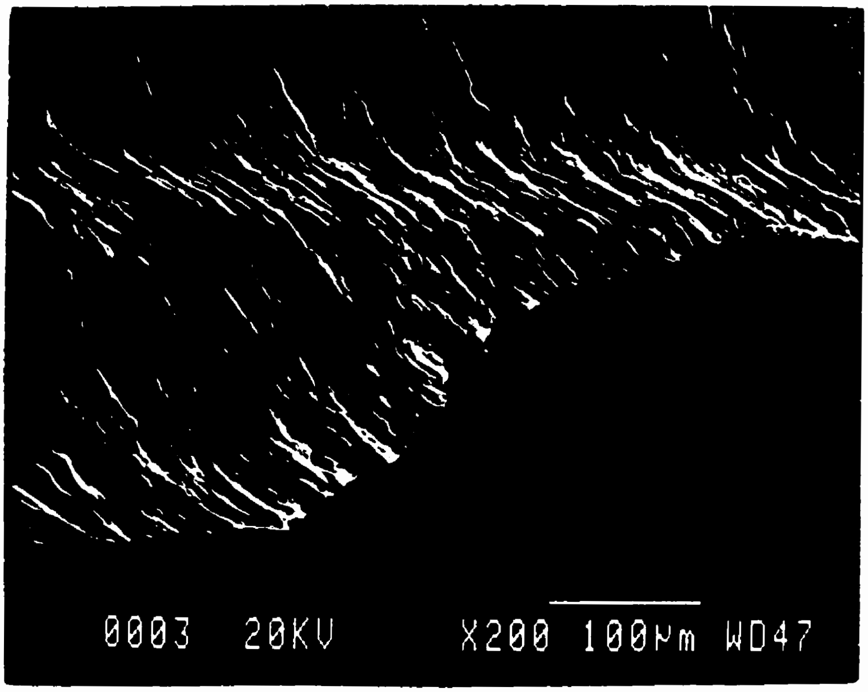

Figure 4.4: Two Shear Bands Joined By the Crack

supposed that fracture occurred after the band material was quenched by the surrounding matrix, that would indicate that the band was already formed and the material in the band was already hard. Under these conditions, the fracture type would most certainly be brittle fracture characterised by cleavage. Since cleavage was not observed in any sample, it was concluded that the fracture occurred during the band formation while the material was still hot from the temperature released by plastic work done during shear deformation.

The evidence of the high temperature released within the band during the adiabatic shear band formation is seen in knobbly structure formed on dimple peaks on the fracture surface. Figure 4.6 shows this for sample B tested at 680 s^{-1}. This knobbly appearance suggests that there was melting of the material inside the band due to high temperature. Melting of the surface can be produced either by the temperature released during plastic work, or can be produced by temperature release due to rubbing two surfaces against each other. However, in this case, it seems that the temperature responsible for melting comes from the plastic work, because otherwise, the surface would be smeared rather than fully developed, dimple-like.

As it was mentioned, the fracture surface also exhibited third characteristic besides dimples and knobbly structure. The third characteristic of the fracture surface observed in this experiment was flat, smeared surface. This is presented in figure 4.7 for sample B tested at 852 s^{-1}. This smeared surface is characteristic of specimens tested in torsion using a torsional split Hopkinson bar. It appears as a result of rubbing between two fractured surfaces of the specimen. The smeared surface is not actually the characteristic of the material or strain rate, but is purely a mechanical consequence of the test conditions.

To summarise, there are three distinct regions on the fracture surface in the specimens tested in this study. These are dimples, knobbly structure and smeared surface.

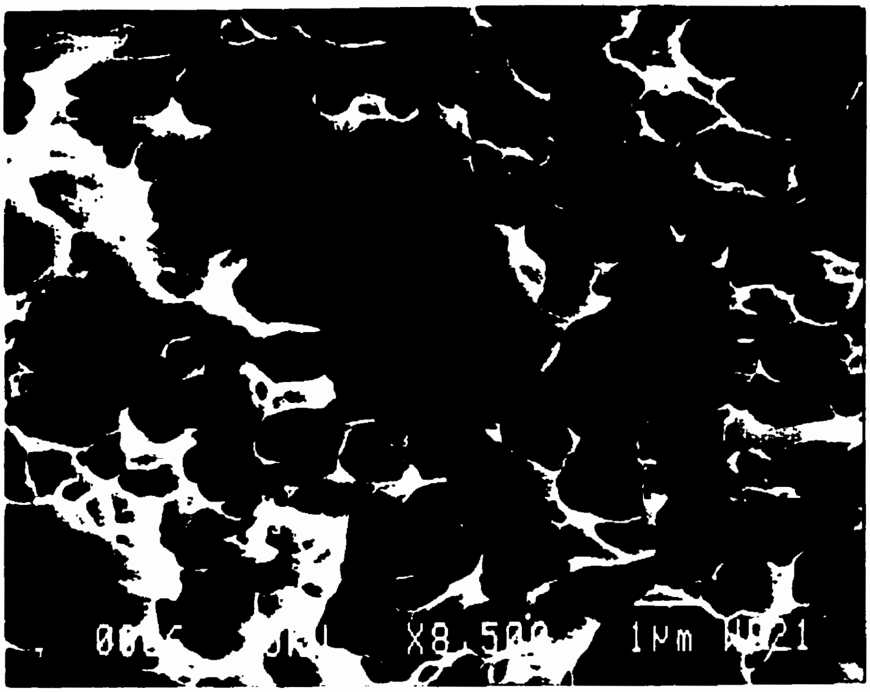

Figure 4.5: Dimples on the Fracture Surface

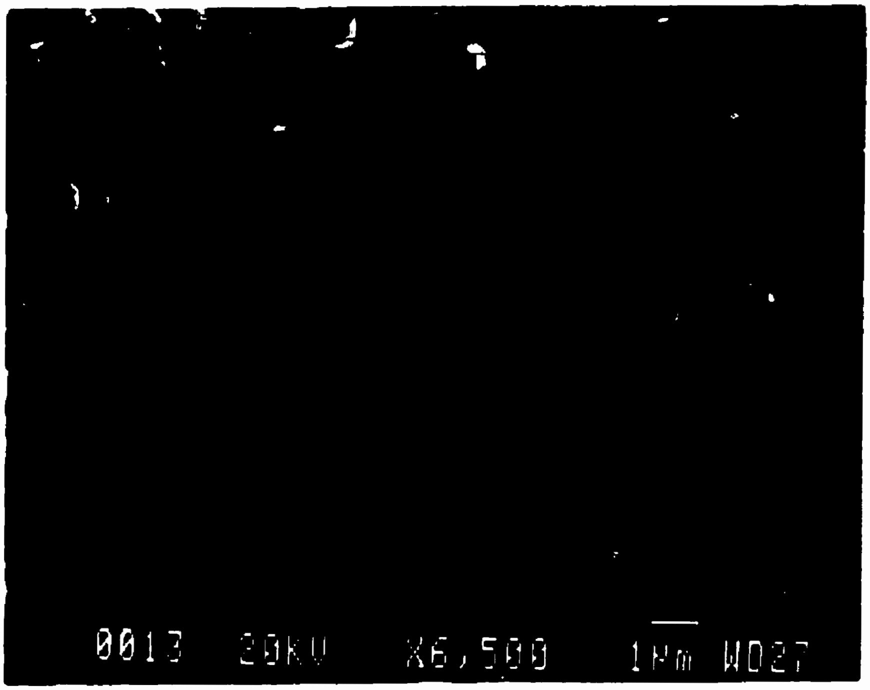

Figure 4.6: Knobbly Structure on Fracture Surface

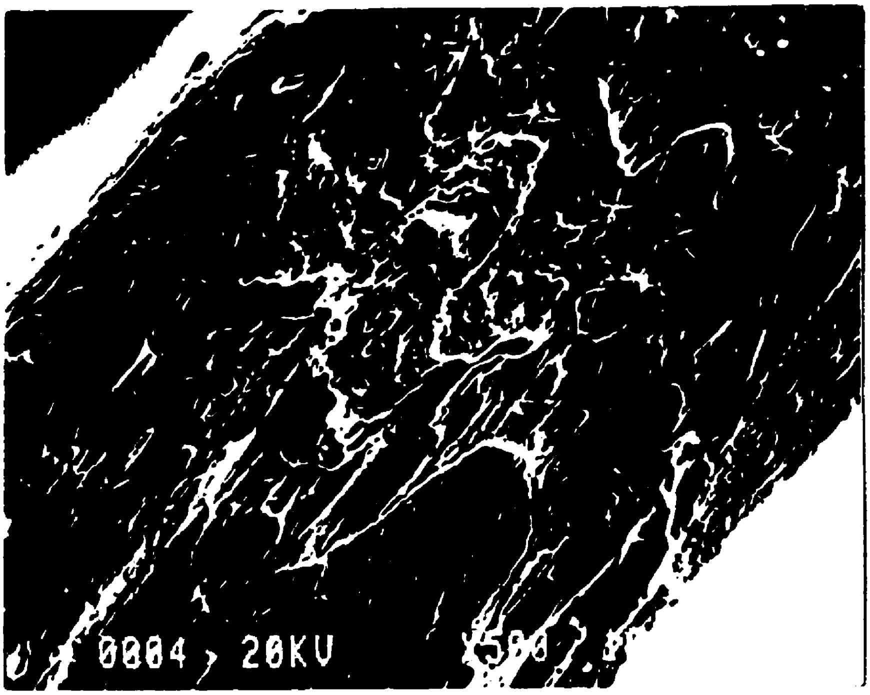

Figure 4.7: Smeared Surface

The most probable mechanism of fracture initiation is the microcrack initiation and void nucleation and coalescence. The nucleation sites for samples tested in this experiment include the interface between ferrite and pearlite grains in samples A and B. It is also possible that voids nucleate at the interface between ferrite and cementite lamellae in the single pearlite grain. The reason for void nucleation at these sites comes from the difference in strength of two phases. The grain boundaries have high strength compared to ferrite, and by plastic deformation of ferrite, the dislocations accumulate at these boundaries raising the stress and strain fields at the boundary. Because of the high stresses at the boundary, there will be decohesion between ferrite grains and pearlite (or other ferrite) grains. The decohesion between ferrite and cementite lamellae in the single pearlite grain forms in a similar fashion to one just described for ferrite/pearlite interface.

The microcrack initiation and void nucleation in samples C and D occurs at hard carbide particles dispersed in the matrix (tempered martensite). The mechanism of cracking in sample D is analogous to crack initiation in samples A and B described above, with the difference in phases. Here, the stronger phase is carbide, and softer phase is ferrite matrix. Sample C follows the same mechanism of crack initiation and void nucleation, but it has another possible site for microcrack and void initiation. Since this material also has the prior austenite grain boundaries, these boundaries are yet another site for void nucleation and microcrack initiation. The mechanism is similar to one described for samples A and B where the crack initiates at the boundary between the ferrite/pearlite interface.

Figure 4.8 presents the voids in sample B tested at 852 s^{-1}. It is seen that voids nucleated in line, grew and joined together forming a crack. It is also seen that there are other parallel cracks in this photo. By joining of these independent cracks, the final fracture occurred in the sample.

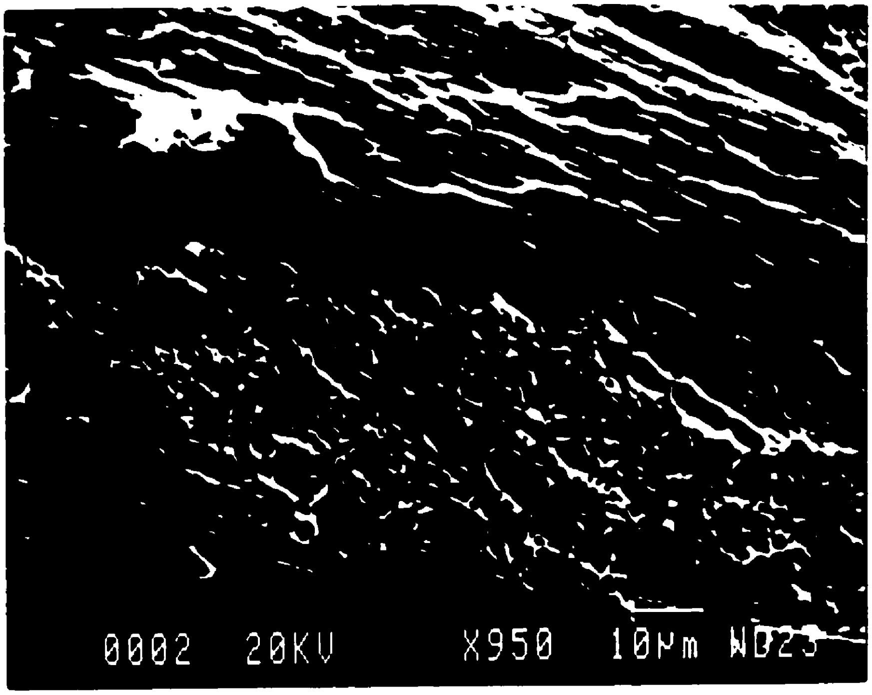

Figure 4.8: Void Nucleation and Coalescence

4.5 INFLUENCE OF MICROSTRUCTURE AND HARDNESS ON SHEAR BANDS

Before commenting on the influence of hardness on adiabatic shear band formation and morphology, the microstructure effect is examined. It is seen from chapter 3 that all samples tested at strain rate of 852 s^{-1} exhibited transformed type of the band. Also, all the specimens tested at strain rate of 255 s^{-1} exhibited the deformed type of the band. In these two groups of strain rates, the influence of microstructure on ASB is not evident. However, in the intermediate strain rate of 680 s^{-1}, some specimens showed the deformed band, and some showed the transformed band.

Specimens A and B tested at 680 s^{-1} were characterised by the deformed type of the shear band, while specimens C and D exhibited the transformed type of the shear band. It is at this strain rate that the influence of microstructure can be examined. Samples that showed deformed shear band are softer specimens A (VHN 250) and B (VHN 207) with hypoeutectoid microstructure consisting of ferrite and pearlite. Ferrite is the softest phase present in this steel, and since it is abundant in heat treatment belonging to samples A and B, it takes most of the deformation. The stress required to plastically deform ferritic-pearlitic structure is much less than the stress required to deform tempered martensitic structure. Thus, the energy supplied from the torsional loading pulse was spent in great portion on plastic deformation of the ferrite. The rest of the work was converted into heat that softened the material in the band. By simultaneous action of the plastic work and heat, the material within the band deformed both under influence of heat (softening effect) and applied stress. As a result of the elevated temperature in the band, some recrystallisation took place and the material in the band was characterised by the same but finer original microstructure, elongated in the direction of shearing.

The situation for samples C and D was somewhat different due to their high hardness. The microstructure of these steels is tempered martensite consisting of martensite and finely dispersed carbide particles in ferrite matrix. Martensite is very hard and brittle, and ferrite reinforced by fine carbides can be as hard as martensite. The difference in the shear band formation and type between softer samples A and B and harder samples C and D, lies in their microstructure and corresponding hardness. The mechanism of the shear band formation in samples A and B with softer ferrite-pearlite microstructure is explained above. Martensitic structure undergoes deformation in a different manner under high strain rates. Since the material is very hard (VHN 292 for C and VHN 352 for D), at high strain rates the flow stress becomes too large and the available plastic work due to the loading pulse is converted almost totally into heat. The heat is then generated and the material in the band experiences thermal softening due to high elevated temperature.. While soft, the material deforms leaving the shear band. Immediately after deformation takes place, the deformed material within the band is quenched by the surrounding matrix, thus undergoing the phase transformation, and the transformed shear band is formed.

The influence of hardness on the width of shear band is presented in figure 4.9. Data are presented for all samples tested and it is observed that the width of the shear band decreases as the hardness of the sample increases. This is true for all three strain rates produced in this experiment. The reason for this decrease in the band width with hardness is that harder materials cannot deform plastically at high strain rates if enough heat is not available. Since there is enough heat to soften the material, it will deform only in the region that was under very high temperature rise, and that is very narrow region. The rest of the material surrounding this narrow localised heated region will not undergo any plastic deformation. This comes form the fact that the flow stress decreases with the increase in temperature. Softer material will deform within and around the centre of the locally heated band, because its flow stress is lower than that of the harder material under the same strain rate and other conditions. All of this leads to wider shear bands in softer materials due to the larger portion of the material around the centreline of the band being deformed.

SPECIMEN	HARDNESS (VHN)	ASB WIDTH (microns)		
		Strain Rate 255 1/s	Strain Rate 680 1/s	Strain Rate 852 1/s
A	250	300	220	120
B	207	340	280	157
C	292	200	180	100
D	352	130	108	58

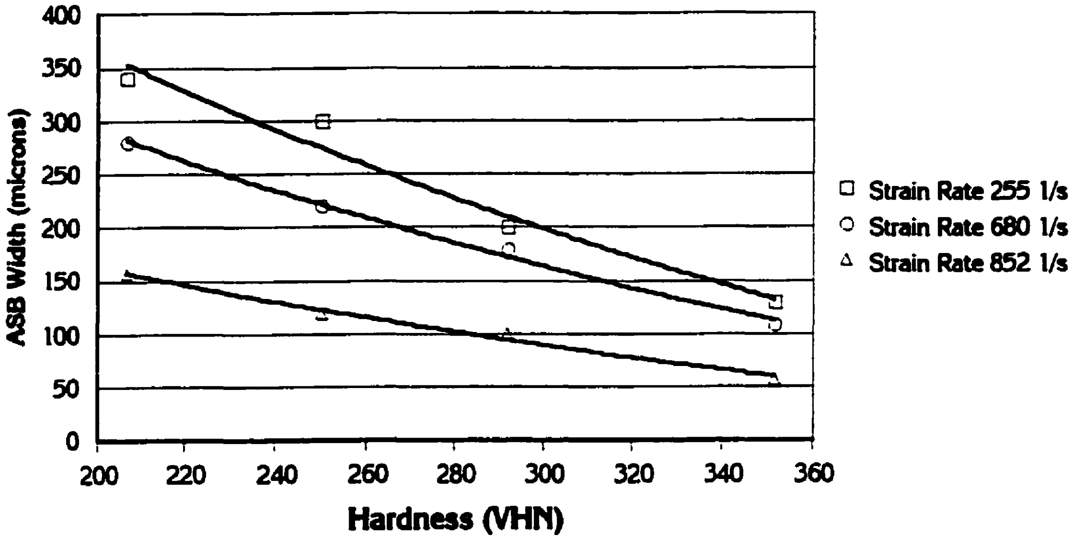

Figure 4.9: Influence of Hardness on ASB Width

Hardness of the sample also influences the fracture. It was mentioned earlier that the fracture type is the same for all tested samples, but the size of the produced dimples on the fracture surface is different. The size of the dimples decreases with the increased hardness and this is presented in figure 4.10 for strain rate of 255 s^{-1}. The relation between the dimple size and the adiabatic shear band width is presented in figure 4.11. It is seen that dimple size and the band width are proportional, i.e., for the wider band, there are larger dimples. This is consistent with the fact that the band is wider and that dimples are larger for the softer material.

4.6 INFLUENCE OF STRAIN RATE ON SHEAR BANDS

Strain rate has an influence on the formation of shear bands. As the strain rate increases, the width of the shear band decreases. This is shown in figure 4.12 for all four groups of samples tested at three different strain rates. The strain rate has similar influence on shear band width as the hardness.

SAMPLE	HARDNESS (VHN)	DIMPLE SIZE (μm)	NUMBER OF DIMPLES per 1 mm^2
A	250	0.71	1,986,551
B	207	0.87	1,323,420
C	292	0.51	3,848,597
D	352	0.25	16,008,001

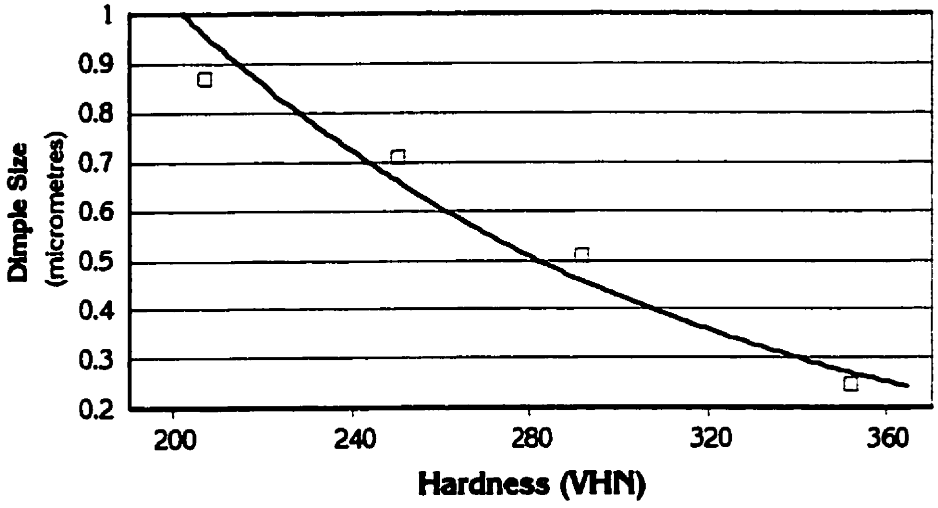

Figure 4.10: Influence of Hardness on Dimple Size

SAMPLE	ASB Width (μm)	DIMPLE SIZE (microns)	NUMBER OF DIMPLES per 1 mm^2
A	300	0.71	1,986,551
B	340	0.87	1,323,420
C	200	0.51	3,848,597
D	130	0.25	16,008,001

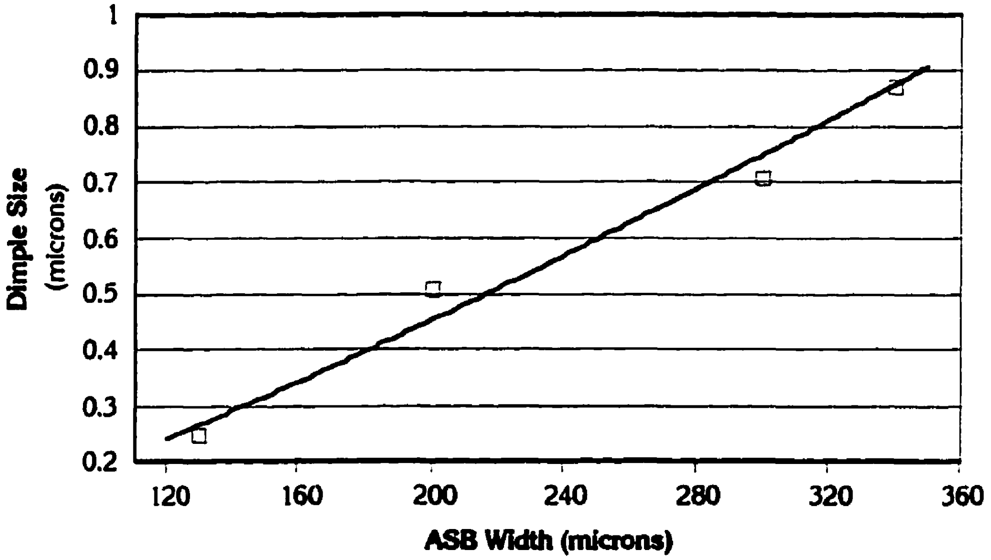

Figure 4.11: Relation Between Dimple Size and ASB Width

	SAMPLE			
	A	B	C	D
STRAIN RATE (1/s)	ASB Width (μm)			
255	300	340	200	130
680	220	280	180	108
852	120	157	100	58

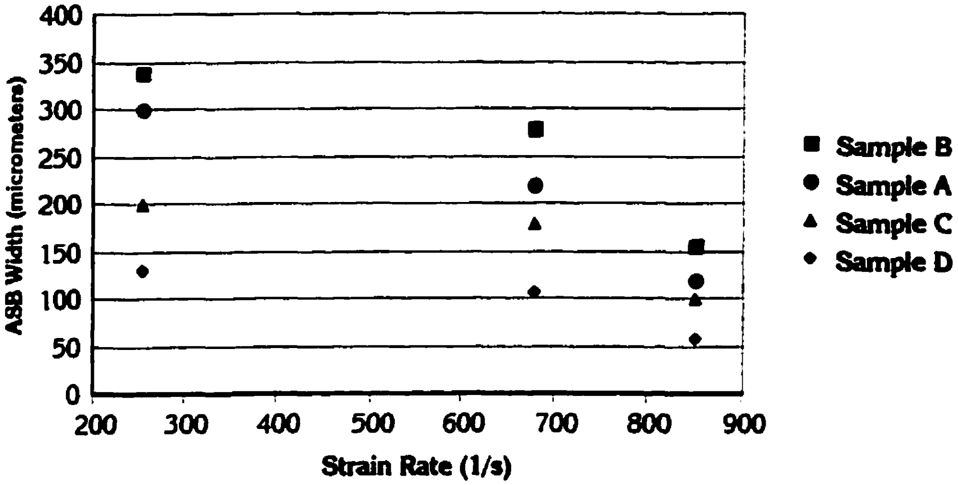

Figure 4.12: Influence of Strain Rate on ASB Width

CHAPTER 5 CONCLUSIONS

Different microstructures of AISI 4140 steel were tested at strain rates of 255 s^{-1}, 680 s^{-1} and 852 s^{-1}. Samples were grouped according to their heat treatment and microstructure in groups A, B, C and D.

All samples tested exhibited the presence of adiabatic shear bands. However, the type of the shear band formed in the sample depended on the strain rate and microstructure of the sample material. At low strain rate of 255 s^{-1}, all specimens showed deformed type of shear band. Samples tested in the intermediate strain rate range of 680 s^{-1} showed mixed shear bands. Ferritic-pearlitic specimens A and B exhibited the deformed type of the band, while samples C and D with tempered martensite structure exhibited the transformed shear bands. All of the samples tested at high strain rate of 852 s^{-1} showed the transformed type of the shear band. It was concluded that the type of the shear band that forms depends on both the strain rate and microstructure.

The width of the shear band varies with hardness and the strain rate. Higher hardness produces narrower shear bands, as does the higher strain rate. As the hardness and strain rate are decreased, the width of the shear band increases.

The type of fracture exhibited by all samples tested in this study, independent on strain rate or the microstructure, was ductile and was characterised by the occurrence of dimples. While the primary mode of fracture does not depend on strain rate and hardness, it was concluded that the size of dimples depends on the hardness. The higher the hardness, the smaller the dimple size.

REFERENCES

[1] Zukas, J. A., *et al.*, *Impact Dynamics*, John Wiley & Sons Inc., 1982

[2] Tresca, H., *Proc. Inst. Mech. Engrs.*, **30**, (1878) 301

[3] Zener, C. and Hollomon, J. H., *J. Appl. Phys.*, **14**, (1944) 22-32

[4] Costin, L. S., Crisman, E. E., Hawley, R. H. and Duffy, J., *Int. Phys. Conf. Ser.*, **47**, (1979) 90-100

[5] Hartley, K. A., Duffy, J. and Hawley, R. H., *J. Mech. Phys. Solids*, **35**, (1987) 283-387

[6] Giovanola, J. H., *Mechanics of Materials*, **7**, (1988) 59-71

[7] Marchand, A. and Duffy, J., *J. Mech. Phys. Solids*, **36**, (1988) 251-83

[8] Bai, Y., in *Shock Waves and High-Strain-Rate Phenomena in Metals*, M. A. Meyers and L. E. Murr (eds.), Plenum Press, New York, 1981, 277-84

[9] Moss, G. L., in *Shock Waves and High-Strain-Rate Phenomena in Metals*, M. A. Meyers and L. E. Murr (eds.), Plenum Press, New York, 1981, 299-312

[10] Lindholm, U. S. and Johnson, G. R., in *Material Behaviour Under High Stress and Ultra-High Loading Rates*, J. Mescall and V. Weiss (eds.), Plenum Press, New York, 1983, 61-79

[11] Cottrell, A. H., in *The Properties of Materials at High Rates of Strain*, Instn. Mech. Eng. London, 1957

[12] Duffy, J., in *Proc. Conf. on Mechanical Properties at High Rates of Strain*, J. Harding (ed.), The Instutute of Physics London, 1979, 1

[13] Klepaczko, J. and Duffy, J., ASTM STP 765, R. W. Rohde and J. C. Swearengen (eds.), 1982, 251

[14] Nicholas, T., *Impact Dynamics*, J. A. Zukas *et al.* (ed.), New York: Wiley, 1981, 227

[15] Lindholm, U. S., *J. Mech. Phys. Solids*, **12**, (1964) 317

[16] Hartley, K. A. and Duffy, J., in *Mechanical Properties at High Rates of Strain*, J. Harding (ed.), The Institute of Physics Bristol and London, 1984, 21-30

[17] Campbell, J. D. and Dowling, A. R., *J. Mech. Phys. Solids*, **18**, (1970) 43

[18] Frantz, R. A. and Duffy, J., *J. Appl. Mech.*, **39**, (1972) 939

[19] Gilman, J. J., *Micromechanics of Flow in Solids*, McGraw-Hill, New York, 1969

[20] Johnston, W. G. and Gilman J. J., *J. Appl. Phys.*, **30**, (1959) 129

[21] Hull, D. and Bacon, D. J., *Introduction to Dislocations*, Pergamon Press, 1984

[22] Malvern, L. E., in *Mechanical Properties at High Rates of Strain*, J. Harding (ed.), The Institute of Physics Bristol and London, 1984, 1-20

[23] Kassner, M. E. and Breithaupt, R. D., in *Mechanical Properties at High Rates of Strain*, J. Harding (ed.), The Institute of Physics Bristol and London, 1984, 47-54

[24] Ellwood, S., Griffits, L. J., Parry, D. J., in *Mechanical Properties at High Rates of Strain*, J. Harding (ed.), The Institute of Physics Bristol and London, 1984, 55-62

[25] Regazzoni, G. and Montheillet, F., in *Mechanical Properties at High Rates of Strain*, J. Harding (ed.), The Institute of Physics Bristol and London, 1984, 63-70

[26] Clifton, R. J., Gilat, A. and Li, C. H., in *Material Behaviour Under High Stress and Ultra-High Loading Rates*, J.Mescall and V. Weiss (eds.), Plenum Press, New York, 1983, 1-19

[27] *http://www.ncemt.ctc.com/em-a/log-strs.html*, Concurrent Technologies Corporation, 1998

[28] Bai, Y., *Res. Mechanica*, **31**, (1990) 133-203

[29] Considere, A., *Ann. des Ponts et Chausséés*, **9**, (1885) 574

[30] Culver, R. S., in *Proc. 3rd Int. Conf. of the Centre for High Energy Forming*, 1971

[31] Culver, R. S., in *Metallurgical Effects at High Strain Rates*, R. W. Rohde, B. M. Butcher, J. R. Holland and C. H. Karnes (eds.), Plenum Press, New York, 1973, 519-30

[32] Taylor, G. I. and Quinney, H., *Proc. Roy. Soc., Ser. A.*, **143**, (1934) 307-26

[33] Staker, M. R., *Acta Metall.*, **29**, (1981) 683-9

[34] Olson, G. B., Mescal, J. F. and Azrin, M., in *Shock Waves and High Strain Rate Phenomena in Metals*, M. A. Meyers and L. E. Murr (eds.), Plenum Press, New York, 1981, 221-47

[35] Vinh, T., Afzali, M. and Roche, A., in *3rd Int. Conf. Mech. Behav. Mat. (ICM3)*, K. J. Miller and R. F. Smith (eds.), Cambridge, UK, **2**, (1979) 633-42

[36] Burns, T. J., Grady, D. E. and Costin, L. S., *Shock Waves in Condensed Matter*, Amer. Phys. Soc., Menlo Park, CA, 1982, 372-5

[37] Dodd, B. and Atkins, A. G., *Acta Metall.*, **31**, (1983) 9-15

[38] Bai, Y., Cheng, C. and Shanbing, Y., *Acta Mechanica Sinica*, **2**, (1986) 1-7

[39] Grady, D. E. and Kipp, M. E., *J. Mech. Phys. Solids*, **35**, (1987) 95-118

[40] Dodd, B. and Bai, Y., *Mat. Sci. Tech.*, **1**, (1985) 38-40

[41] Campbell, J. D., *Mat. Sci and Eng.*, **12**, (1973) 3

[42] Rogers, H. C., in *Deformation Processing and Structure*, G. Krauss (ed.), ASM, Metals Park, OH, 1984, 425-44

[43] Shockey, D. A., in *Metallurgical Applications of Shock-Wave and High-Strain-Rate Phenomena*, L. E. Murr, K. P. Staudhammer and M. A. Meyers (eds.), Marcel Dekker, New York and Basle, 1986, 633-56

[44] Rosenfield, A. R. and Hahn, G. T., *Trans. ASM*, **59**, (1966), 962

[45] Batra, R. C. and Kim, C. H., *Int. J. Engng. Sci*, **29**, (1991) 949-60

[46] Nakkalil, R., Hornaday Jr., J. R., Bassim, M. N., *Mat. Sci. and Eng.*, **A141**, (1991) 247-60

[47] Zhu, Z. G. and Batra, R. C., *Computers & Structures*, **39**, (1991) 459-72

[48] Bacmann, M. E. and Finnegan, S. A., in *Metallurgical Effects at High Strain Rates*, R. W. Rohde, B. M. Butcher, J. R. Holland and C. H. Karnes (eds.), Plenum Press, New York, 1973, 531-43

[49] Rogers, H. C., *Annu. Rev. Mater. Sci.*, **9**, (1979) 283-311

[50] Bedford, A. J., Wingrove, A. L. and Thompson, K. R. L., *J. Aust. Inst. Met.*, **19**, (1974) 61-73

[51] Timothy, S. P., *Acta. Metall.*, **35** (2), (1987) 301-6

[52] Stelly, M. and Dormeval, R., in *Metallurgical Applications of Shock-Wave and High-Strain-Rate Phenomena*, L. E. Murr, K. P. Staudhammer and M. A. Meyers (eds.), Marcel Dekker, New York and Basle, 1986, 607-32

[53] Cepus, E., *Evolution of Adiabatic Shear Bands in High Strength Steels at High Shear-Strain Rates*, University of Manitoba, Canada, M. Sc. Thesis, 1995

[54] Wang, L. L., Lu, W. X., Hu, S. S. and Tang, Z. P., *IUTAM Symposium*, Tokyo, Japan, 1985, 395-406

[55] Dao, K. C. and Shockey, D. A., *Metall. Trans.*, **50**, (1979) 8244-46

[56] Samuels, L. E. and Lamborn, I. R., *Metallography of Failure Analysis*, L. J. McCall and P. M. French (eds.), Plenum Press, New York, 1978, 167

[57] Bhambri, A. K., *Microstr. Sci.*, **7**, (1979) 255

[58] Timothy, S. P. and Hutchings, I. M., *Acta Metall.*, **33**, (1985) 667-76

[59] Bassim, M. N. and Panic, N., in *Advances in Materials and Processing Technologies '97*, 1997, 913-18

[60] Rogers, H. C., *Adiabatic Shearing -a Review*, Drexel Univ. Report, 1974

[61] Rogers, H. C., in *Material Behaviour Under High Stress and Ultra-High Loading Rates*, J. Mescall and V. Weiss (eds.), Plenum Press, New York, 1983, 101-18

[62] Craig, S. J., *Journal de Physique - Int. Conf. on Mech. and Phys. Behaviour of Materials Under Dynamic Loading*, **4** (C8), (1994) 41-6

[63] Wittman, C. L, Meyers, M. A. and Pak, H. R., *Metall. Trans.*, **21A**, (1990) 707-16

[64] Speich, G. R. and Szirmae, A., *Trans. AIME*, **245**, (1968) 1063-74

[65] Mgbokwere, C. O., Nutt, S. R and Duffy, J., *Mechanics of Materials*, **17**, (1994) 97-110

[66] Hines, J. A., Vecchio, K. S. and Ahzi, S., *Metall. and Mat. Trans. A*, **29A**, (1998) 191-203

[67] Zhang, B., Shen, W., Liu, Y., Tang, X. and Wang, Y., *Wear*, **211**, (1997) 164-8

[68] Talunts, G. G., Eshchenko, R. N., Borychev, A. N., Muryshev, E. Y. and Sinitsyn, A. V., *Fizika Metalov i Metallovedenie*, **n4**, (1992) 45-52

[69] Giovanola, J. H., *Impact Loading and Dynamic Behaviour of Materials*, C. Y. Chiem, H. D. Kunze and L. W. Meyer (eds.), DGM Informationgessellshaft - Verlag, Oberursel, 1987

[70] Cho, K., Chi, Y. C. and Duffy, J., *Metall. Trans.*, **21A**, (1990) 1161-75

[71] Chung, D. T., Moon, S. K. and Yoo, Y. H., *Journal de Physique*, **4**, (1994) 547-52

[72] Panic, N., *Study of the High Strain rate Behaviour of Steels*, University of Manitoba, Canada, B. Sc. Thesis, 1997

[73] Irwin, G. J., DREV-R-652/72, Canada, 1972

[74] Zurek, A. K., Follansbee, P. S. and Hack, J., *Metall. Trans.*, **21A**, (1990) 431-9

[75] Mengmei, X., *Acta Armamentarii*, **n3**, (1983) 34-44

[76] Bassim, M. N. and Mucz, R. J., *Review of the State-of-the-Art Technology and of the Canadian Capabilities in the Filed of High Strain Rate Material Properties*, MONAC International Corporation, 1990

[77] Yokoyama, T. and Kishida, K., *Journal of Testing and Evaluation*, **14 n5**, (1986) 236-42

[78] Kolsky, H., *Proc.Phys. Soc.*, **62B**, (1949) 676

[79] Baker, W. E. and Yew, C. H., *J. Appl. Mech. Trans. ASME (E)*, **38**, (1966) 917-23

[80] Hartley, K. A., Duffy, J. and Hawley, R. H., in *Metals Handbook: Mechanical Testing, Volume 8*, ASM Metals Park, OH, 1985, 218-39

[81] Mehl, R. F., in *Metals Handbook: Atlas of Microstructures of Industrial Alloys, Volume 7*, ASM Metals Park, OH, 1972

[82] *Metals Handbook: Properties and Selection of Metals, Volume 1*, 8th ed., ASM Metals Park, OH, 1961

[83] Molinari, A. and Clifton, R. J., *J. Appl. Mech.*, **5**, (1987) 806-12